IDAHO TRANSPORTATION DEPARTMENT

RESEARCH REPORT

Your Safety • Your Mobility
Your Economic Opportunity

RP 265

Effectiveness of High-Early Strength Concrete Class 50AF with Polypropylene Fibers as a Cost-Effective Alternative for Field-Cast Connections of Precast Elements in Accelerated Bridge Construction

By

PIs: Arya Ebrahimpour and Mustafa Mashal

Students: Maximilian Casanova, Utsa Rashique, Christopher Clauson, and Ali Shokrgozar

Prepared for

Idaho Transportation Department

Research Program, Contracting Services

Division of Engineering Services

https://itd.idaho.gov/alt-programs/?target=research-program

October 2018

Standard Disclaimer

This document is disseminated under the sponsorship of the Idaho Transportation Department and the United States Department of Transportation in the interest of information exchange. The State of Idaho and the United States Government assume no liability of its contents or use thereof.

The contents of this report reflect the view of the authors, who are responsible for the facts and accuracy of the data presented herein. The contents do not necessarily reflect the official policies of the Idaho Transportation Department or the United States Department of Transportation.

The State of Idaho and the United States Government do not endorse products or manufacturers. Trademarks or manufacturers' names appear herein only because they are considered essential to the object of this document.

This report does not constitute a standard, specification or regulation.

1. Report No. FHWA-ID-16-246	2. Government Accession No.	3. Recipient's Catalog No.
4. Title and Subtitle Effectiveness of High-Early Strength Concrete Class 50AF with Polypropylene Fibers as a Cost-Effective Alternative for Field-Cast Connections of Precast Elements in Accelerated Bridge Construction		5. Report Date July 2018 6. Performing Organization Code
7. Author(s) Arya Ebrahimpour, Mustafa Mashal, Maximilian Casanova, Utsa Rashique, Christopher Clauson, and Ali Shokrgozar		8. Performing Organization Report No.
9. Performing Organization Name and Address Department of Civil and Environmental Engineering Idaho State University Pocatello, Idaho 83209		10. Work Unit No. (TRAIS) 11. Contract or Grant No. ISU-17-01
12. Sponsoring Agency Name and Address Idaho Transportation Department (SPR) Division of Engineering Services, Contracting Services, Research Program PO Box 7129 Boise, ID 83707-7129		13. Type of Report and Period Covered Final Report 12/16/2016 -- 7/31/2018 14. Sponsoring Agency Code RP 265
15. Supplementary Notes Project performed in cooperation with the Idaho Transportation Department and the Federal Highway Administration.		

16. Abstract

Accelerated Bridge Construction (ABC) methods are relatively new in the U.S. and Idaho. ABC requires that bridge precast concrete components be effectively connected to one another in the field. Currently Ultra-High Performance Concrete (UHPC) is used to connect precast bridge deck panels or girders in 6-in. wide closure pours between the precast elements. As an alternative, Idaho Transportation Department (ITD) is proposing to place High-Early Strength (HES) concrete with polypropylene fibers (compressive strength of minimum 5 ksi in 28 days) in 10-in. closure pours between girders. There are several advantages to this alternate material. An experimental and numerical research project was carried out at Idaho State University to determine the effectiveness of the alternate material and the connection detail. The experimental work consisted of small specimen testing and larger specimens with headed bars. Among the six closure pour concrete mixes considered, one was selected that had the largest compressive and tensile strength values and the lowest shrinkage value. Using the results of the larger specimens, a finite element model of the new connection was developed. The behavior of the ITD's 10-in. closure pour connection with the optimum mix longitudinally placed between precast girders of a bridge was studied. For this analysis, the AASHTO's requirements for Strength I, Service I, and Fatigue I Limit States were considered.

17. Key Words Bridge, deck, high-early strength concrete, connection, precast elements, accelerated bridge construction	18. Distribution Statement Copies available online at: https://itd.idaho.gov/alt-programs/?target=research-program

19. Security Classification (of this report) Unclassified	20. Security Classification (of this page) Unclassified	21. No. of Pages 130	22. Price None

FHWA Form F 1700.7

METRIC (SI*) CONVERSION FACTORS

APPROXIMATE CONVERSIONS TO SI UNITS

Symbol	When You Know	Multiply By	To Find	Symbol
		LENGTH		
in	inches	25.4	millimeters	mm
ft	feet	0.3048	meters	m
yd	yards	0.914	meters	m
mi	Miles (statute)	1.61	kilometers	km
		AREA		
in^2	square inches	645.2	millimeters squared	cm^2
ft^2	square feet	0.0929	meters squared	m^2
yd^2	square yards	0.836	meters squared	m^2
mi^2	square miles	2.59	kilometers squared	km^2
ac	acres	0.4046	hectares	ha
		MASS (weight)		
oz	Ounces (avdp)	28.35	grams	g
lb	Pounds (avdp)	0.454	kilograms	kg
T	Short tons (2000 lb)	0.907	megagrams	mg
		VOLUME		
fl oz	fluid ounces (US)	29.57	milliliters	mL
gal	Gallons (liq)	3.785	liters	liters
ft^3	cubic feet	0.0283	meters cubed	m^3
yd^3	cubic yards	0.765	meters cubed	m^3

Note: Volumes greater than 1000 L shall be shown in m^3

		TEMPERATURE (exact)		
°F	Fahrenheit temperature	5/9 (°F-32)	Celsius temperature	°C
		ILLUMINATION		
fc	Foot-candles	10.76	lux	lx
fl	foot-lamberts	3.426	candela/m^2	cd/cm^2
		FORCE and PRESSURE or STRESS		
lbf	pound-force	4.45	newtons	N
psi	pound-force per square inch	6.89	kilopascals	kPa

APPROXIMATE CONVERSIONS FROM SI UNITS

Symbol	When You Know	Multiply By	To Find	Symbol
		LENGTH		
mm	millimeters	0.039	inches	in
m	meters	3.28	feet	ft
m	meters	1.09	yards	yd
km	kilometers	0.621	Miles (statute)	mi
		AREA		
mm^2	millimeters squared	0.0016	square inches	in^2
m^2	meters squared	10.764	square feet	ft^2
km^2	kilometers squared	0.39	square miles	mi^2
ha	hectares (10,000 m^2)	2.471	acres	ac
		MASS (weight)		
g	grams	0.0353	Ounces (avdp)	oz
kg	kilograms	2.205	Pounds (avdp)	lb
mg	megagrams (1000 kg)	1.103	short tons	T
		VOLUME		
mL	milliliters	0.034	fluid ounces (US)	fl oz
liters	0.264	Gallons (liq)	gal	m^3
	meters cubed	35.315	cubic feet	ft^3
m^3	meters cubed	1.308	cubic yards	yd^3

		TEMPERATURE (exact)		
°C	Celsius temperature	9/5 °C+32	Fahrenheit temperature	°F
		ILLUMINATION		
lx	lux	0.0929	foot-candles	fc
cd/cm	candela/m^2	0.2919	foot-lamberts	fl
		FORCE and PRESSURE or STRESS		
N	newtons	0.225	pound-force	lbf
kPa	kilopascals	0.145	pound-force per square inch	psi

Acknowledgements

The authors would like to thank the Idaho Transportation Department for supporting this research project. We would like to thank the members of the Technical Advisory Committee, Matt Farrar, Dan Gorley, Leonard Ruminski and Ned Parish for their support and valuable input. Leonard Ruminski provided extensive input in several key parts of this project. Dr. Saiidi of the University of Nevada, Reno, served as the peer reviewer for this project. We appreciate his input. Mike Horrocks of Pocatello Ready Mix is acknowledged for donating materials for the project and providing technical support. This project provided experience in laboratory experimental research, structural computer modeling, and data analysis for two graduate students (Maximilian Casanova and Utsa Rashique) and one undergraduate student (Christopher Clauson) at the Idaho State University. Ali Shokrgozar, a Ph.D. student at ISU, provided assistance in bridge computer modeling.

Technical Advisory Committee

Each research project is overseen by a technical advisory committee (TAC), which is led by an ITD project sponsor and project manager. The Technical Advisory Committee (TAC) is responsible for monitoring project progress, reviewing deliverables, ensuring that study objectives are met, and facilitating implementation of research recommendations, as appropriate. ITD's Research Program Manager appreciates the work of the following TAC members in guiding this research study.

Project Sponsor – Matt Farrar, P.E.

Project Manager – Dan Gorley, P.E.

TAC Members
Leonard Ruminski, P.E.
Ned Parrish

FHWA-Idaho Advisor – Ed Miltner

Table of Contents

List of Tables

List of Figures

List of Acronyms

ABC	Accelerated Bridge Construction
ACI	American Concrete Institute
AASHTO	American Association of State Highway and Transportation Officials
ASTM	American Society for Testing and Materials
BA	Bonding Admixture
BG	Bonding Agent (an abbreviation used in this report)
CZM	Cohesive Zone Model
DAQ	Data Acquisition System
DOF	Degrees of Freedom
FE	Finite Element
FHWA	Federal Highway Administration
HES	High-Early Strength
HRWR	High Range Water reducer
HyFRC	Hybrid Fiber Reinforced Concrete
ISU	Idaho State University
ITD	Idaho Transportation Department
LEFM	Linear Elastic Fracture Mechanics
LRFD	Load and Resistance Factor Design
LVDT	Linear Variable Differential Transformer
NSCG	Non-shrink Cementitious Grout
NTS	Not to Scale
PBE	Precast Bridge Element
SRA	Shrinkage Reducing Admixture
SSD	Saturated Surface Dry
TAC	Technical Advisory Committee for the project
UHPC	Ultra-High Performance Concrete
VCCT	Virtual Crack Closure Technique

Executive Summary

Introduction

Accelerated Bridge Construction (ABC) methods are relatively new in the U.S. and Idaho. ABC requires that bridge precast concrete components be effectively connected to one another in the field. Currently there is a trend of using Ultra-High Performance Concrete (UHPC) for field connections. There have been several experimental tests showing that precast bridge deck panels or girders may be effectively connected by placing UHPC in 6-in. wide closure pours between the precast elements. As an alternative, Idaho Transportation Department (ITD) is proposing to place High-Early Strength (HES) concrete with fibers with a minimum compressive strength of 5 ksi in 28 days in 10-in. closure pours between girders.

The advantages of the alternative material and connection detail include: (1) HES concrete with fibers can be batched in the ready mix plant, brought to the field in the mixing truck, and placed similar to conventional concrete; (2) ITD allows removal of forms for HES concrete after one day, while for UHPC a minimum curing time of four days and a compressive strength of 14 ksi is required before removal of the forms; and (3) the estimated cost saving for one project alone is approximately $100,000. Note that UHPC is a proprietary material with an installed cost of $10,000-$15,000 per cubic yard based on actual bid prices for UHPC in Idaho Transportation Department bridge projects between 2016 and 2018.

Project Objectives and Tasks

The project objectives are: (1) obtain experimental data on the behavior of six mixes containing HES concrete Class 50AF with and without polypropylene fibers, select the optimum mix, and perform laboratory tests on larger specimens; and (2) use the experimental results to create a computer model of the proposed closure pour detail that is capable of assessing the connection strength and provide an indication of fatigue performance. To carry out the above objectives, the following tasks were assigned. This report focuses on Tasks 1-5.

- Task 1: Perform a literature review.
- Task 2: Select HES concrete mixes with and without polypropylene fibers. Determine material properties and choose the optimum mix.
- Task 3: Obtain bond strength between the optimum mix and the precast concrete. In addition, perform headed bar tensile strength tests in a closure pour connection. The specimen is to represent the lower half portion of a closure pour section.
- Task 4: Perform three-point and four-point flexural tests of beams composed of two precast segments with the optimum mix in ITD's 10-in. closure pour detail in the middle.
- Task 5: Develop finite element (FE) models for headed bar pull-out specimens as well as the beam specimens and compare results with the experimental results. In addition, investigate the adequacy of the connection with the optimum mix between Deck Bulb-T girders in a typical bridge. Using the AASHTO LRFD design requirements, check adequacy of connection for Strength I, Service I, and Fatigue I Limit States.

- Task 6: Make a presentation to the ITD Bridge Section staff describing the project and results.
- Task 7: Submit the final project report.

Task 1

In the literature review, five main sections were covered: (a) an overview of the field-cast connections of prefabricated bridge elements; (b) related testing methods; (c) preparation of laboratory concrete specimens; (d) materials needed for the closure pour, including bonding agent and polypropylene fibers; and (e) literature needed for computer modeling. Literature review revealed that high performance fiber-reinforced concrete has been used as an alternate material to UHPC in connecting certain bridge precast components. Work by others gave insight as to the appropriate ASTM testing methods and sample preparation techniques. It was also concluded that rebar bond-slip plays an important role in numerical modeling.

Task 2

Task 2 was to select HES concrete mixes with and without polypropylene fibers and other additives. This task was done with direct input from the TAC members. Six mixes were selected with different amounts of fiber with and without Shrinkage Reducing Admixture (SRA) and Bonding Admixture (BA). Compressive strength, tensile strength, and shrinkage behavior of each mix were determined. Table ES1 shows these mixes, and the corresponding material properties using ASTM standard tests methods.

Table ES1. HES mix variables and the measured average properties.

Mix	Variables			1-day compressive strength (psi)	28-day compressive strength (psi)	Split tensile strength (psi)	Shrinkage (microstrain)
	Fiber (lb/yd^3)	SRA	BA				
A (Control)	-	-	-	3,196	7,752	767	736
B	0.75	-	-	3,442	8,471	634	655
C	1.5	-	-	3,551	7,860	733	673
D	1.5	✓	-	3,074	8,864	837	522
E	0.75	✓	✓	2,550	7,710	749	555
F	-	✓	✓	2,723	8,161	765	528

Mix D, containing 1.5 lb/yd^3 of fiber and shrinkage reducing admixture, performed the best. It had the largest compressive and tensile strength values and the lowest shrinkage value. These values were 8,864 psi, 837 psi, and 522 microstrain, respectively. For computer modeling, modulus of elasticity and Poisson's ratio of the optimum mix were also obtained.

Task 3

Task 3 was to obtain the interface bond strength and perform headed bar pull-out tests. With input from TAC, Mixes D and E with and without bonding agent were selected for the ASTM C78 four-point bending tests. The interface surfaces of the precast segments were prepared to have exposed

aggregates. Mix D without the bonding agent performed the best with a bond strength (modulus of rupture) value of 612 psi. In contrast, De la Varga, Haber, and Graybeal (2016) obtained a value of 712 psi for the interface bond strength between UHPC and precast concrete with exposed aggregate surface.[1]

Next, headed bar tensile strength tests were performed in a closure pour connection with the optimum mix. The specimen represents the lower half portion of a closure pour section. Figure ES1 shows the headed bar pull-out specimen fabrication sequence. The specimens were 4 in. thick, 9 in. wide and 20 in. long. The length consisted of a 10-in. closure pour segment in the middle and two 5-in. long precast segments at the ends. No. 5 headed bars were installed at 3-in. spacing between opposing bars. Six specimens were tested. Table ES2 shows the pull-out test results. In all tests the initial crack occurred at the upper interface between closure pour and precast at the average force of 5,820 lb. The average ultimate pull-out force was 12,511 lb. Even after the cracking of the upper interface, the strut action between the opposing lapped bars was effective, resulting in upper bar stress of 40.4 ksi or 67% of the steel specified yield strength. The most useful data was the relationship between the total tensile force in the specimen and the force carried by the head of the upper bars. This relationship was used to calibrate the FE model of the pull-out specimen.

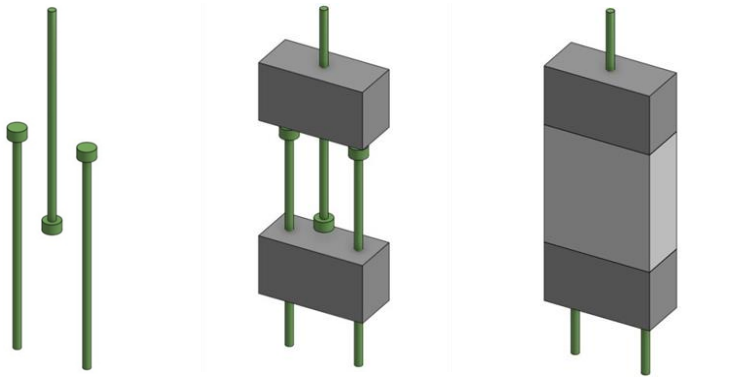

(a) Rebars **(b) Precast concrete segments** **(c) Specimen with closure pour segment**

Figure ES1. Headed bar pull-out specimen fabrication sequence.

Table ES2. Headed bar pull-out test average values.

Cracking force (lb)	Force carried by the head at cracking force (lb)	Ultimate force (lb)	Force carried by the head at ultimate load (lb)	Stress in the upper bar at ultimate force (ksi)
5,820	239	12,511	3,516	40.3

Task 4

Task 4 was to perform three-point and four-point flexural tests of beams composed of two precast segments with the optimum mix closure pour segment in the middle. The beams had a span of 72 inches between the supports and were 12 inches in width and 8 inches in height. A total of four No. 5 headed

bars, two from each side, created a lap splice inside the closure at the bottom. Regular No. 5 reinforcing bars were used in a similar fashion at the top. The ITD's 10-in. closure pour detail was used. Figure ES2 shows the components of the beam specimen. Three of each beam tests were performed. In the three-point testing, the load at the center was applied on a 10 in. x 20 in. steel plate in order to simulate an AASHTO truck wheel patch. Table ES3 shows the beam test results. In both cases of three-point bending and four-point bending, the initial crack always formed on the lower right of the interface between closure pour and precast. This was a limitation of the beam specimens; i.e., unsymmetrical placement of reinforcing and the small width of the beam. Both the three-point and four-point loading tests had almost the same ultimate moment capacity of about 147 kip-in. The mid-span moment versus the bar stress next to the head of the headed bars (where the strain gages were installed) provided the most useful information. This data was used for comparing results with the FE model results.

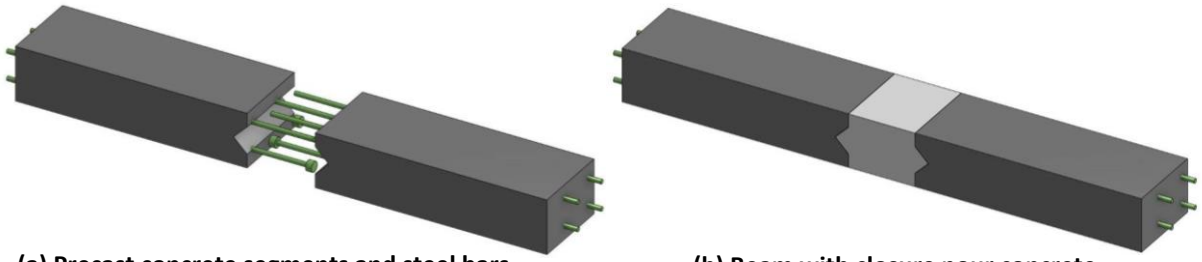

(a) Precast concrete segments and steel bars **(b) Beam with closure pour concrete**

Figure ES2. Components of the beam specimen.

Table ES3. Summary of average values of beam test results.

Test type	Cracking force (lb)	Cracking moment (kip-in.)*	Ultimate force (lb)	Ultimate moment (kip-in.)	Mid-span displacement at ultimate force (in.)
3-point	2,867	44.4	9,492	147.1	0.283
4-point	2,933	35.2	12,209	146.5	0.328

* For the three-point bending test, the moment is calculated at the center, although crack is at the interface.

Task 5

This task had two components. The first one was to develop the FE models for headed bar pull-out and the beam specimens and compare the results with the experimental test results. In addition, the task required investigation of the adequacy of the connection with the optimum mix between the Deck Bulb-T girders of a typical bridge. ANSYS software was used for FE modeling.

The FE models of the pull-out and beam specimens performed well in the linear region and resulted in very good agreements with the experimental results of moment versus stress in the bar next to the head. See Figure ES3 for the three-point bending test comparison. The agreement in the nonlinear region was not as good with the beam bending tests. Although not measured in the experiments, the FE model of the beam showed a larger bar stress at the interface compared to the bar stress next to the head. Rebar bond-slip had a big role in capturing the experimental results. With no bond-slip, the head

carries less force in the FE model than what was observed in the experiments. This was true for both the pull-out test and the beam bending test.

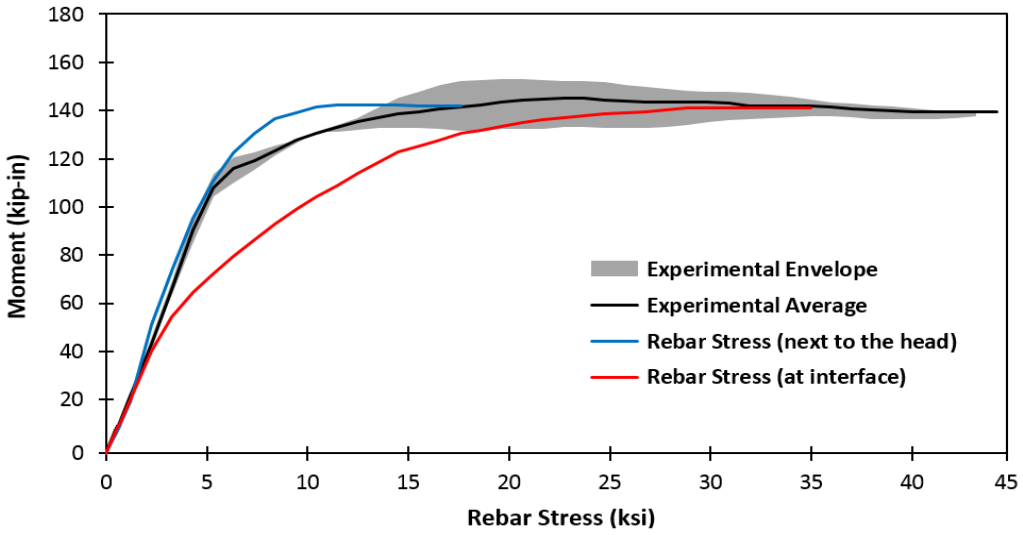

Figure ES3. Moment vs. rebar stress for the three-point bending test.

Next, a bridge with Deck Bulb-T girders connected with Mix D was modeled in ANSYS. This bridge is the new design of the SH-36 Bridge over Bear River near Preston, Idaho. For this task linear-elastic behavior was considered. The closure pour connection performed well under three AASHTO limit states: (1) Strength I Limit State for flexural capacity; (2) Service I Limit State for controlling flexural cracking; and (3) Fatigue I Limit State for infinite load-induced fatigue life.

Conclusions and Future Work

The experimental laboratory work consisting of small specimen testing and larger samples with headed bars were all completed. The FE results were very good in the linear regions, but the beam FE model in the nonlinear portion could be improved. Analysis of the ITD's 10-in. closure pour behavior with Mix D longitudinally placed between precast girders of a bridge met all the applicable AASHTO limit state design requirements.

The second phase of this project has been approved. This phase involves instrumenting the SH-36 Bridge over Bear River with strain gages placed over the headed bars and on the concrete surface below the bridge deck along a transverse section close to the southwest abutment. Early in 2018, the bridge girders were fabricated. They will be installed during the summer and early fall 2018. In May 2018, the bridge girder headed bars were instrumented in the precasting yard. Based on the results of the first phase, headed bars were instrumented next to the head and next to the precast interface. The closure pour material for this bridge is a mix similar to Mix D. Among the tasks planned are: strain data measurement in the bridge under a known truck load, data acquisition under commercial truck loading, data analysis, and refining the FE model of the ITD's 10-in. closure pour detail.

Chapter 1
Introduction

Description of the Problem

Accelerated Bridge Construction (ABC) methods are relatively new in the U.S. and Idaho. ABC requires that bridge precast concrete components be effectively connected to one another in the field. To this end, there is currently a growing nationwide trend to use Ultra-High Performance Concrete (UHPC) for field connections. There have been several experimental tests showing that precast bridge deck panels or girders may be effectively connected by placing UHPC in 6-in. wide closure pours between the precast elements. UHPC allows full strength development of #6 bars extended from precast elements into the narrow 6-in. closure pours. Although UHPC is an excellent material with a compressive strength of up to 30 ksi, it has the following disadvantages:

- It is a proprietary material with an installed cost of $10,000-$15,000 per cubic yard based on actual bid prices for UHPC in Idaho Transportation Department bridge projects between 2016 and 2018.
- Its proper installation requires very rigorous preparation and quality control, which at times may be difficult to achieve.
- It is extremely fast setting and thus it must be batched in small quantities.
- It requires special portable field mixing equipment, and as such is labor intensive.
- Because of its initial consistency (i.e., it is quite “watery”), its placement on steep grades is problematic.

As an alternative, ITD is proposing to place High-Early Strength (HES) concrete with fibers (with a minimum compressive strength of 5 ksi in 28 days) in the 10-in. closure pours between girders. The advantages of this approach are:

- HES concrete with fibers can be batched in the ready mix plant, brought to the field in the mixing truck, and placed similar to a conventional concrete.
- ITD allows removal of forms for HES concrete after one day, while for UHPC a minimum curing time of four days and a compressive strength of 14 ksi is required before removal of the forms.
- The cost is not much higher than the cost of conventional concrete ($600-$700 per cubic yard). The estimated cost saving versus the use of UHPC or high strength mortar for one project alone is approximately $100,000.

Regarding the first item above (i.e., fibers in HES concrete), it should be noted that HES concrete has high cement content in order to accelerate curing. This creates high hydration temperatures causing shrinkage cracks. The primary reason that ITD prefers adding fibers is to reduce shrinkage cracks. The fibers are not intended to increase compressive or tensile strengths of the concrete.

Regarding the second item above (i.e., removal of forms for HES concrete after one day), ITD requires that HES concrete to have a compressive strength of 3 ksi in 24 hours. Only when this strength is met, the forms can be removed. In addition, the ITD bridge plans require that the traffic cannot be placed on top of the girders before HES closure pour and end diaphragm concretes achieve 5 ksi compressive strength. The HES concrete usually achieves 5 ksi compressive strength within 7 days. In practice, it usually takes more than 7 days before the bridge is open to traffic after placing closure pours between girders. Although ITD's 50AF concrete is specified to have a minimum strength of 5 ksi in 28 days, typically a strength of 8 ksi is achieved within this time frame, which closely matches ITD's required concrete strengths for precast elements.

Project Objectives

The project objectives are:

- Obtain experimental data on the behavior of several mixes containing HES concrete Class 50AF with and without polypropylene fibers and select the optimum mix for use as a closure pour material between Deck Bulb-T Girders.
- Use the experimental results to create a computer model of the proposed closure pour detail that (a) is capable of assessing the connection strength under one-time truck load; and (b) can provide an indication of fatigue performance under repeated loading.

Project Tasks

The project tasks are:

- Task 1: Perform a literature review on the connections used in precast bridge deck components.
- Task 2: In collaboration with ITD Technical Advisory Committee (TAC), select high-early strength concrete mixes with and without polypropylene fibers. Determine compressive strength, tensile strength, and shrinkage behavior of the concrete mixes. Select the optimum mix. For computer modeling, obtain the modulus of elasticity and Poisson's ratio of the optimum mix.
- Task 3: Obtain bond strength between the optimum mix and the precast concrete. In addition, perform headed bar tensile strength tests in a closure pour connection. The specimen is to represent the lower half portion of a closure pour section.
- Task 4: Perform three-point and four-point flexural tests of beams composed of two precast segments with the optimum mix closure pour segment in the middle. The ITD's 10-in. closure pour detail is to be used for the beam specimens.
- Task 5: Develop finite element (FE) models for headed bar pull-out specimen as well as the beam specimens and compare results with the experimental results. In addition, investigate the adequacy of the connection with the optimum mix between Deck Bulb-T girders of a span in a typical bridge. Using the AASHTO LRFD design requirements, check adequacy of connection for Strength I, Service I, and Fatigue I Limit States.
- Task 6: Make a presentation to the ITD Bridge Section staff describing the project and results.

- Task 7: Submit the final project report.

This report presents Tasks 1 to 5.

Report Overview

This report is divided into seven chapters:

- Chapter 1 presented an introduction to the research problem, the objectives, and project tasks.
- Chapter 2 presents the literature review.
- Chapter 3 presents experimental work methodology, equipment used and data analysis.
- Chapter 4 presents the laboratory experimental results.
- Chapter 5 describes the finite element modeling of specimens tested in the laboratory. It also provides a summary of comparison of the FE and experimental results.
- Chapter 6 presents a bridge computer model and AASHTO LRFD design requirements.
- Chapter 7 presents a summary, conclusions and future work.

Chapter 2
Literature Review

Introduction

The literature review will examine prior research that is applicable to this project. There are five main sections within this chapter. The first section gives an overview of the field-cast connections of Prefabricated Bridge Elements (PBE). It includes components made with UHPC as well as alternative connection materials available, specifically high-early-strength concrete with fibers. The second section reviews literature relating to testing methods with a comprehensive breakdown of research done in areas of shrinkage and bond strength. The third section addresses the sample preparation of concrete specimens. This section reviews surface preparation as well as moisture at the interface. The fourth section examines the materials needed for the closure pour including bonding agent and polypropylene fibers. The fifth section provides literature review on information needed for computer modeling, including experimental and numerical research on the bond between reinforcing bars and concrete. The chapter concludes with a summary of the literature review and application to this project.

Field-Cast Connections

Field-cast connections are a necessary component for ABC. These components, which are cast in the field, connect the prefabricated bridge elements together. The most common materials utilized for field-cast connections are high-strength grouts and UHPC. Field-cast connections have been used for a variety of bridge components including cap beams, bridge girders (i.e. deck bulb-T), and deck panels. This research is limited to the connection between deck bulb-T girders. Depicted in Figure 1 are a typical cross-section of a prestressed concrete bridge and a view of the closure pour connection detail. The connection detail shows the interlacing rebars and closure pour concrete. As the connection detail becomes more complex, rebar can start to limit the amount of space inside the closure which causes congestion and can make construction and pouring more difficult. Two examples of connection details are shown in Figure 2. Ways to alleviate the rebar congestion problem are to design better connection details as well as to use materials suited to the application. Material flowability is important for consolidation and placement within the connection.

Grout is used as a material for field-cast connections due to its good flowability. Non-shrink Cementitious Grout (NSCG) was developed to mitigate the material shrinkage cracking. Although grout has been used extensively, other materials have been used to reduce the cost of the bridge either construction or lifetime costs as a result of improved performance of the connection. As a viable alternative in PBE connections, UHPC has increased in popularity with its application to ABC and is further discussed in the next section.

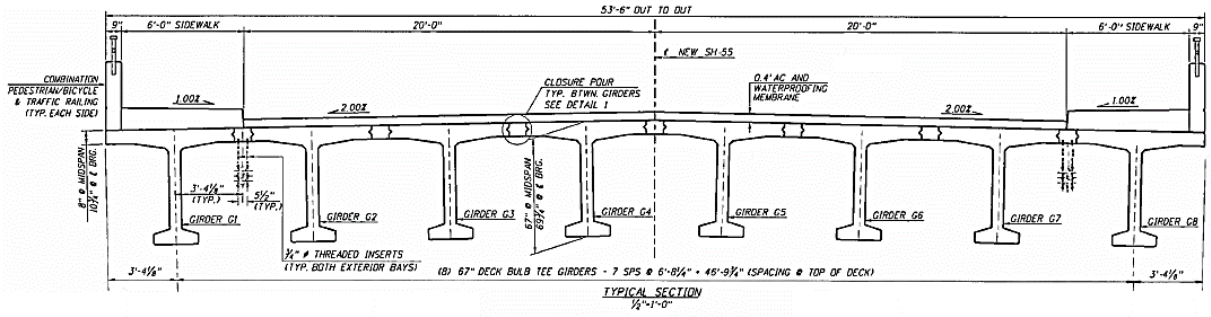

(a) Typical cross-section view

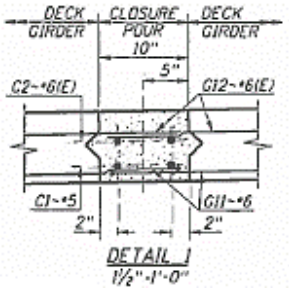

(b) Closure pour detail

Figure 1. Drawing of SH-55 over Payette River Bridge in Cascade, Idaho. (NTS) (Drawings from the Idaho Transportation Department, Bridge Section).

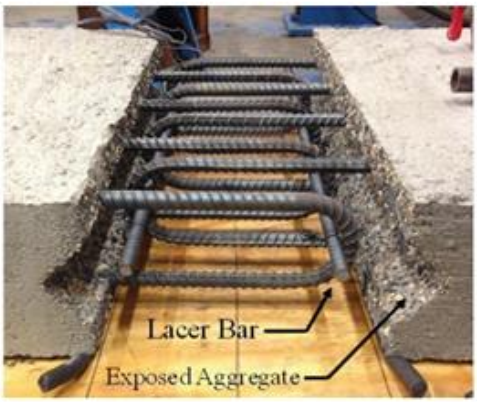

(a) U-Bar

(b) Interlaced straight

Figure 2. Sample closure connection details.[2]

Ultra-High Performance Concrete (UHPC)

Standard tests have shown that UHPC is suited for applications in bridge construction. Graybeal (2014) reported a UHPC with a compressive strength of 24 ksi, split tensile strength of 1.3 ksi, and long-term drying shrinkage of 550 microstrain.[3] These values far exceed typical normal weight concrete values of 4 ksi and 0.4 ksi, for compressive and tensile strengths, respectively. The high strength values, low

shrinkage, and good durability of the UHPC make it an ideal material to use for connecting precast concrete bridge components. Although UHPC is gaining popularity, it is still not as readily available as normal weight concrete, and it is a proprietary product. This, along with extensive preparation and installation work, make the cost of UHPC high, ranging between $2,000 and $4,000 per cubic yard.[4, 3] According to ITD the installed cost (i.e., material and labor) of UHPC is approximately $15,000 per cubic yard. Given the literature, UHPC will be used as a comparison to evaluate the proposed concrete mix in terms of performance and overall costs. A number of studies conducted by Graybeal (2010) have investigated the performance of UHPC in PBE connections.[5] In the same study, Graybeal examined the performance of large-scale panels with typical closure pour connections shown in Figure 2. In that study, the researchers subjected the panels to cyclic and static structural loading. Another study determined that UHPC outperformed grout in PBE connections (Haber, et al. 2016).[2] Researchers found similar results when comparing multiple UHPC concretes and NSCG (Haber and Graybeal 2016).[6] Despite the advantages of UHPC, there still remains a cost-prohibitive element to its use.

Alternative Materials

A proposed alternative to UHPC is high-early strength concrete with fibers. According to ITD bridge engineers the cost of using HES concrete is comparable to conventional concrete ($600-$700 per cubic yard). The estimated cost saving of using HES over UHPC can range from $50,000 to $100,000. Although most research involving prefabricated bridge element connections focuses on the use of grout and UHPC materials for field-cast connections, there is insufficient research involving a more conventional high-early strength concrete mix. The only significant research found was a study conducted for the Virginia Department of Transportation (VDOT) by Hoomes et al. (2017) which evaluated high-performance fiber-reinforced concrete (HPFRC) for bridge deck connections and joints, including closure pours.[7] Their research was focused on cracking and crack opening which occurs between link slabs in bridges. An example of a UHPC link slab connection detail is depicted in Figure 3.

Hoomes et al. determined the most advantageous mix based on performance and respective costs. Performance parameters included: bond strength, flexural toughness, deflection hardening, shrinkage, and fresh concrete properties.[7] The study concluded that Hybrid Fiber Reinforced Concrete (HyFRC) containing polypropylene and PVA performed to specifications. The total fiber content for this mixture was 2% by volume. The higher dosage of fibers reduced workability and needed increased amounts of high-range water-reducing admixture, which caused segregation of aggregates. Although it was not the highest performing mix, it was the most economical and user-friendly. VDOT has shown an interest for alternative materials, specifically (HES) concrete, for use in bridges. VDOT has used HES concrete in connecting prefabricated deck components in several bridge projects.

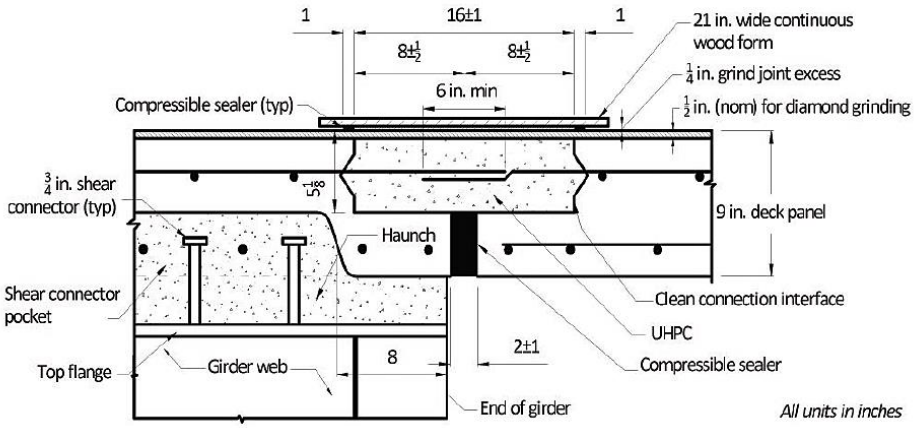

Figure 3. UHPC link slab connection detail on SR962G Bridge in Owego, NY (Graybeal, 2014).[3]

Testing Methods

Shrinkage

Shrinkage in concrete is the reduction in volume due to loss of water. This occurs in the early age, in its plastic state prior to hardening, and over long term, after the concrete hardens. Early-age shrinkage is also known as plastic shrinkage and the long-term shrinkage is mainly due to drying shrinkage (Mamlouk and Zaniewski, 2017).[8] Plastic shrinkage can be controlled by preventing the loss of water, from evaporation of surface moisture or absorption of concrete forms, until the concrete has set. Excessive volume change can cause cracks, known as shrinkage cracks, in the concrete which increases permeability. Minimizing shrinkage is important particularly in connections for PBE. Shrinkage reducing admixtures and fibers significantly reduce cracking.

The standard test method for shrinkage is ASTM C157, *Standard Test Method for Length Change of Hardened Hydraulic-Cement Mortar and Concrete*.[9] A prismatic beam of 3 in. x 3 in. cross-section and 11.25 in. length with gage studs embedded into the ends is used for this method. This test measures the length change after the concrete has hardened and cured for a set amount of time. Most often the drying shrinkage is reported. Graybeal (2014) reported the long-term shrinkage for UHPC at 550 microstrain, which is used as a comparison value for this study.[3]

Bond between Precast Concrete and Field-cast Material

This section examines the methods used to evaluate bond strength and the different factors that contribute to bond behavior. Durability of connections utilized in PBE is critical to the overall performance of the bridge. Poor bond between precast concrete and field-cast concrete could result in cracks at the interface allowing water to penetrate into the deck and cause damage. Some of the research discussed here investigate specific applications and may not directly apply to the current study but they will still be used to evaluate bond performance.

Common tests for determining bond strength are flexural beam, splitting cylinder, slant-shear, and direct tension pull-off.[6, 10, 11, 12, 13, 14, 15] These tests are based on ASTM standard test methods. Bond strength tests are shown in Figure 4. All test specimens use segments of previously cast concrete (e.g. precast or another concrete base) and connection material (e.g. grout, UHPC, or new concrete). These tests are intended to determine the bond behavior of the interface between the two materials.

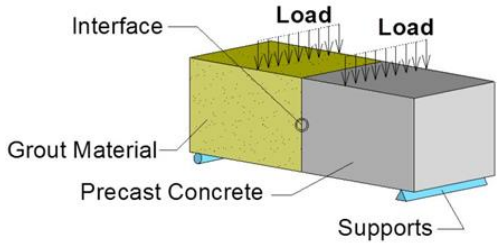

(a) Flexural beam test

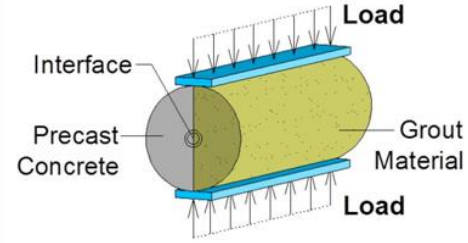

(b) Splitting cylinder test

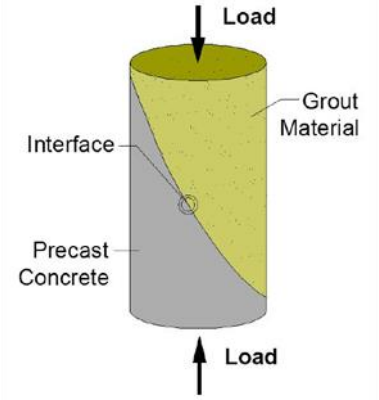

(c) Slant-shear compression test

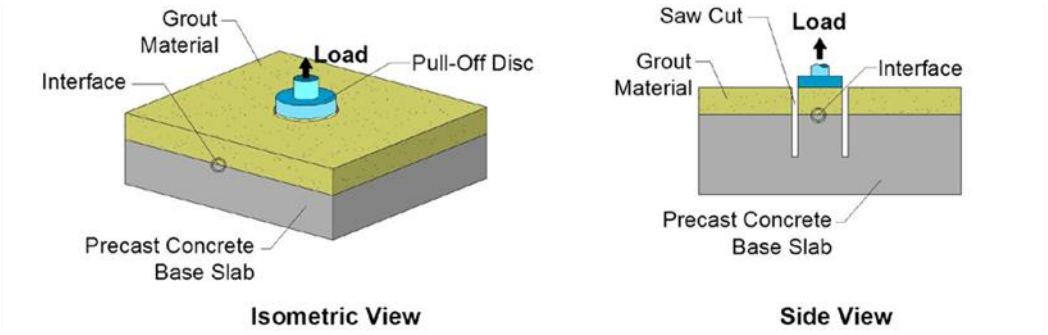

(d) Direct tension pull-off test

Figure 4. Tests for characterizing bond between precast concrete and field-cast connection material (De la Varga et al. 2017).[11]

Each test method puts the interface into a different state of stress (e.g. flexure, tensile, or shear). The flexural beam test (Figure 4a) is based on ASTM C78, *Standard Test Method for Flexural Strength of Concrete (Using Simple Beam with Third-Point Loading)*. This test is performed on a 6 in. x 6 in. x 21 in. composite beam with one half containing the base material and the other half containing the closure material. Third-point loading is applied and this test puts the bottom portion of interface into a state of

flexural tension. Splitting cylinder (Figure 4b) is based on ASTM C496, *Standard Test Method for Splitting Tensile Strength of Cylindrical Concrete Specimens*.[16] This test uses a 4 in. x 8 in. or 6 in. x 12 in. composite cylinder with halves consisting of the base material and the closure material. A load is applied along the length of the cylinder putting the interface into indirect tension. Slant-shear test (Figure 4c) is based on ASTM C882, *Standard Test Method for Bond Strength of Epoxy-Resin Systems Used with Concrete by Slant Shear*.[17] This test uses a slant cylinder in which the halves are cast such that a slant face is produced to apply a combination of shear and compression at the interface. The direct tension pull-off test (Figure 4d) follows ASTM C1583, *Standard Test Method for Tensile Strength of Concrete Surfaces and the Bond Strength or Tensile Strength of Concrete Repair and Overlay Materials by Direct Tension (Pull-Off Method)*.[18] Specimens consist of a base concrete slab and a 2 in. thick overlay of the connection material. A steel disc is then glued to the top surface and a partially-cored hole is drilled approximately 1 in. into the base concrete. This test puts the interface into direct tension. Bond strength can be difficult to determine because there are multiple testing methods that can be used, therefore a test method should be selected based on the anticipated stresses in the field. Due to the number of variations that can contribute to bond strength, some researchers investigating bond performance have employed several of the test methods of Figure 3 in their studies.[10, 11, 18] The optimal test method for determining bond strength is the flexural beam test, ASTM C78, because it best simulates loading in the field.

Some research has concluded that these tests may not be the true bond strength due to a number of factors. These factors include: precast substrate surface preparation, pre-wetting substrate, surface cleanliness, differential shrinkage, and differential stiffness.[8, 9, 20] Some of these factors will be discussed in the next section.

Precast Concrete Interface Surface Preparation

This section presents literature on improving bond strength between precast concrete and closure material. Two of the most important factors are surface roughness and moisture at the interface.

Surface Preparation

Researchers agree that substrate (i.e., base material) surface preparation has a significant role in terms of bond strength (De la Varga et al. 2016; De la Varga et al. 2017; Julio et al. 2004; Santos and Julio 2011; Tayeh et al. 2013).[1, 11, 19, 20, 21] One component to surface preparation involves roughening of the substrate surface which increases the contact area for the new concrete to bond. In general, research shows that the greater the surface roughness, the higher the bond strength.[11] Surface preparation methods include wire brushing, jack hammering, pressure washing, sand blasting, and exposing the aggregate of the precast concrete.[1, 21] The research has shown that exposed aggregate surface preparation is the best method for ensuring the best bond strength.

Moisture at the Interface

Presence of moisture also affects bond strength (De la Varga et al. 2017; Bentz et al. 2017; Julio et al. 2005; Emmons 1994).[11, 10, 22, 12] This refers to the surface moisture prior to casting the connection concrete. Research has revealed opposing conclusions about the need for moisture at the substrate. These opposing ideas are often attributed to the testing method that is used. Bentz et al. (2017) conducted tests on sets of slant-shear and direct tension specimens that were prepared with different substrate finishes and moisture conditions.[10] In the study Bentz et al. employed neutron and X-ray radiography to examine the dynamic microstructural rearrangements occurring at the interface during curing (i.e. identifying the water movement and densification between the two materials). The two bond tests, slant-shear and direct tension, produced different results. Slant-shear tests resulted in higher bond strength compared to direct pull-off tests when the substrate was dry. Conversely, when the substrate was Saturated Surface Dry (SSD), direct pull-off tests had higher bond strengths compared to slant-shear (Bentz et al.). For the dry substrate case, the flow of water from the repair material to the substrate causes densification of the layer and this may be the cause of higher slant-shear results. For the moist condition, the excess water provided for better hydration and consolidation for the RM resulting in higher direct pull-off values.

Materials

Bonding Agent

A bonding agent is a liquid compound applied to a concrete substrate to promote good bonding to new or repair concrete. Bonding agents are latex or epoxy based. Literature involving use of bonding agents was intended for concrete repair and overlay material applications. Emmons (1994) suggests not using a bonding agent because it can produce a vapor barrier that could result in failure.[12] The experimental study by Julio et al. (2005) consisted of preparing sets of slant-shear specimens with each pair treated with a different substrate finish (e.g. as-cast, wire-brushing, partially chipped, and sand-blasted).[22] The research group concluded that a bonding agent is not necessary, provided the surface roughness is adequate. The sand-blasted specimen without a bonding agent performed better than the specimen with a bonding agent. From the literature, use of bonding agents may not be beneficial, particularly because the applications for bonding agents were mainly for repair or overlays. These types of applications induce shear and direct tension stresses at the interface rather than primarily flexural tension stress encountered in the current project.

Several commercially available bonding agents were compared for use with the current study. There are two types of bonding agents, re-emulsifiable and non-re-emulsifiable that act differently in the presence of water. In this study the researchers chose to only compare re-emulsifiable bonding agents because of their property to re-wet after initial application, a preferable method in the field. Bonding agents from four different companies were evaluated and compared based on the data provided by each company for their products. The comparisons of these products were problematic since there are multiple testing methods used to determine bond strength of a bonding agent. These testing methods included ASTM C1059, *Standard Specification for Latex Agents for Bonding Fresh to Hardened Concrete*, and ASTM

C1042, *Standard Test Method for Bond Strength of Latex Systems Used With Concrete By Slant Shear*.[23, 24] Bond strengths for each bonding agent were also compared. Table 1 lists the bonding agents that were compared and the strength data from the data sheets provided by the company. No strength information was given for MasterProtect P110. Products from Sika and US Mix Company were much lower than that of Euclid. In this study the bonding agent Tammsweld produced by Euclid Chemical Company was selected because of its highest bond strength value of 4,600 psi.

Table 1. Bonding agent comparison.

Company	Product	Strength	ASTM
BASF	MasterProtect P110	N/A	N/A
Euclid Chemical Company	Tammsweld	4,600 psi	C1042
Sika	SikaLiquid Weld	1,300 psi	C1059
US Mix Company	Multi-55	14-day strength, Type I: 1,700 psi Type II: 1,300 psi	C1042

Polypropylene Fibers

One of the most important materials in this study is fibers. Fibers are produced from a variety of materials including steel, glass, synthetic, and naturally occurring substances. Depending on the application of the concrete mix, a particular fiber might be more suitable. Fibers that are commonly used are steel and synthetic. Steel fibers would be added to a mix to increase tensile capacity for use in structural applications (Graybeal 2014).[3] A synthetic fiber, such as polypropylene, may be added to control cracking (Ahmed et al. 2006; Banthia and Gupta 2006; Madhavi, Raju, and Mathur 2014; Serdar et al. 2015).[25, 26, 27, 28] Fibers are typically used for secondary reinforcing (i.e. for crack control), as opposed to conventional methods such as wire mesh. The current study is focused on the use of polypropylene fibers.

Polypropylene fibers have been a topic of interest in recent years due to their versatility. Polypropylene fibers have a number of properties which include: low specific gravity (S.G. = 0.91), high tensile capacity (80 ksi to 101 ksi), and high acid and salt resistance. In addition, they are nonabsorbent, noncorrosive, and chemically inert, meaning not reacting with concrete admixtures (Banthia and Gupta 2006; Kakooei et al. 2012; Serdar et al. 2015).[26, 29, 28] Fiber lengths typically range from 0.25-2.5 in., and can be either monofilament, consisting of single strands, or fibrillated, a bundle of strands. Polypropylene fibers can be implemented into any concrete mix, are readily accessible, and are inexpensive, making them a suitable option for many applications, including bridge construction. When determining the appropriate mix, fiber dosage needs to be considered.

Research has shown an optimum range of fiber dosage for concrete. Due to the variability of concrete mixes and types of fibers used in each study the general findings and conclusion will be presented. Tests

conducted by Ahmed et al. (2006) examined fiber dosage rates of 1, 2, and 3 lb/yd^3 (fiber dosage is in pounds of fiber per cubic yard of concrete).[25] Compressive strength and splitting tensile strength increased with increasing fiber content up to 2 lb/yd^3, and a decrease in strength at 3 lb/yd^3.[25] Ahmed et al. also showed a reduction in shrinkage cracking of 83% and 85% with the addition of 2 lb/yd^3 and 3 lb/yd^3, respectively. Experimental work conducted by Kakooei et al. (2012) also observed an increase in compressive strength with a fiber volume of 1.5-2 kg/m^3 (2.5-3.4 lb/yd^3).[29]

Besides the fiber dosage, the actual fiber type can affect the concrete performance. A study by Banthia and Gupta (2006) concluded that the geometry of the fibers is important for optimizing shrinkage reduction.[26] Fiber dosage rates used were 0.1% (1.5 lb/yd^3), 0.2% (3.1 lb/yd^3), and 0.3% (4.6 lb/yd^3) by volume. They tested four different fiber products and had a control test for a baseline to determine shrinkage crack reduction. The researchers concluded that longer, finer-sized fibers were better at reducing crack widths, and fibrillated fibers were better at controlling shrinkage cracking than monofilament fibers.[26]

Manufacturers provide recommended dosages which range between 1-1.5 lb/yd^3.[27] At higher fiber dosages, workability is reduced, but this can be remedied with the use of a plasticizer. Using polypropylene fibers benefits the concrete in its plastic state and after hardening. Fibers hold the mix together while the concrete is still fresh, or plastic, reducing the possibility of segregation and bleeding. Segregation is the tendency of the heavier coarse aggregates to move toward the bottom of the concrete. Bleeding is a form of segregation; it is when the water in the mix rises to the surface because it is lighter than the other constituents. Fibers also reduce the shrinkage cracking. In addition, fibers improve the properties of hardened concrete, including: reducing drying shrinkage, increasing resistance to abrasion and freeze-thaw, increasing impact resistance, and restraining cracking.

Experimental and Numerical Literature for Computer Modeling

This section provides literature review of experimental and numerical research for finite element modeling of the closure pour connection detail suggested by ITD and used in this study. More details on this section are provided in the thesis by Rashique, U. (2018).[30]

Bond Strength of Reinforcing Bars in Concrete

The issue with the steel-concrete bond has been extensively researched since the nineteenth century. As a result, deformed, bent, twisted and headed bars were introduced for better bond strength. The highly nonlinear and inelastic behavior of concrete and bar slip makes the analytical study of bond-slip behavior difficult.

Mathey and Watstein (1961) conducted experiments on 18 beams and 18 pull-out specimens with deformed reinforcing bars and reported on bond strength.[31] Lutz and Gergely (1967) studied the effect of the rib face angle on the bond slip.[32] Goto (1971) studied the internal cracks around the reinforcing bar.[33] Nilson (1972) proposed a slip function for reinforcing steel.[34] Rao, et al. (2007) tested forty pull-out specimens for bond strength and its variation.[35] It was observed that ideal pull-out failure occurred

in all the specimens with confinement, while the unconfined specimens failed by longitudinal splitting of concrete. The maximum bond strength of unconfined concrete was found to be between 50% and 60% of that with confinement.

Headed reinforcing bar is a relatively new technology and only a few literature on bond behavior is available. Research by Fynboe and Thorenfeldt (1986), Eligenhausen (1996) and others has shown that headed bars have better bond-slip response than hooked and bent bars under monotonic and cyclic loading.[36, 37] The headed bar can fail by yielding or fracture. Two other failure modes involving concrete failure are pull-out cone failure and side blowout failure as shown in Figure 5.

One of the most extensive works on strength of headed reinforcing bars was carried out by DeVries (1996).[38] They conducted pull-out tests on 140 samples and investigated the effects of variables such as embedment depth, clear cover over the bar, spacing of adjacent bars and orientation of the heads on bond behavior. The tests were done for both shallow and deep embedments. Shallow embedment was defined by the ratio of the embedment length to side cover being less than five. Various bar sizes and yield strengths were used. In shallow embedment tests, some bars reached the yield stress plateau and went into strain hardening. But in general, bar yielding did not have a significant effect on the ultimate pull-out load. Also, the observed result showed a trend that the bars with development length had higher pull-out loads than the bars with no development length. The no development length condition was achieved by covering the bars with PVC pipes, thus not allowing the bar to bond with concrete. This causes only the head being able to resist the pull-out force. While the edge distance was found to be a factor in controlling the size of the failure cone, it was also found that bars closer to the edge had relatively smaller pull-out load capacity. Wright and McCabe (1997) performed similar work as DeVries on headed bars.[39] They conducted extensive research on the effect of anchorage length and transverse reinforcement on the behavior of headed bars.

Thompson, et al. (2006) tested 27 lap-splice specimens with headed bars.[40] A typical specimen is shown in Figure 6. As depicted in Figure 7, it was found that internal cracks always tend to propagate from the head of one bar towards the opposing bar at an angle of 55 degrees measured from the bar axis. On the other end, a well-defined, concrete wedge forms at the head of the opposing bar.

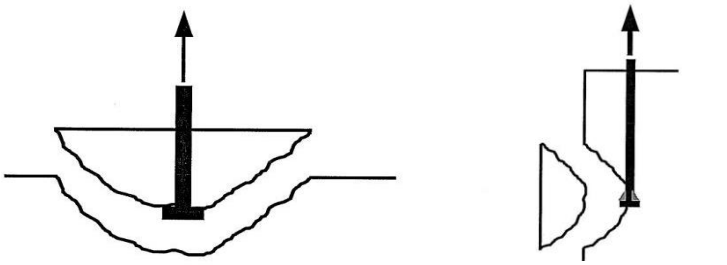

(a) Pull-out cone failure **(b) Side blowout failure**

Figure 5. Concrete failure modes.[38]

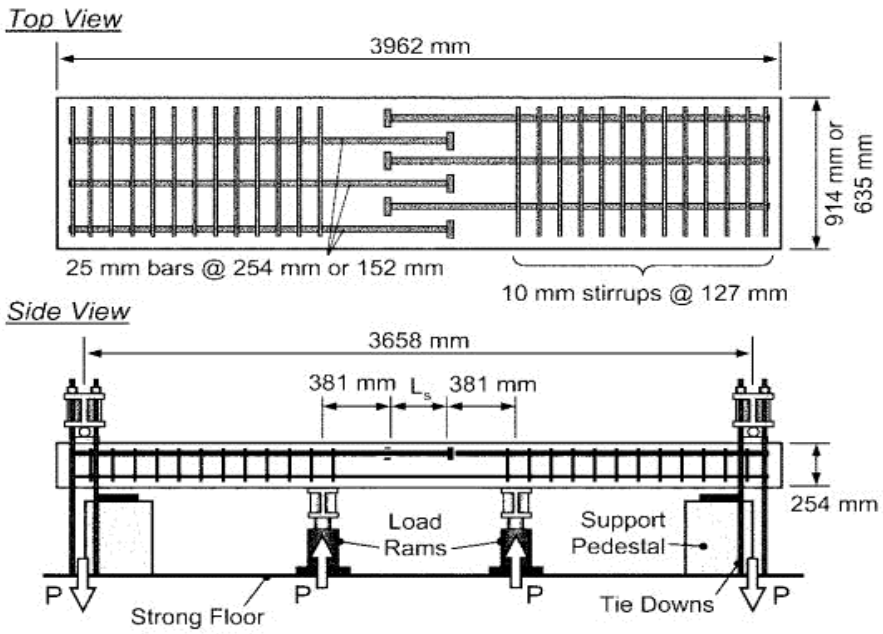

Figure 6. Typical lap-splice specimen used by Thompson et al., 2006.[40]

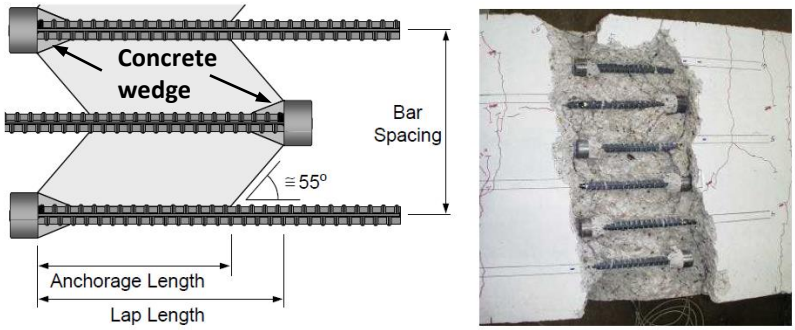

(a) Strut model for lap splices **(b) A tested specimen**

Figure 7. Mechanism of force transfer between opposing lapped bars (Thompson et al., 2006).[40]

The experimental work on headed bars found in the literature can be used to compare general behavior with the laboratory samples used in this study. And, they can be used to calibrate the Finite Element (FE) model.

Numerical Modeling

Numerical modeling of reinforcing bar bond slip has been carried out by several researchers. A brief summary is given here. For more details, refer to thesis by Rashique, U. (2018).[30]

Ngo and Scordelis (1967) proposed a simple two-dimensional bond element. Two orthogonal spring elements were used to connect the adjacent steel and concrete node pair.[41] The springs had no physical dimension which means the adjacent steel and concrete nodes could occupy the same location.

Dinges (1983) proposed a generalized contact element with two double nodes and a linear shape function.[42] Keuser & Mehlhorn (1988) analyzed the aforementioned bond-link element (Ngo & Scordelis) and contact element (Dinges) behavior with five shape functions.[43] They concluded that the accuracy of the results can be increased by using higher order polynomials for displacement functions.

From the experiments on axially loaded cylinders, Doerr (1980) derived a bond stress-slip relationship where the bond shear stress was related to concrete tensile strength and bar slip.[44] Keuser & Mehlhorn (1988), used the equations proposed by Doerr (1980) and Martin (1973), and compared them to the results obtained by FE analysis using the bond-link element with constant stiffness developed by Ngo and Scordelis (1967).[43, 44, 45, 41] It was concluded that bond elements with constant shape function and linear elastic material properties cannot model the steel-concrete bond-slip behavior with sufficient accuracy.

A large portion of the bond-slip nonlinearity arises from the primary and secondary cracks. As a consequence, research was carried out to develop Linear Elastic Fracture Mechanics (LEFM) model for steel-concrete bond. Ingraffea, et al. (1984) studied the efficacy of LEFM models in the FE analysis of steel-concrete bond.[46] While LEFM works well for metals and many rocks, it was considered not accurate in case of concrete.

Another bond model using plasticity theory incorporating the effects of mechanical interaction and secondary cracks was developed by Cox and Hermann (1998).[47] This was a two-dimensional axisymmetric model in "bar scale", i.e., the concrete and the bar were modeled separately, but for simplification, the ribs in the bar were not modeled. While Ingraffea et al. (1984) considered the effect of cracking on horizontal displacement of the bar, Cox and Hermann (1998) considered the relative movement of concrete in bond zone in both the horizontal direction and the normal direction (bond zone dilation). Figure 8 depicts an idealized deformation of the bond zone.

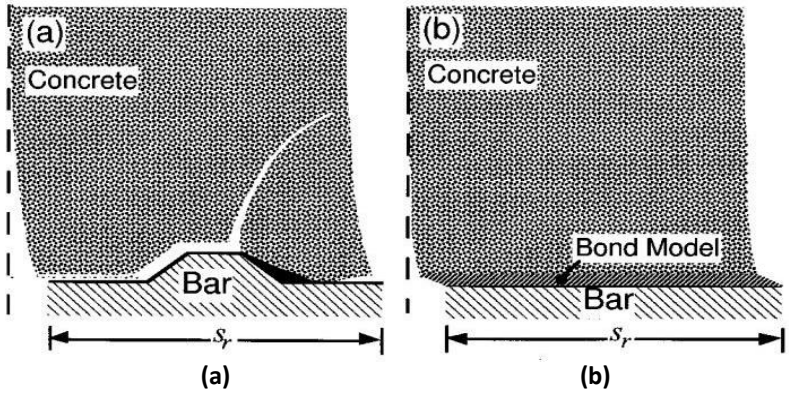

Figure 8. Deformation of bond zone: (a) actual, (b) idealized model (Cox and Hermann, 1998).[47]

In a recent study, a bond-slip relationship was developed by Hong et al. (2008) in which the bond stress (i.e., shear stress per unit interface area) is expressed as a function of concrete compressive

strength, bar diameter, and the amount of slip. This equation was developed using a set of experimental results.[48]

Although, many researchers have developed numerical models to simulate the bond-slip behavior of steel and concrete, no single model was able to incorporate all the factors affecting bond-slip response. Thus, the FE modeling of the laboratory specimens in this study remains a challenging task. Past experience has shown that if there are too many nonlinearities in a FE model (material, contact elements, large deformation, etc.), the models will have more difficulty with solution convergence. Therefore, it is important to use a simple bond-slip model.

Summary

The literature review examined numerous studies and offered valuable insight into the current study. Based on the literature reviewed, the following key points are found:

1. High performance fiber reinforced concrete has been used as an alternate material to UHPC in connecting certain bridge precast components by the Virginia Department of Transportation.
2. ASTM C-157 is an adequate method for determining the drying shrinkage of concrete specimens.
3. There are several test methods in determining bond strength. The flexural beam test, ASTM C-78, was chosen for this study because it simulates loading in the field.
4. Based on the performance and ease of application, the optimum surface preparation is the exposed aggregate finish.
5. Saturated surface dry moisture condition at the interface is suggested to provide the best bond performance.
6. Bonding agents are primarily used for applications involving repair or overlays.
7. Polypropylene fibers proved to be a suitable option based on performance, availability, and cost.
8. The experimental work on headed bars can be used for comparison with experimental work in this study and to calibrate the FE models.
9. A simple model of bond-slip is preferable in the FE modeling, especially in the context of this research.

Chapter 3
Experimental Work Methodology and Data Acquisition

Introduction

The optimum high-early strength concrete mix was chosen based on compressive strength, splitting tensile strength, and shrinkage. Interface bond strength tests were conducted using segments of precast and optimum material. It should be noted that ITD is currently using high-early strength concrete with Polypropylene fibers in certain parts of bridges in Idaho; therefore, the materials considered in this study are readily available in Idaho.

Mix Design

This project consisted of designing a control mix and five alternate mixes. The control mix was determined by using the ACI Absolute Volume Method. Cement for this mix was Type II. The cement was supplied by Ash Grove Cement Company. Fly ash Type F was used as a cement substitute (secondary cementitious material).

To obtain high-early strength concrete, MasterSet AC 534 accelerating admixture was included. Air entrainer MasterAir AE 200 was used to control air content. High-range Water Reducer (HRWR) MasterGlenium 1466 was used. Other parameters to create the remaining mixes were Shrinkage Reducing Admixture (SRA), Bonding Admixture (BA), and Polypropylene fibers. Bonding admixture was AKKRO-7T and was supplied by Euclid Chemical Company. Shrinkage reducing admixture was MasterLife SRA 035. Polypropylene fibers were Fibermesh 150. Table 2 provides a list of the products used in the concrete mixes. Material specifications for constituents can be found in Appendix A of the thesis by Casanova, M. (2018).[49]

Table 2. Product list.

	Product	Company
Accelerating admixture	MasterSet AC 534	BASF
Air entraining admixture	MaterAir AE 200	BASF
High-range water-reducing admixture	MasterGlenium 1466	BASF
Shrinkage reducing admixture	MasterLife 035	BASF
Bonding admixture	AKKRO-7T	Euclid
Bonding agent	Tammsweld	Euclid
Polypropylene Fiber	Fibermesh 150	Fibermesh

Table 3 shows the mix design variables which were developed in consultation with the ITD Technical Advisory Committee. Trial batches mixed in the laboratory were also helpful in determining admixture and fiber dosages. During trial batches, workability significantly decreased with a fiber dosage of 3.0

lb/yd^3. The trial batches using a fiber dosage of 1.5 lb/yd^3 proved more workable. To avoid workability issues in the later mixes, fiber dosages of 0.75 lb/yd^3 and 1.5 lb/yd^3 were used. Accelerator dosage of 70 fl oz/cwt was determined from trial batches for the control mix to obtain the minimum 1-day compressive strength of 3,000 psi, as specified by ITD. This dosage was used for all mixes. Air entrainer was adjusted for each mix to meet the air content requirement. Mixes with bonding admixture (BA) did not require additional air entrainment. Recommended manufacturer dosages for SRA and BA were used. SRA dosage used was 1 gal/yd^3. For BA the recommended was to mix one part AKKRO-7T with three parts water (1:3). All admixture dosages were verified by the local ready mix company's owner who has served as a consultant for ISU student projects, and provided many of the materials for this research project. The control mix was developed following American Concrete Institute (ACI) absolute volume method. The mix design also followed the specifications required by ITD's *Standard Specifications for Highway Construction*.[50] Refer to Appendix B of the thesis by Casanova, M. (2018) for the mix design procedure and the appropriate ITD design parameters. The precast concrete mix design used for this research was supplied by a local precast producer.[49]

Table 3. Mix design variables.

Mix	Fibers	SRA	BA
A (Control)	-	-	-
B	0.75 lb/yd^3	-	-
C	1.5 lb/yd^3	-	-
D	1.5 lb/yd^3	✓	-
E	0.75 lb/yd^3	✓	✓
F	-	✓	✓

Note: Fibers are polypropylene fibers; SRA = shrinkage reducing admixture; BA = bonding admixture

A great deal of time was spent conducting trial batches and tests to obtain a control mix with specifications required by ITD (i.e., adjusting the admixture dosages to obtain the required one-day compressive strength, mix air content and slump). The control mix proportions are shown in Table 4. Water adjustments to the mix design were made to account for the moisture content and absorptions of the coarse and fine aggregates. Water adjustments for admixtures were also considered as per the recommendation of ITD Material's Engineer. Accelerator admixture is composed of 46.5% liquids, so the equivalent amount of water was taken out. Equivalent amounts of water were taken out with the addition of SRA or BA. The contributions of air entraining and water reducing admixtures to the adjusted water were minimal compared to the others and were ignored. The first water value shown in Table 4 is the required mix water adjusted for the moisture and absorption of the aggregates. The second value "Water used" is the amount of water adjusted for aggregates and admixtures. This value was the actual amount of mix water used during batching. Table 5 shows the summary of the admixture dosages used for each mix. More details about water adjustments and all the mix design proportions can be found in Appendix B of the thesis by Casanova, M. (2018).[49]

Table 4. Control mix (Mix A) proportions.

Water to cement ratio (w/c)	0.36	
Fine aggregate		
Moisture content	5.7	*%*
Absorption	2.1	*%*
Coarse aggregate		
Moisture content	1.9	*%*
Absorption	1.3	*%*
Water (*adjusted for moisture contents and absorption of fine and coarse aggregates*)	176	*lb/yd^3*
Water used (*adjusted for admixtures*)	156	*lb/yd^3*
Cement	528	*lb/yd^3*
Fly ash	132	*lb/yd^3*
Fine aggregate	1564	*lb/yd^3*
Coarse aggregate	1454	*lb/yd^3*
Admixture	Dosage	
Accelerator (AC)	70	*fl oz/cwt*
Air Entrainer (AE)	7	*fl oz/cwt*
Superplasticizer (HRWR)	8	*fl oz/cwt*
Shrinkage Reducing Admixture (SRA)	0	*gal/yd^3*
Bonding Admixture (BA)	0	
Fibers	0	*lb/yd^3*

Note: cwt = hundred pound weight of cementitious material

Table 5. Mix design admixture dosage summary.

Admixture	Units	A	B	C	D	E	F
AC	fl oz/cwt	70	70	70	70	70	70
AE	fl oz/cwt	7	10	10	10	-	-
HRWR	fl oz/cwt	8	8	8	8	5	6
SRA	gal/yd^3	-	-	-	1	1	1
BA	-	-	-	-	-	1:3	1:3
Fibers	lb/yd^3	-	0.75	1.5	1.5	0.75	-

Note: cwt = hundred pound weight of cementitious material

Aggregate Analysis

The aggregate for this project was supplied by Pocatello Ready Mix. Sampling of aggregates was conducted following ASTM D75, *Standard Practice for Sampling Aggregates* (ASTM 2014a). Aggregate collected from the stockpile were kept sealed in five gallon buckets to preserve their moisture content during storage. Using ASTM C566 (ASTM 2013d), the moisture content of aggregates was obtained.

Aggregate absorption was determined by following ASTM C127 and ASTM C128 for coarse and fine aggregates, respectively.[51, 52] Sieve analysis was also conducted according to ASTM C136, *Standard Test Method for Sieve Analysis of Fine and Coarse Aggregates*.[53] Moisture and absorption values were used to determine water adjustments for the mix design. Aggregate gradations met the requirements as specified by the Idaho Transportation Department.[50] Aggregate analysis data can be found in Appendix C of the thesis by Casanova, M. (2018).[49]

Sample Casting

Concrete samples were cast in accordance with ASTM C192, *Standard Practice for Making and Curing Concrete Test Specimens in the Laboratory*.[54] Before casting samples slump and air content tests were performed. Slump and air content were determined in accordance with ASTM C143 and ASTM C231, respectively. Capping of concrete cylinders followed ASTM C617, *Standard Practice for Capping Cylindrical Concrete Specimens*.[55] Concrete batching was mainly done in the laboratory with a barrel mixer. However, a mixing truck was used when a large quantity of precast concrete was needed for headed bar pull-out and flexural beam specimens. Appropriate laboratory procedures for mixing concrete were followed.

Cylinder and Shrinkage Prism Casting

Cylinders were cast for determining compressive and splitting tensile strengths. Samples were 4-in. diameter by 8-in. tall and cast using standard plastic molds. Length change prisms were cast in molds with dimensions of 3 in. x 3 in. x 11.25 in. and included anchor holes in the ends to secure gage studs. Gage studs were screwed into the ends of the mold to be cast into the specimens. Concrete molds are shown in Figure 9.

After 24 hours the samples were removed from their molds and placed in a water bath to cure. Due to the large quantity of samples to be tested, a water tank was constructed for curing, as shown in Figure 10. Concrete cylinders and shrinkage prisms were moist cured in lime-saturated water for 28 days, after which the samples were removed from the water and prepared for testing.

Interface Beam Casting

To determine the interface bond strength between precast concrete and HES concrete, a modified ASTM C78 developed by De la Varga, Haber, and Graybeal (2016) was used.[1] The modified standard uses a 6 in. x 6 in. x 21 in. composite loaded in third-point bending. See Figure 11. Specimens are made by first casting the precast segments. The precast interface was prepared next, followed by the pouring of the connection concrete. Exposed aggregate surface finish was the chosen method for precast concrete interface surface preparation. Exposing the aggregate was accomplished by the use of a concrete surface retarder, “Formula F” manufactured by Euclid Chemical Company. This product delays the setting of concrete so that the surface can be washed or scrubbed away to reveal the underlying coarse aggregate. Based on the literature review and recommendations by ITD, Saturated Surface Dry (SSD) was used for the precast interface surface.

(a) Cylinder mold

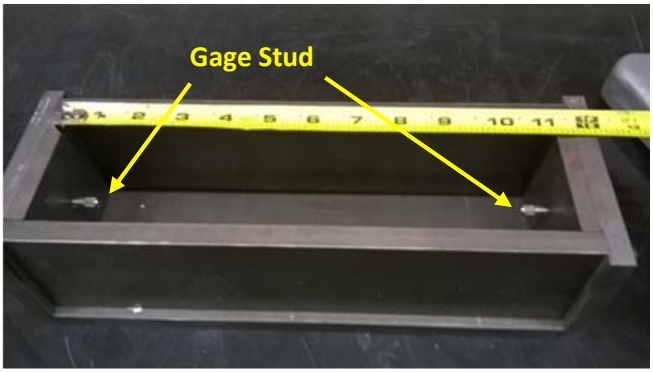

(b) Length change prism mold

Figure 9. Concrete molds.

Figure 10. Water tank for moist curing of samples.

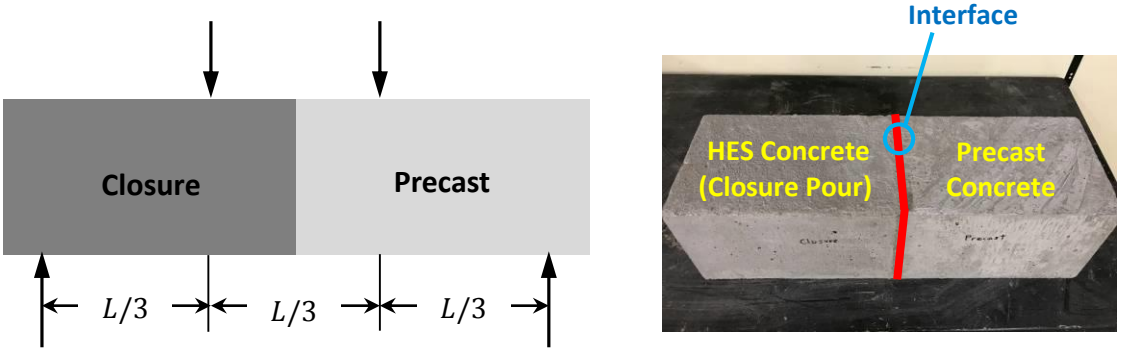

Figure 11. Interface bond specimen.

The wood mold seen in Figure 12 shows a divider in the middle that was painted with a layer of concrete surface retarder. The molds were lubricated with WD-40 to prevent concrete from sticking to the wood and promote easy mold removal, except where the concrete surface retarder was applied. The molds were filled in two lifts of equal volume and rodded 32 times for each lift. After each lift the concrete was consolidated by tapping the sides of the mold 10 to 15 times with a mallet. Once the second lift was

consolidated, the surface was troweled to achieve a smooth finish. The samples were covered with plastic to prevent water from evaporating and were allowed to cure for 24 hours. After curing, the precast segments were removed from the molds and the surface that was in contact with the concrete retarder was washed with water using a garden hose sprayer to produce an Exposed Aggregate (EA) finish as shown in Figure 13.

(a) Interface beam mold **(b) Concrete retarder on form** **(c) Precast section poured**

Figure 12. Interface bond test specimen mold.

Figure 13. Exposed aggregate surface preparation.

Wet burlap was placed around the precast concrete segments and then covered in plastic. The burlap was monitored and kept moist with a sprayer throughout the curing process. The precast sections were removed at 28 days. After removal, these sections were placed back into the molds. The molds were lubricated with WD-40 oil spray. The EA surface on the precast portion was sprayed with water to create a SSD moisture condition. Casting the HES concrete followed the same steps as the precast concrete and a similar curing method was used after specimens were removed from the molds. A second set of beam specimens were used to determine the effect of applying bonding agent at the interface. Casting and curing procedures were the same as the previous set except for the precast interface surface preparation. The precast sections were removed from curing one day before casting the HES closure concrete. The EA surfaces were dried with a heat gun then the Bonding Agent (BG), Tammsweld, was applied with a paint brush and allowed to dry before being placed back in the molds. For casting the HES

concrete, water was not sprayed over the bonding agent. Refer to Appendix M of the thesis by Casanova, M. (2018) for pictures of the casting process.[49]

Headed Bar Pull-out Specimen Casting

Headed bar pull-out tests were used to simulate the lower portion of a closure pour deck connection between Deck Bulb-T girders as shown in Figure 14. The specimen consists of precast concrete sections and the closure concrete reinforced with three headed rebars. The sequence of specimen construction is shown in Figure 15.

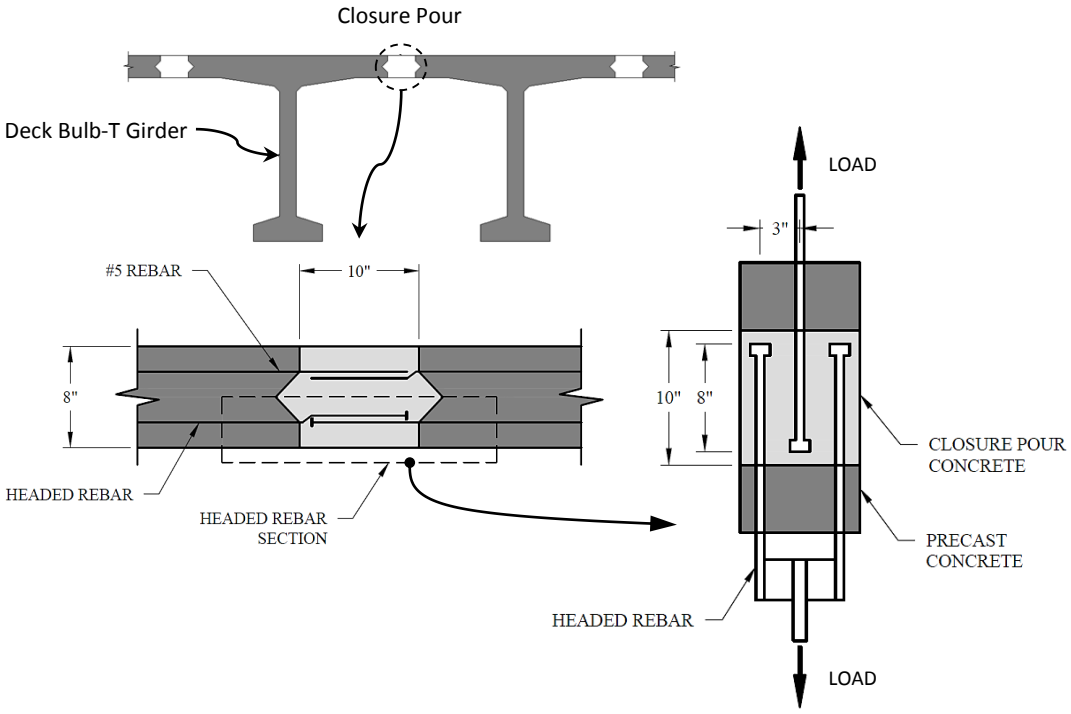

Figure 14. Headed bar pull-out specimen schematic.

Precast segments of the headed bar pull-out samples were prepared similar to the interface bond samples with the exposed aggregate surface finish. Molds were constructed from plywood. Holes were drilled for placing the rebar. Concrete surface retarder was applied to the inside face of the two precast segments. Strain gages were installed on rebar before casting concrete. Rebars were set in the molds so that the strain gages were oriented so they were facing up and down. Precast sections were poured in two lifts and rodded 25 times for each lift. After the precast concrete cured, the closure concrete was poured. Steel plates and threaded rods were welded to the ends of the sample. These were used to attach the specimen to the United tensile testing machine. Prior to testing, the front faces of the specimens were painted white and 1 in. x 1 in. grid lines were marked with a pencil. The paint helped identify cracks. Refer to Appendix M of the thesis by Casanova, M. (2018) for details regarding the casting and fabrication of the headed bar pull-out specimens.[49] Figure 15 shows the sequence of specimen fabrication; beginning with the rebar placement, then casting the precast concrete, and finally casting the closure concrete. The fabrication can be seen in Figure 16. The photos show the rebar being

placed in the wood mold, the exposed aggregate surface finish of the precast interface, and the fully cast specimen.

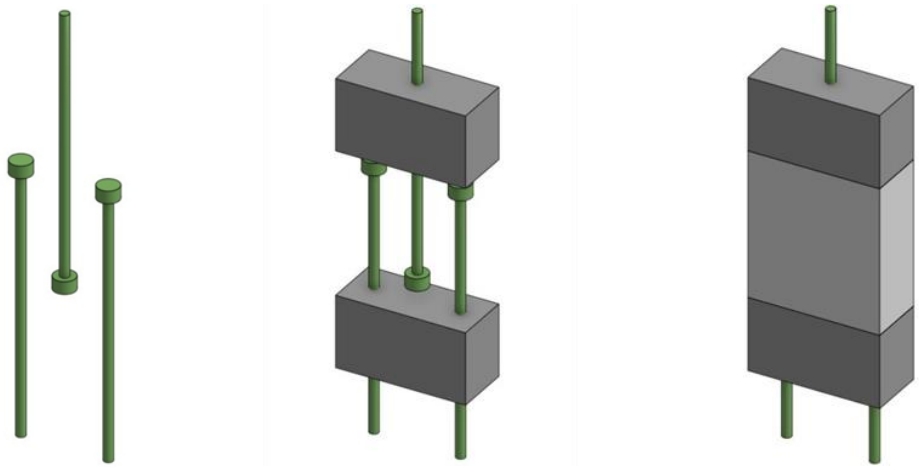

(a) Rebars **(b) Precast concrete segments cast** **(c) Closure pour concrete cast**

Figure 15. Headed bar pull-out specimen fabrication sequence.

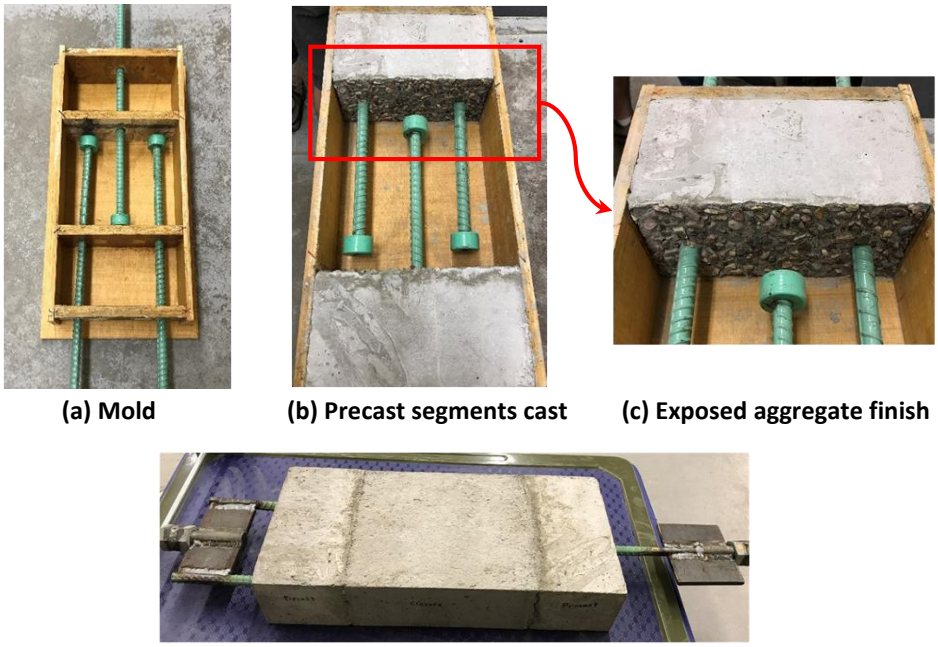

(a) Mold **(b) Precast segments cast** **(c) Exposed aggregate finish**

(d) Fully cast specimen

Figure 16. Headed bar pull-out specimen fabrication.

Flexural Beam Casting

Large beam samples were used to determine the flexural strength under three-point and four-point bending. Beams were constructed by connecting two separate precast segments with the closure concrete. The overall dimensions of the beam were 78 in. x 12 in. x 8 in. and contained reinforcement as seen in Figure 17. Casting procedure for large beam specimens was similar to headed bar pull-out specimens. Strain gages were installed on rebar before casting concrete and were oriented so that strain gages were facing up and down. The sequence of casting is shown in Figure 18. Rebars were first setup with epoxy coated rebars at the top and headed rebars at the bottom. Next, the precast concrete was poured. The last step was to connect the two precast segments by pouring the closure concrete.

Due to the large volume of precast concrete needed, a mixing truck was used for the larger precast segments. Precast concrete for headed bar pull-out and flexural beam specimens were cast at the same time. The concrete surface retarder was applied to the molds. Rebars were placed inside the molds and set the correct distance. A group of ISU student volunteers helped pour all the specimens within an hour. Figure 19 shows pictures from the "Pour Day" which the volunteers were involved with. After casting the concrete, the rebars were checked to ensure they were correctly positioned. Eye bolts were embedded in samples to be used for lifting. Precast concrete cylinders to be used for material property tests were cast at the same time. Refer to Appendix M of the thesis by Casanova, M. (2018) for more photos of specimen fabrication.[49]

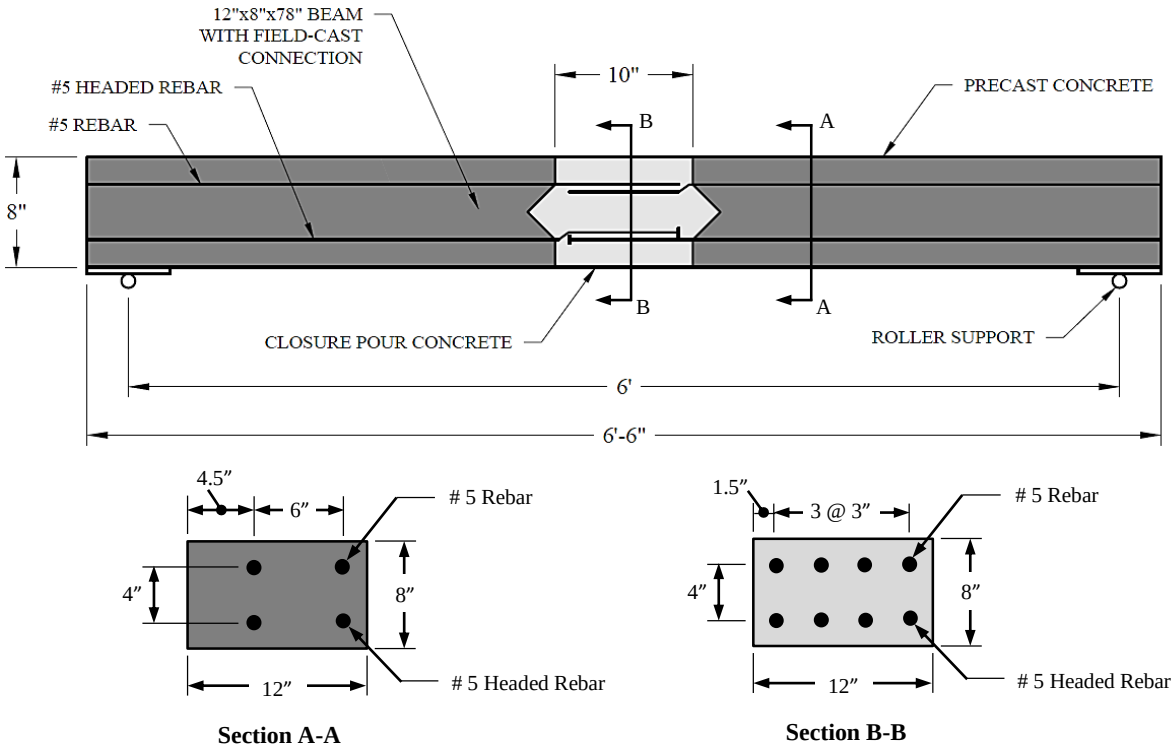

Figure 17. Large beam schematic.

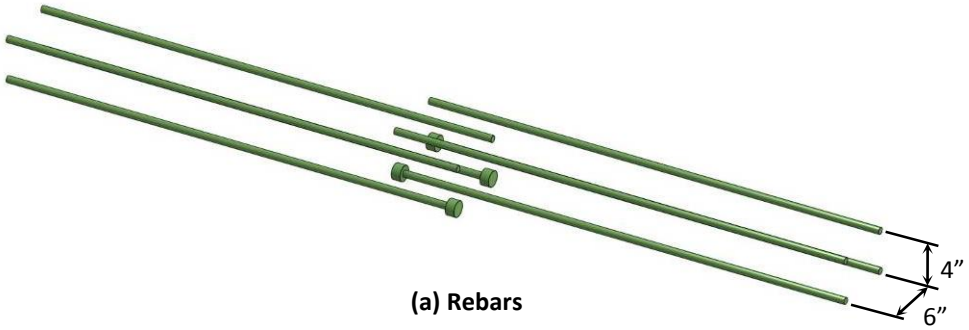

(a) Rebars

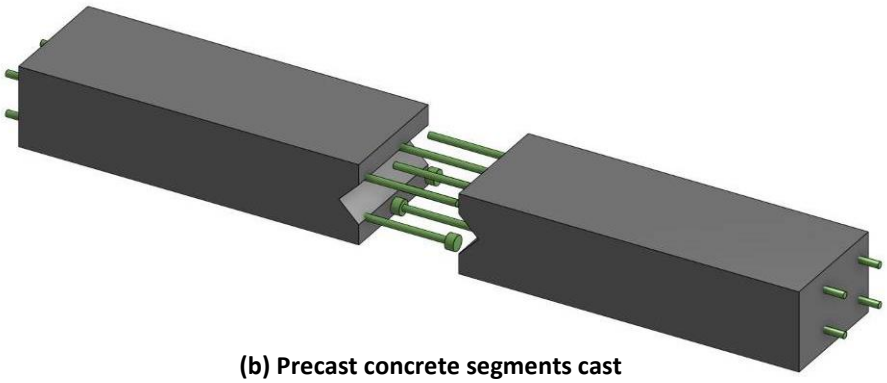

(b) Precast concrete segments cast

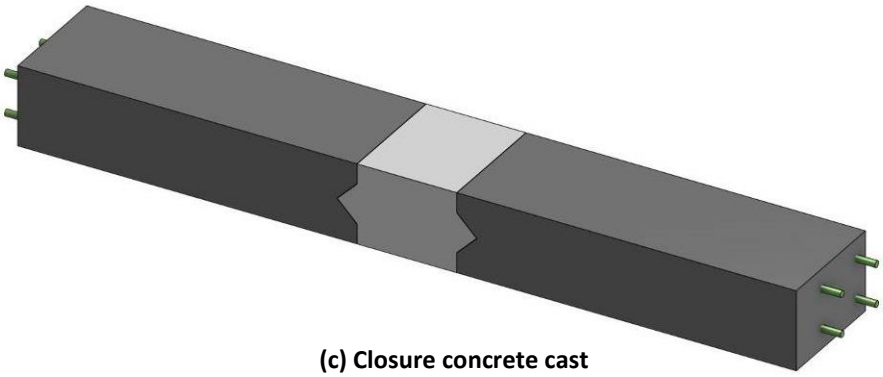

(c) Closure concrete cast

Figure 18. Large beam specimen fabrication sequence.

(a) Pouring large beam precast segments

(b) Pouring rebar pull-out specimen precast segments

(c) Rodding large beam

(d) Embedding eye bolt anchors

Figure 19. Pictures from the "Pour Day" (casting of precast concrete segments).

Testing

This section presents the various tests that were carried out as part of the experimental work for this project. These tests include concrete compressive strength, splitting tensile, length change, modulus of elasticity, and Poisson's ratio which were used to determine concrete material properties. Additional tests include interface bond, headed bar pull-out, and flexural beam. These tests are described in the following sections.

Compression Test

Concrete compressive strength tests were conducted according to ASTM C39, *Standard Test Method for Compressive Strength of Cylindrical Concrete Specimens*.[56] Specimens were capped according to ASTM C617 with a sulfur based compound to provide uniform load distribution.[55] Cylinders were used to determine the 1-day and the 28-day compressive strengths. Compression tests were conducted using the Gilson Compression Testing Machine shown in Figure 20(a). A loading rate of approximately 440

lb/sec was applied until failure. The peak load was recorded from the digital readout of the machine. Figure 20(b) shows a compressive specimen prior to testing.

(a) Gilson testing machnie **(b) Compression specimen**

Figure 20. Compression testing setup.

Splitting Tensile Test

Splitting tensile strength tests followed ASTM C496, *Standard Test Method for Splitting Tensile Strength of Cylindrical Concrete Specimens*.[16] Either 4 in. x 8 in. or 6 in. x 12 in. concrete cylinders are used for this test. Wood strips were used to provide uniform loading along the length of the cylinder. A loading rate of approximately 126 lb/sec was applied until failure. In this project 4 in. x 8 in. cylinders were used as shown in Figure 21.

Figure 21. Splitting tensile testing setup.

Length Change Test

Length change testing followed ASTM C157, *Standard Test Method for Length Change of Hardened Hydraulic-Cement Mortar and Concrete*.[9] This test method uses 3 in. x 3 in. x 11.25 in. concrete prisms with gage studs embedded at the ends to measure changes in length over time. An initial measurement was taken after removing samples from the molds 24 hours after casting. Samples were then moist cured. At 28 days, samples were removed and another measurement was taken. Samples were then placed on a rack at least one inch apart to allow for uniform drying as shown in Figure 22. Specimens continued to dry during which time measurements were periodically recorded. Measurements were taken after curing at 4, 7, 14, 28, 42, and 56 days, and then every 4 weeks for a total of 336 days following curing. A comparator, shown in Figure 23, was used to measure the difference in length between the reference bar and the specimen. A reference bar is first placed in the comparator and the digital indicator is zeroed. A specimen is then placed into the comparator and the measurement is recorded. The change in length is then calculated according to the ASTM procedure.

Figure 22. Shrinkage specimens air drying.

(a) Length comparator

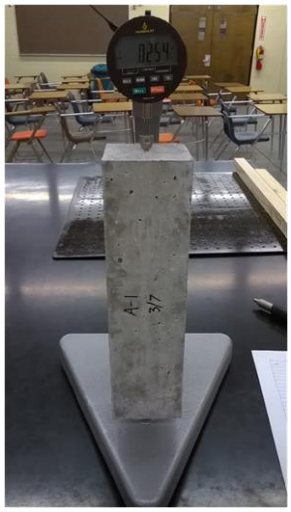

(b) Measuring sample

Figure 23. Length change test.

Modulus of Elasticity and Poisson's Ratio Tests

Modulus of elasticity and Poisson's ratio tests were conducted on cylinders that were made while casting the precast and closure concretes for the headed bar pull-out and large beam specimens. Prior to conducting compressive strength tests, concrete cylinders were first used to determine modulus of elasticity and Poisson's ratio according to ASTM C469.[57] This test uses a compressometer/extensometer shown in Figure 24(a) to measure strain of a concrete specimen subjected to compression loading. The device in use is shown in Figure 24(b). Refer to Appendix K of the thesis by Casanova, M. (2018) for the detailed testing procedure.[49]

(a) **(b)**

Figure 24. Compressometer/extensometer.

Interface Bond Test

Similar bond tests performed by De la Varga et al. (2016) and Haber and Graybeal (2016) were used for this study because this test best replicates the stresses at the interface in the field.[1, 6] Interface bond samples were tested in third-point loading in accordance with ASTM C78. Figure 25 shows the Gilson Testing Machine and flexural beam testing apparatus that were used to break the samples. A constant loading rate of 30 lb/sec was applied until beam failure occurred. After testing concluded, the maximum load was recorded and cross-sectional measurements were taken to calculate bond strength.

Headed Bar Pull-out Test

Samples were tested in tension using the United Testing Machine shown in Figure 26. Monitors were setup next to the test specimen so that a high resolution camera could view the specimen and the measured values. Specimens were loaded at a constant rate of 0.01 in./min until failure occurred. Load, displacement, and strain values were recorded with each test. Six headed bar pull-out tests were conducted. The instrumentation used for this test will be discussed in Chapter 4.

Figure 25. Interface bond test setup.

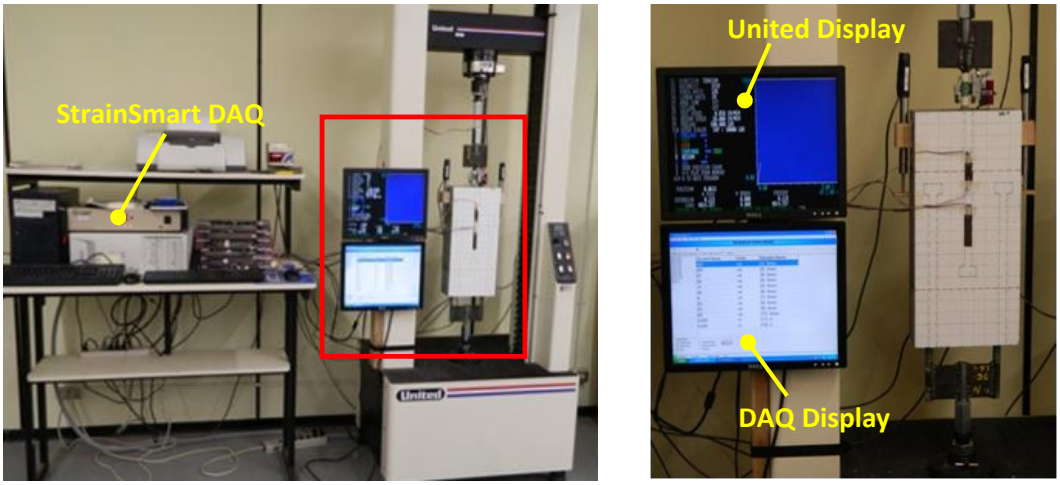

(a) Test setup **(b) Sample**

Figure 26. Headed bar pull-out test setup.

Flexural Beam Test

A total of six beams were cast. Three beams were tested in three-point bending and three were tested in four-point bending. Beams were tested in the Tinius Olsen Testing Machine shown in Figure 27. In these tests the closure pour concrete age was 28 days. The span length for all beams was 72 inches.

Figure 27 shows the diagram of the flexural beam test setup. Before loading the connecting bolts for the steel beam to the steel column supports were removed. The Tinius Olsen contains a hydraulic pump underneath the loading platform so when the pump is activated, the loading platform is lifted up toward

the upper plate. This means the steel beam is unsupported at the ends and is only supported by the loading platform.

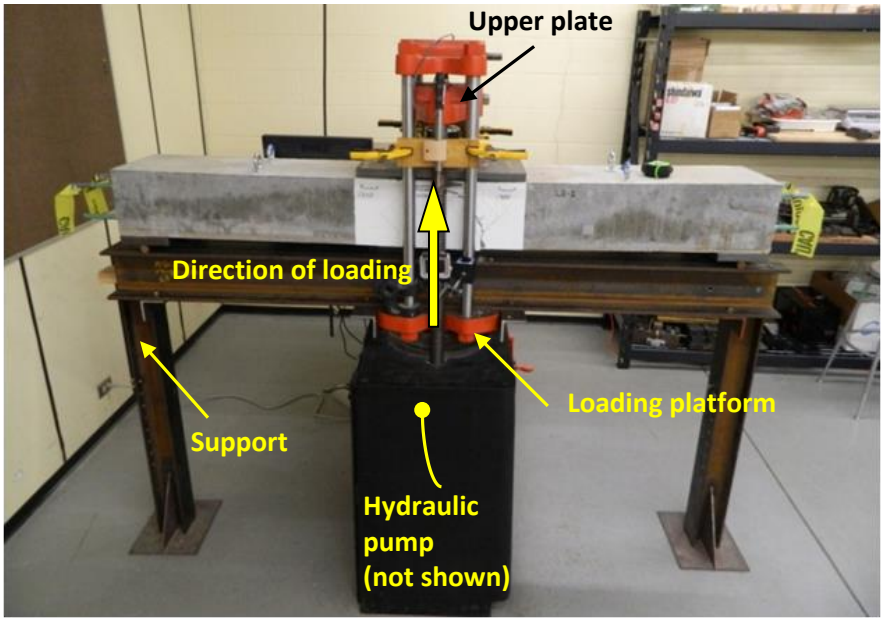

Figure 27. Beam test setup. Note before the test, the supports are removed.

Three-point flexural testing consisted of applying the load to a one-inch thick plate at the center of the beam. The plate was 10 in. x 20 in., which simulates a truck tire footprint as prescribed by American Association of State Highway and Transportation Officials (AASHTO). Figure 28 shows the setup for three-point load testing. The steel plate, load cell, and rubber pad were setup as shown in Figure 29.

Four-point loading in Figure 30 shows a spreader beam (HSS 8 x 4 x 3/8) distributing the load. The load cell setup for four-point bending is seen in Figure 31. Loading for all beam tests were applied at a rate of 0.1 in./min until failure. Instrumentation of the beam specimens will be discussed in Chapter 4.

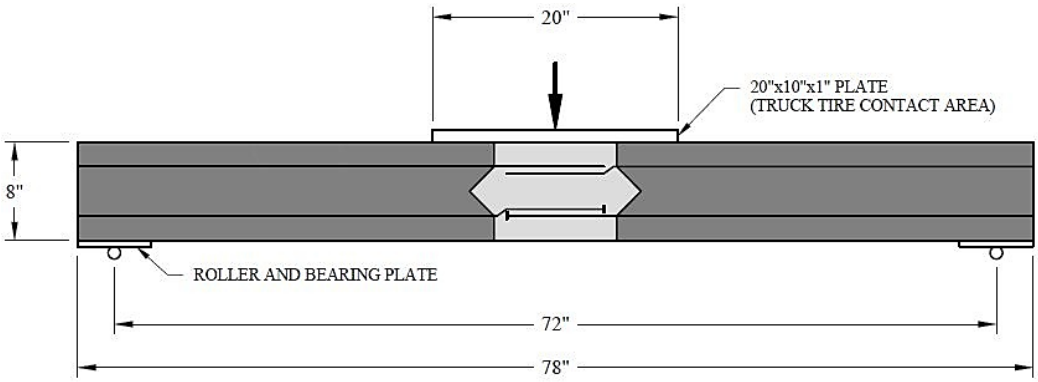

Figure 28. Three-point flexural test diagram.

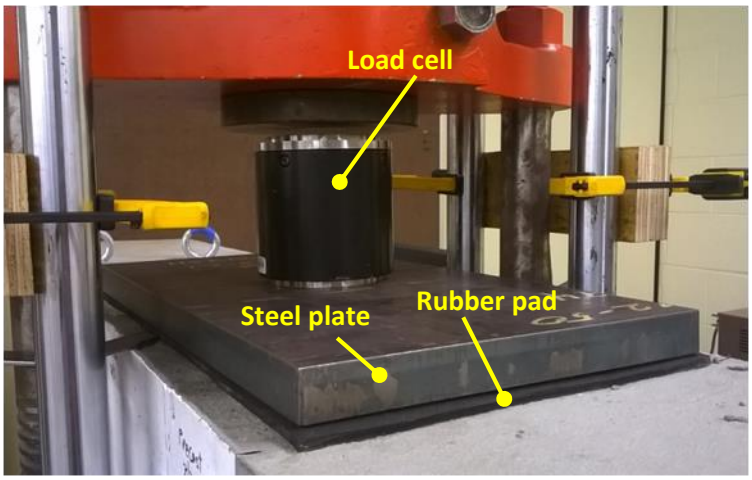

Figure 29. Three-point loading setup.

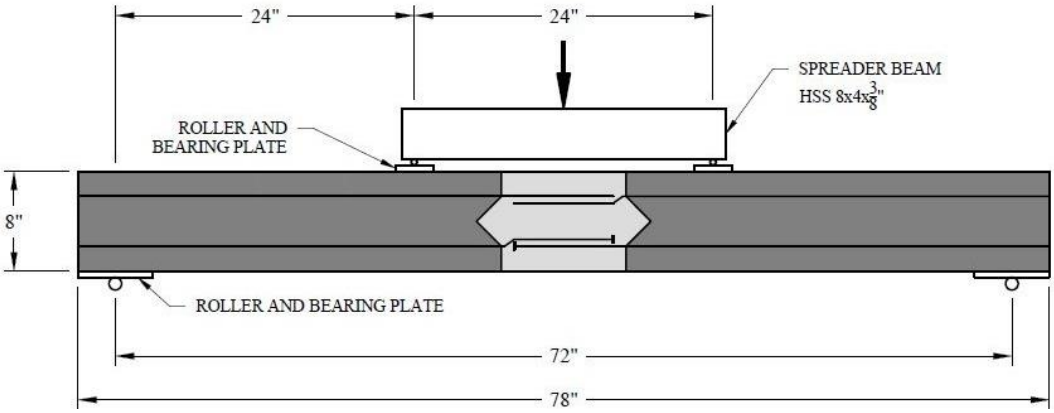

Figure 30. Four-point flexural test diagram.

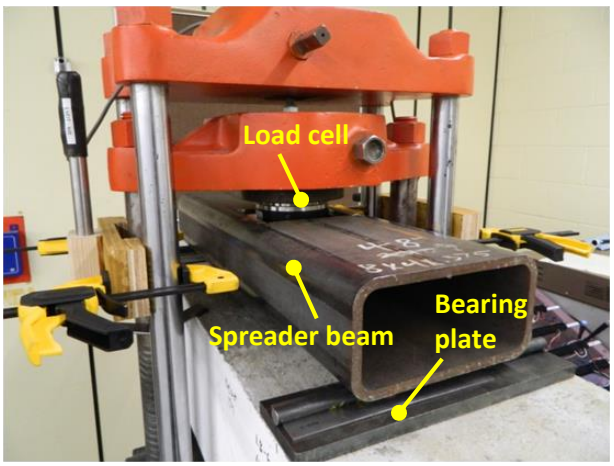

Figure 31. Four-point loading setup.

Instrumentation

The following section describes the instrumentation used to measure larger specimen behavior during testing. Instrumentation used section strain gages, linear variable differential transformers (LVDT), and load cells. Test data was collected using a Vishay Strain Smart Data Acquisition System. The data acquisition system (DAQ) uses cards for different measuring devices. This project utilized strain gage cards and LVDT cards. More on instrumentation used in this project are provided in thesis by Casanova, M. (2018) and its Appendix L.[49]

Strain Gages

The installation of rebar strain gages followed manufacturer procedures for steel installation as outlined in Micro-Measurements *Instruction Bulletin B-137*, strain gage installation for metallic structures. Concrete strain gages were also used for this project. The installation for concrete strain gages followed procedure as outlined in Micro-Measurements *Tech Tip TT-611*, strain gage installation for concrete structures. Figure 32 shows the steel and concrete strain gage installation.

(a) Headed bar strain gage installation

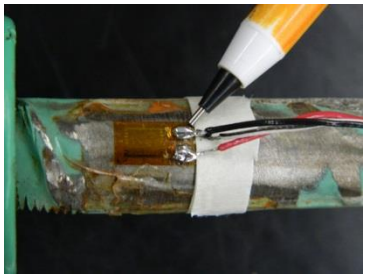

(b) Strain gage next to steel bar's head

(c) Steel strain gage on headed bar pull-out specimen

(d) Concrete strain gages on headed bar pull-out specimens

(e) Gages in protective coating and wrapped in aluminum foil

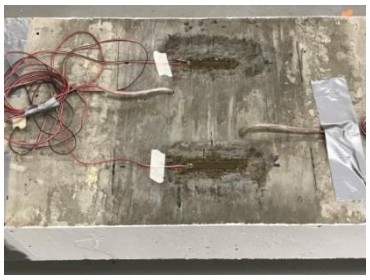

(f) Concrete strain gages on bottom of a beam specimen

Figure 32. Headed steel bar and concrete strain gage installation.

Linear Variable Differential Transformer (LVDT)

Displacements were measured using a linear variable differential transformer or LVDT shown in Figure 33(a). Mounting blocks for the LVDTs were fabricated using 2 in. x 3 in. lumber to securely hold LVDTs in

place. A hole was drilled through the block and a slit was cut along the side as shown in Figure 33(b). A screw was used to clamp the LVDT to the block. No slipping occurred once the LVDT was clamped.

(a) LVDT

(a) Mounting block

Figure 33. LVDT and mounting block.

Load Cells

Load cells were used to measure the applied force subjected to the specimens. Two load cells were needed; one for tension and another for compression. A tensile load cell was fabricated to be incorporated into the pull-out tests. The compression load cell was used for the large beam tests. Figure 34 shows the load cells used this project. More details on load the cells and the calibration process are provided in the thesis by Casanova, M. (2018).[49]

(a) Tension load cell used in headed bar pull-out tests

(b) Compression load cell used for beam tests

Figure 34. Tension and compression load cells

Specimen Instrumentation

Data collected from pull-out tests included strain, displacement, and force. Strain gages were included on the center rebar. Concrete strain gages were placed at three locations: in the middle of the closure concrete and on either side of the top interface. Gages were installed on the front and back of the

samples. A pair of strain gages was installed at each location on the concrete and on the headed bar, on opposite sides, to remove any local bending effects when measuring the axial strain. The concrete strain gages were all surface mounted. The larger concrete strain gages give the average strain over a 2-inch gage length. Figures 35 and 36 show the pull-out specimen and the locations of the strain gages. As shown in Figure 36, LVDTs were attached to the left and right side to measure the expansion of the interface crack. Mounting blocks were attached to the samples using a two-part epoxy. Supports made from L-brackets were also attached to the sample for the extension rods as seen in Figure 32(b). Threaded couplers were used to attach the ends of the pull-out specimen and tensile load cell to the United Testing Machine.

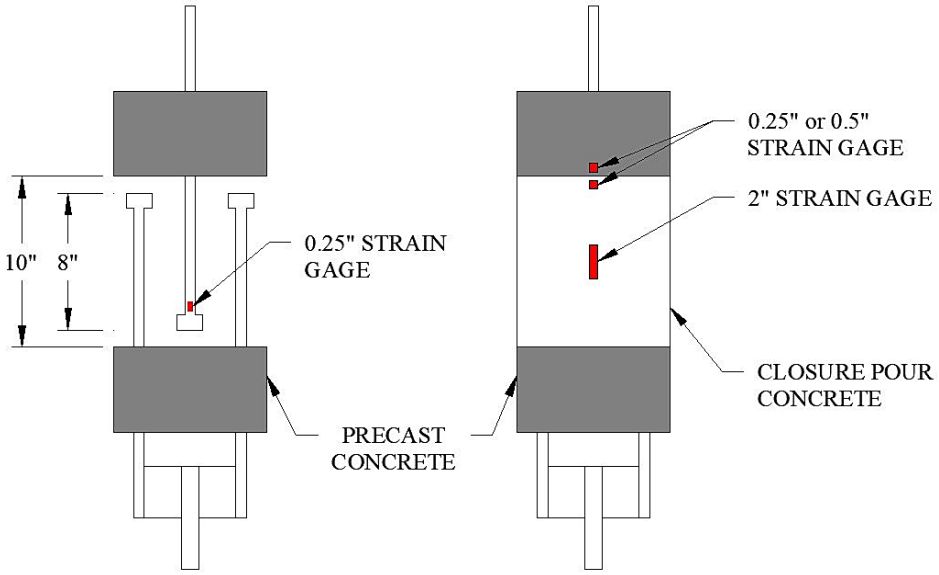

Figure 35. Pull-out Sample Instrumentation.

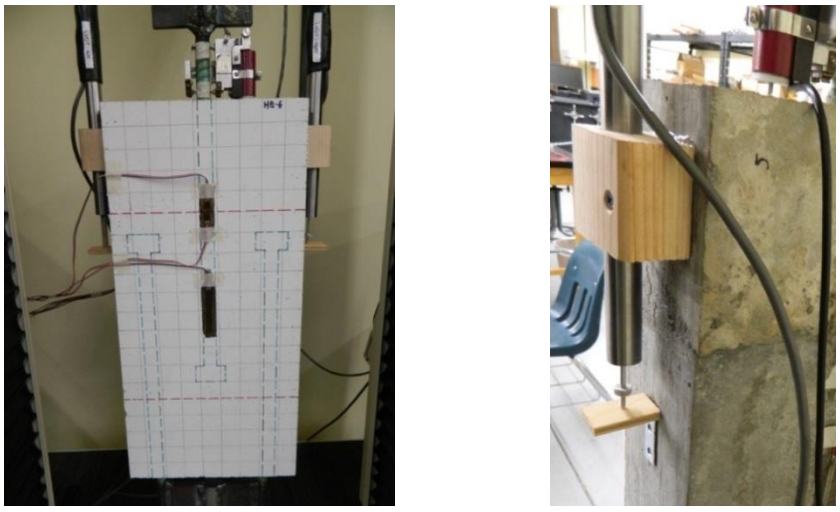

(a) **(b)**

Figure 36. (a) Pull-out specimen and (b) LVDT setup.

Beam tests used similar instrumentation. Two strain gages were attached to each of the two central headed rebars. Two strain gages were also attached to the bottom face of the closure concrete section. Figure 37(a) shows the locations of all six strain gages on the beams. LVDTs were used to measure the mid-span deflection of the beam. The LVDT wood mounting blocks were attached to a piece of plywood that was clamped to the frame of the Tinius Olsen machine, as shown in Figure 37(b). Steel plates were attached to the top of the beam in the center which extended to the outside of the frame.

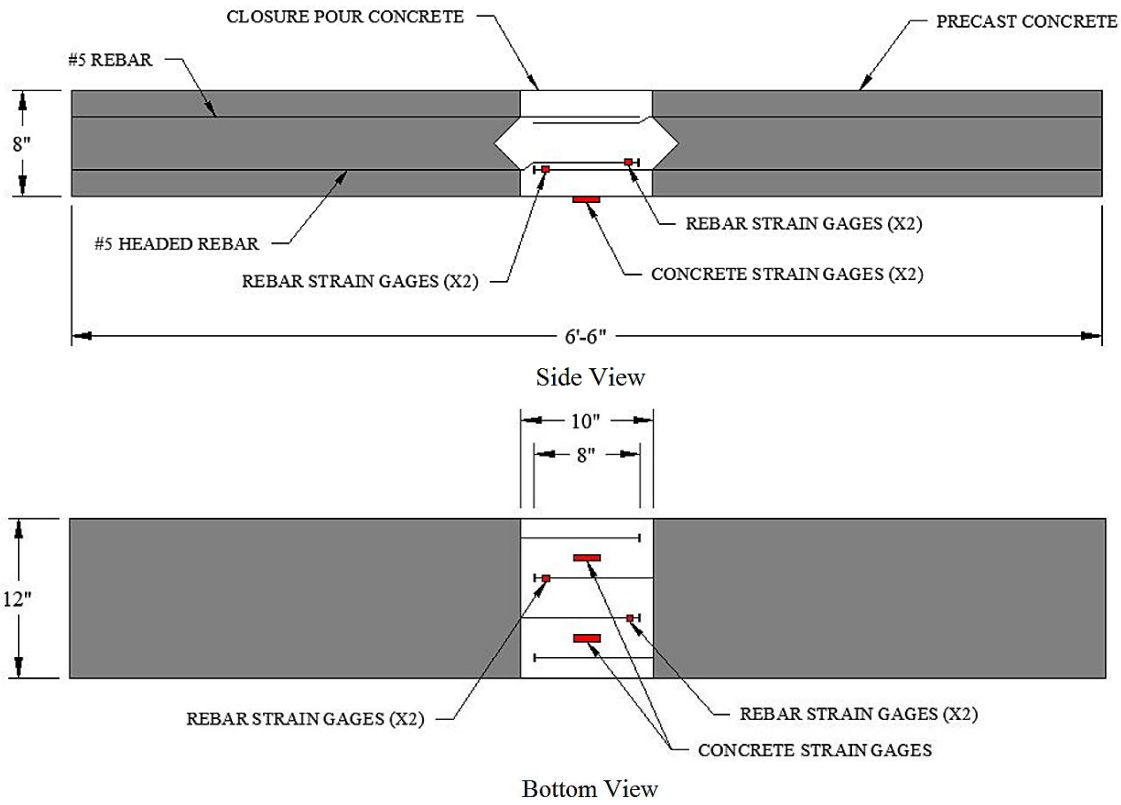

(a) Strain gage locations

(b) LVDT mount and extension bracket

Figure 37. Large beam instrumentation.

Data Analysis

The following section describes how the test data was processed using the Strain Smart software and the System 6000 DAQ. After importing the data into Excel, the data was analyzed. Results were produced from this Excel data analysis. The results are presented in Chapter 4.

Strain Smart

The Strain Smart software can have a scan rate ranging from 100-10,000 samples per second. The sample rate is the number of measurements that will be collected per second. The System 6000 is designed for dynamic measurements and use higher sampling rates. Loading procedures for this project only considered static loading conditions. Therefore, the sample rate was kept low. Using a slower setting decreases the file size. The sample rate applies to each channel, meaning each channel with a measuring device will be sampled at the same rate.

Headed bar pull-out tests took approximately 2.5 minutes and large beam tests took approximately 5 minutes to complete. Headed bar tests had a total of 12 channels and beam tests had 9 channels. Table 6 shows the number of instrumentation channels used for each test.

Table 6. Instrumentation channels used for larger specimen tests.

Sensor Type		Headed Bar Pull-out	Large Beam
Strain gages	Load cell	2	1
	Rebar	2	4
	Concrete	6	2
LVDT		2	2
	Total	**12**	**9**

Over 30,000 data points were collected for each channel for the headed bar pull-out tests and 60,000 data points for beam tests. Data was exported to an Excel file for processing. Precision of load and strain data was measured to the nearest microstrain (i.e. 1×10^{-6}) and displacements were measured to the nearest thousandths of an inch.

To simplify analysis, the data was reduced in the post-processing phase. A trial and error approach showed that taking data points at every ¼ second was sufficient for the experimental tests in this project. Reduction in data did not affect outputs, i.e., the maximum or minimum values. After the data reduction, headed bar pull-out and beam tests had approximately 600 and 1,200 data points for each channel, respectively.

Calculating the Headed Bar Stress Next to the Head and Force Taken by the Head

As shown in Figure 38, strain gages were placed next to the head of the headed bars for the upper bar in the pull-out specimens and the two bottom headed bars in the beam specimens. The center of the steel bar strain gages was 1 in. away from the head. Therefore, the stress at these locations or the estimated force taken by the head can be determined.

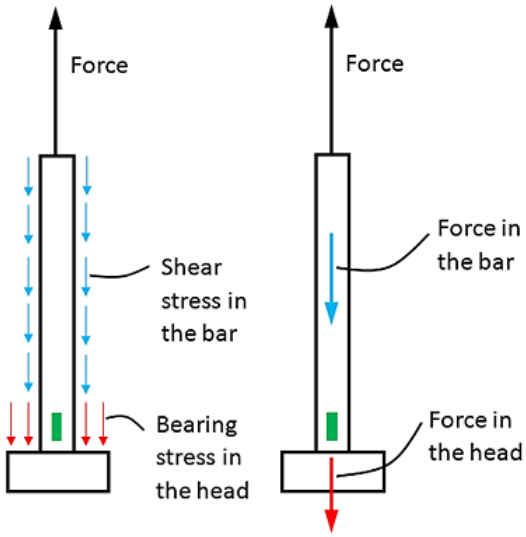

Figure 38. Bar stress from strain gages and force in the head of the headed bar.

The bar stress and force resisted by the head of the headed bar was calculated using the equation in Figure 39.

$$\sigma_{bar} = E_s \, \varepsilon_{avg.}$$

$$F_{head} = \sigma_{bar} \, A_{bar} = E_s \, \varepsilon_{avg.} \, A_{bar}$$

Figure 39. Equations for calculating stress in the bar next to the head and force in the head.

Where,

E_{steel} = Modulus of elasticity, modulus of steel = 29 x10^6 (psi),
σ_{bar} = Normal stress in the bar next to the head (psi),
$\varepsilon_{avg.}$ = Average strain of the two strain gages next to the head (με, 10^{-6}),
F_{head} = Estimated force in the head (lb),
A_{bar} = Bar cross-sectional area (in.^{2}).

Calculating the Concrete Beam Mid-span Deflection

As shown in Figure 27, before loading the beam, the connecting bolts for the steel beam-to-column supports were removed. The Tinius Olsen contains a hydraulic pump underneath the loading platform so

when the pump is activated the platform is lifted up into the upper plate. This means the steel beam is unsupported at the ends and it is only supported by the loading platform. LVDT measurements were adjusted to account for bending of the steel support beams. Concrete beam and steel beam deflections are shown in Figure 40.

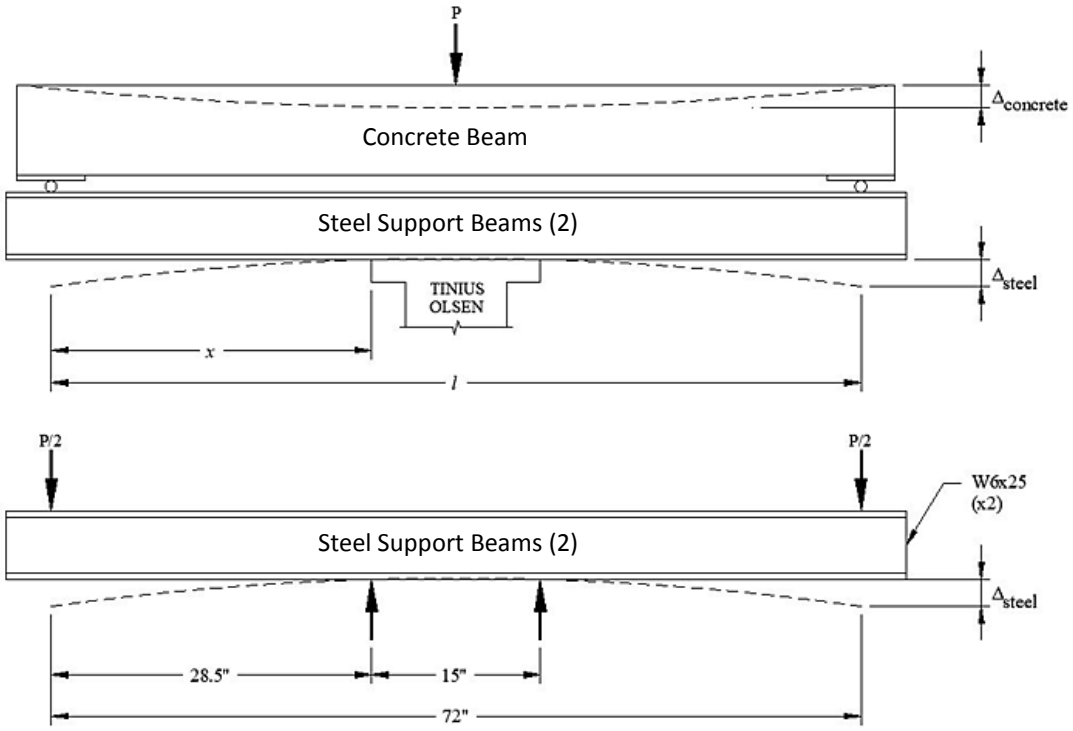

Figure 40. Beam deflection diagram.

The measured displacement from the LVDTs is the summation of the deflection of the concrete beam and the deflection of the two identical support steel beams. This is expressed as:

$$\Delta_{measured} = \Delta_{concrete} + \Delta_{steel}$$

Or,

$$\Delta_{concrete} = \Delta_{measured} - \Delta_{steel}$$

Figure 41. Equations for calculating concrete beam mid-span deflection.

Where,

$\Delta_{concrete}$= Mid-span concrete beam deflection (in.),
$\Delta_{measured}$ = Displacement measured from LVDT (in.),
Δ_{steel} = Deflection of the steel support beams (in.).

The loading condition of the steel support beams in Figure 40 is a simply-supported beam with two equal concentrated loads symmetrically placed. From the deflection diagrams in Table 3-23 of the AISC Steel Construction Manual the deflection equation was obtained for the corresponding load case.[58] The deflection in the steel support was very small in comparison to the concrete beam. More details of calculating the concrete beam mid-span deflection are presented in thesis by Casanova, M. (2018).[49]

Chapter 4
Experimental Results

Introduction

This chapter presents the results obtained from laboratory tests. It is divided into six sections: compression strength, splitting tensile strength, shrinkage, interface bond strength, headed bar pull-out test results, and flexural beam test results. Based on the results obtained from the tests conducted on the material properties, namely compression, split tensile, and shrinkage, an optimum mix was determined. Using this optimum mix and another alternative mix (as suggested by ITD), interface bond strength tests were performed. This resulted in the best method for preparing the interface between the precast concrete and closure pour material. The headed bar pull-out test and the flexural beam test determined the behavior of the ITD connection detail with the optimum closure pour material.

Compression Results

In order to obtain the compressive strength of a sample, the cross-sectional area was first determined. Two diameter measurements were taken perpendicular to each other at mid-height of the specimen. After the samples were measured, they were tested according to the methodology in Chapter 3. Following testing, the peak load was recorded and used to calculate the compressive strength using the equation in Figure 42.

$$f_c' = \frac{P}{A}$$

Figure 42. Compressive strength of concrete.

Where,

f_c' = Compressive strength (psi),
P = Peak load (lb),
A = Cross sectional area (in^2).

Standard deviation and coefficient of variation were also calculated for 28-day compressive strengths for each set. Results are shown in Table 7. Figure 43 is a graphical representation of the data provided in Table 7.

The 1-day compressive strength was a design criterion with a minimum value of 3,000 psi, as specified by ITD. Mixes E and F were below the minimum at 2,550 psi and 2,723 psi, respectively. As seen in Table 7, the highest 28-day compressive strength attained was 8,864 psi for Mix D. The coefficient of variation for all mix designs were within the 3-7% range. The error bars in Figure 43 represent the standard deviation of the mixes considered. The compression result data for all specimens tested are presented in Appendix D of the thesis by Casanova, M. (2018).[49]

Table 7. Compressive strength of closure pour concrete mixes.

Mix	1-day compressive strength (psi)	28-day compressive strength (psi)	Standard deviation, 28-day (psi)	Coefficient of variation, 28-day (%)
A (control)	3,196	7,752	374	4.8
B	3,442	8,471	281	3.3
C	3,551	7,860	332	4.2
D	3,074	8,864	623	7.0
E	2,550	7,710	260	3.4
F	2,723	8,161	385	4.7

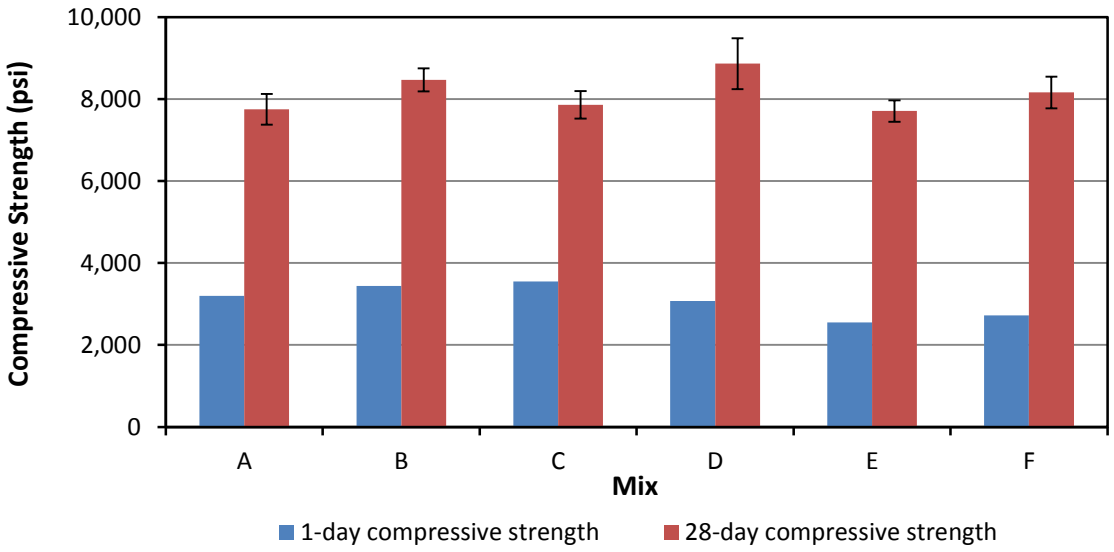

Figure 43. Compressive strength of closure pour concrete mixes.

Tensile Strength Results

Using a straight-edge, a line was first drawn along the length of the sample. Utilizing a combination square, a second line was then drawn across the end connecting it with the first line. Three diameter and two length measurements were taken. After the specimens were measured, they were tested according to the procedure outlined in Chapter 3. The peak load was recorded and the splitting tensile strength was calculated using the equation in Figure 44.

$$T = \frac{2P}{\pi LD}$$

Figure 44. Tensile strength formula.

Where,

T = Splitting tensile strength (psi),

P = Peak load (lb),
L = Average length (in.),
D = Average diameter (in.).

Figure 45 shows a typical split cylinder test before and after failure. Standard deviation and coefficient of variation were also calculated for each set. The results are shown in Table 8 and Figure 46.

During the progression of the test, a crack develops along the vertical plane of the cylinder. Mixes without fibers exhibited sudden failures, whereas mixes containing fibers had more ductility. This was a result of the fibers holding the concrete together which is shown in a close-up view in Figure 47 where fibers can be seen in the crack.

As seen in Table 8 the highest splitting tensile strength was 837 psi for Mix D. The addition of polypropylene fibers for Mixes B and C showed a decrease in strength compared to the control (Mix A) of 133 psi and 34 psi, respectively. All mix designs' coefficient of variation fell in the 3-10% range. The splitting tensile strength data of all mixes are presented in Appendix E of thesis by Casanova, M. (2018).[49]

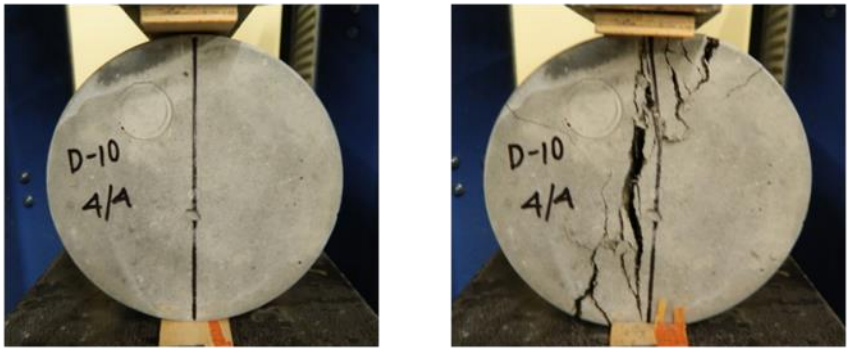

(a) Before Test **(b) After Failure**

Figure 45. Specimen in splitting tensile test.

Table 8. Splitting tensile strength results.

Mix	Average split tensile strength (psi)	Standard Deviation (psi)	Coefficient of variation (%)
A	767	31	4.0
B	634	64	10.1
C	733	45	6.2
D	837	54	6.5
E	749	36	4.9
F	765	27	3.5

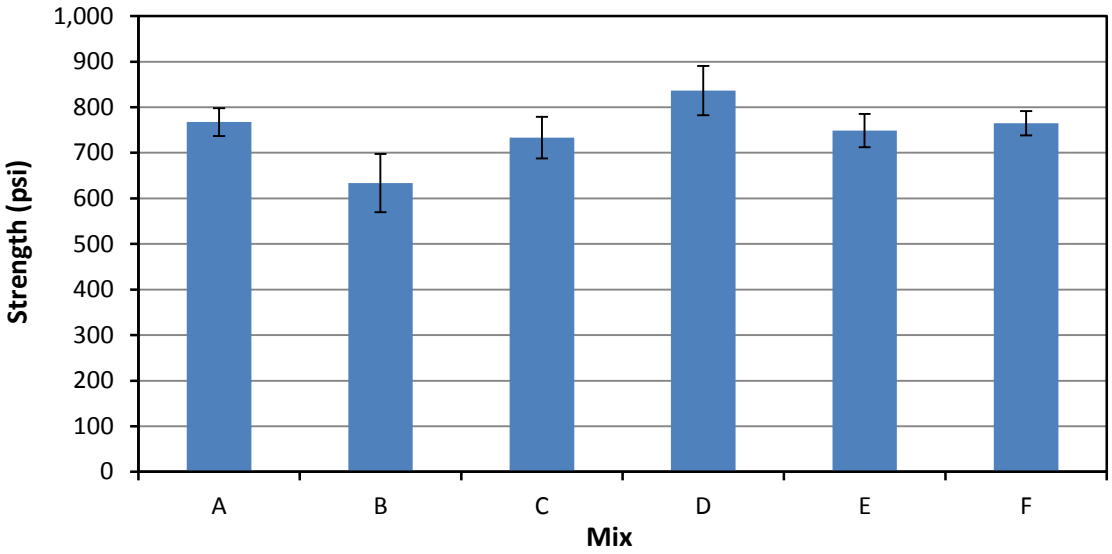

Figure 46. Splitting tensile strength results.

Figure 47. Split tensile crack showing the fibers.

Length Change Results

Length change measurements followed the procedure outlined in Chapter 3, Length Change Test section. For each mix, there were six samples. An initial length measurement, CRD_{inital}, was taken after removal from the mold at 24 hours. This was the baseline for determining changes in length according to equation in Figure 48.

$$\Delta L_x = \frac{CRD - CRD_{inital}}{G}$$

Figure 48. Equation for length change measurements.

Where,

ΔL_x = Length change of specimen (με),

CRD = Difference between the comparator reading of the specimen and the reference bar reading (in.),

G = Gage length = 10 in.

Negative length change values indicate shrinkage and positive values represent swelling. Samples were stored on a metal rack spaced at least one inch apart in accordance with ASTM C157 for air storage.[9] Average shrinkage curves are shown in Figure 49. Average values for mix design "A" excluded specimen A-4 since in that specimen one of the gage studs was set too far into the concrete and readings were not possible. All specimens exhibited swelling, an increase in volume, during moist curing caused by the absorption of water. This swelling is shown on the shrinkage graphs indicated by the positive values at zero days. Once the specimens were removed from water they began to shrink caused by the loss of water. The majority of the samples follow a steady curve but there were some fluctuations either increasing or decreasing abruptly, but these variations were acceptable. Data were collected up to 336 days after removal from moist curing.

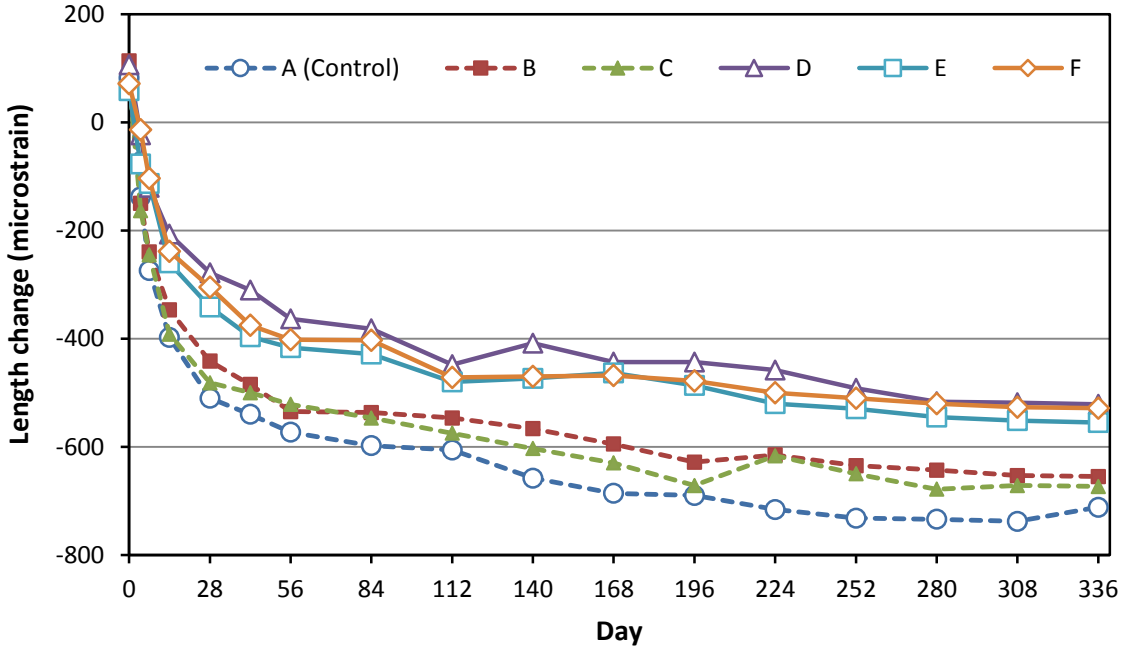

Figure 49. Average length change after removal from mold at 24 hours.

The shrinkage curves follow similar trends with the majority of shrinkage, about 70-80% of the long-term shrinkage, occurring in the first two months. For this study the long-term drying shrinkage is considered to be the length change at 336 days. Long-term shrinkage values for each mix are shown in Table 9. As shown in Table 9, the lowest shrinkage value was 522 microstrain for Mix D, a 29% reduction from the control. Addition of fibers decreased shrinkage, as seen with Mixes B and C. Use of shrinkage reducing admixture (SRA) had a significant effect on decreasing shrinkage. The average shrinkage for mixes containing SRA (i.e. Mix D, E, and F) is 535 microstrain compared to the average shrinkage for mixes only containing fibers (i.e. Mixes B and C) at 664 microstrain. The difference between Mixes B and C was not significant, this is most likely due to the low range of fiber dosages of 0.75 lb/yd^3 and1.5 lb/yd^3

(0.05% and 0.1% by volume), respectively. The length change data and graphs for all mixes are given in Appendix F of the thesis by Casanova, M. (2018).[49]

Table 9. Long term drying shrinkage.

Sample	Shrinkage (microstrain)	Percent reduction (%)
A (Control)	736	-
B	655	11
C	673	9
D	522	29
E	555	25
F	528	28

Based on the compression, split tensile, and shrinkage results, the optimum mix was determined to be Mix D, which contained 1.5 lb/yd^3 of fiber and SRA. Shrinkage results between Mix D, E, and F were comparable, but Mix D had higher strength values and better workability.

Interface Bond Results

As described in Chapter 3, Interface Bond Test section, the optimum mix was used to test interface bond strength with precast concrete. As recommended by the ITD Technical Advisory Committee, a set of samples with Mix E, which contained 0.75 lb/yd^3 of fiber, SRA, and BA, was also tested. The benefit of bonding admixture was not determined from the material property tests so the interface bond tests would provide the researchers with an indication of the performance. A bonding agent, Tammsweld, was applied to half of the samples.

Prior to testing, marks were drawn on the top and bottom faces to align the specimen with the supports of the testing apparatus as shown in Figure 51. Samples were tested by turning them on their side to provide flat surfaces for loading. Beams were tested 28 days after casting the closure concrete. The age of the precast concrete was approximately 8 weeks at the time of testing. Once the samples were marked, they were tested following the methodology outlined in Chapter 3, Interface Bond Test. Once the test concluded, the break type and peak load were recorded. Three depth and three width measurements were taken at the plane of failure. Measurements were averaged to calculate bond strength using equation in Figure 50.

$$R = \frac{PL}{bd^2}$$

Figure 50. Equation for calculating modulus of rupture.

Where,

R = Modulus of rupture or bond strength (psi),
P = Maximum load indicated by testing machine (lb),
L = Span length = 18 in.,
b = Average width (in.),
d = Average depth (in.).

(a) Beam specimen

(b) Alignment marks for support and loading locations

Figure 51. Interface bond strength test setup.

All interface beam specimens failed at the interface between the precast concrete and the closure pour concrete. Figure 52 shows the failure at the interface that was typical for all samples. During testing, two distinct failure behaviors were observed. The first was a sudden failure of the beam after the maximum load was attained, this was seen for samples without bonding agent. The second failure type was more ductile with samples reaching their peak load then undergoing more deflection before ultimate failure. Bonding agent caused this behavior. The majority of aggregates debonded while only a small portion of aggregates fractured. Mix D samples without bonding agent had 11% of aggregates fracture and about 7% of aggregates fractured in Mix E samples without bonding agent. There was no significant difference in the percent of aggregates that fractured between a mix prepared without bonding agent and the same mix prepared with bonding agent. Figure 53 shows the failure plane of specimen D-2 (an interface bond specimen with Mix D for closure pour segment and with bonding agent).

Figure 52. Interface bond test sample D-4 without bonding agent.

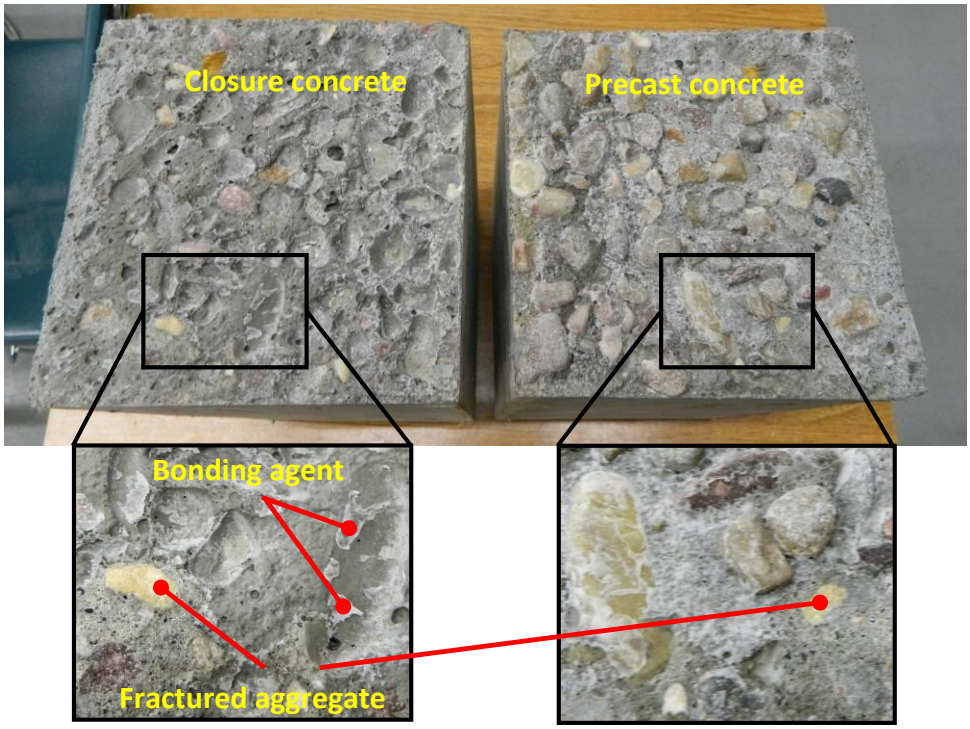

Figure 53. Interface bond failure of specimen D-2 with bonding agent.

The fractured aggregate in Figure 53 was determined by identifying similar aggregates in both failure planes. Residue of bonding agent was seen on both interface surfaces, but the precast interface had more because the bonding agent was applied to the precast portion.

Average bond strength results are shown in Table 10. Standard deviation and coefficient of variation have also been calculated for each set. Figure 54 is a graphical representation of the data provided in Table 10. The error bars in Figure 54 represent the standard deviation of the mixes considered.

Table 10. Interface bond strength summary.

Mix		Average strength (psi)	Standard deviation (psi)	Coefficient of Variation, %	Difference w/ and w/o BG
D	w/o BG	612	78	12.8	
	w/ BG	436	32	7.5	176
E	w/o BG	561	57	10.1	
	w/ BG	386	9	2.2	175

Note: BG = bonding agent.

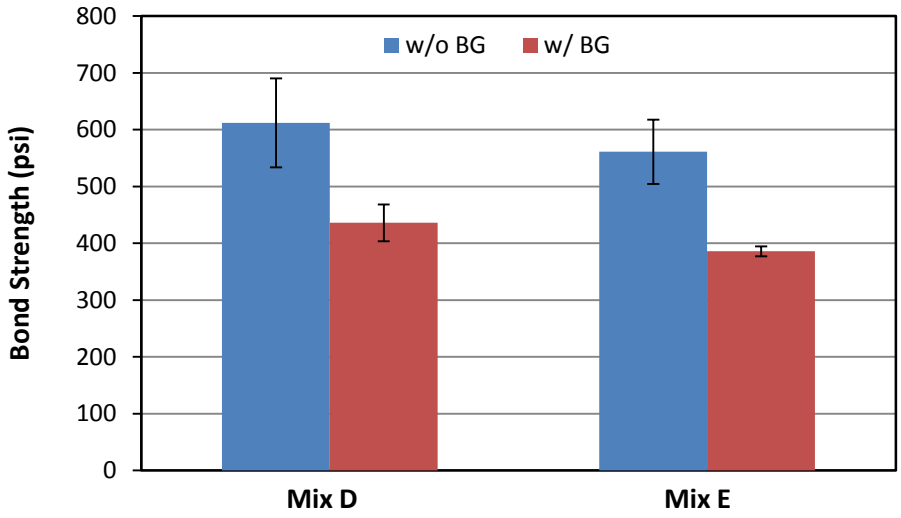

Note: BG = bonding agent.

Figure 54. Average interface bond strength with and without bonding agent.

Bonding agent had an adverse effect on bond strength, resulting in a 29% and 31% reduction in strength for specimens prepared with Mix D and Mix E, respectively. Mix E without bonding agent had a lower strength by 51 psi (8% difference) than Mix D without bonding agent. In addition, Mix D, with no bonding agent, achieved the highest bond strength of 612 psi. Standard deviations differed by approximately 47 psi for mixes with and without bonding agent.

Based on these results, Mix D prepared with a saturated surface dry interface moisture condition, without bonding agent, was selected for use for the remaining headed bar pull-out and flexural beam tests. Pull-out results are discussed in the next section. More details on the interface bond results are given in Appendix H of the thesis by Casanova, M. (2018).[49]

Headed Bar Pull-out Tests

Pull-out specimens were cast and prepared as described in the Chapter 3, section titled Headed Bar Pull-out Specimen Casting. A total of six specimens were tested in tension with the same loading. The headed bar specimens were designated as HB1, HB2, HB3, HB4, HB5, and HB6. Specimens were tested

28 days after casting the closure concrete. Precast concrete age was 74 days at the time of testing. A typical test setup is shown in Figure 55.

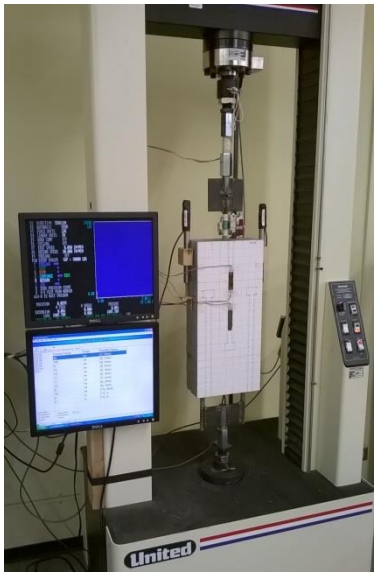

Figure 55. Typical pull-out test setup.

Material Properties

As the precast and closure pour concrete were poured for the headed bar pull-out specimens, a set of test cylinders were also prepared to determine material properties. These material properties are used in the finite element computer modeling part of this project. Material properties for cylinders included: compressive strength, splitting tensile strength, modulus of elasticity, and Poisson's ratio. Concrete material properties are summarized in Table 11. Data for the compressive strength, split tensile strength, modulus of elasticity, and Poisson's ratio can be found in Appendices D, E, and G of the thesis by Casanova, M. (2018).[49]

Table 11. Pull-out tests concrete material properties summary.

	Compressive strength (psi)	Split tensile strength (psi)	Modulus of elasticity (ksi)	Poisson's ratio	Age (days)
Closure	8,453	768	4,322	0.194	28
Precast	5,258	614	3,241	0.170	74

Test Results

Samples were tested as described in Chapter 3. A sample was inserted into the United Testing Machine and instrumentation was connected to the Strain Smart system. Before testing, the instruments were zeroed and the DAQ started recording data. Testing began by loading at a constant rate of 0.01 in./min. Data for headed bar pull-out specimens were collected up to the point of failure. Data past the failure

point was not useful since many of the strain gages broke or were damaged in the process. Figure 56 shows the diagram referencing the labels corresponding to the concrete strain gages. Upper and middle strain gages are located at the top interface. The lower strain gage is located in the center of the closure concrete. Strain gages were applied to the front and the back side of specimens.

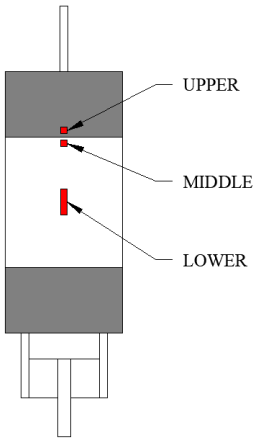

Figure 56. Strain gage labels.

Figure 57 shows a graph of the force versus time for all specimens. The graphs give an overview of the test. The initial portion of the lines, in the boxed area, represents the settlement of the specimen in the machine. The fixtures and connections resulted in slack for the specimen. Tensile testing typically applies a preload but to ensure correct zero values for calibration, this testing procedure did not use a preload. Each line has a distinct initial drop in load which indicates cracking at the top interface. Some specimens had several more drops in load before finally reaching the ultimate capacity. The force drops in Figure 57 are attributed to the cracks within the concrete. All the specimens experienced these drops before reaching the ultimate load.

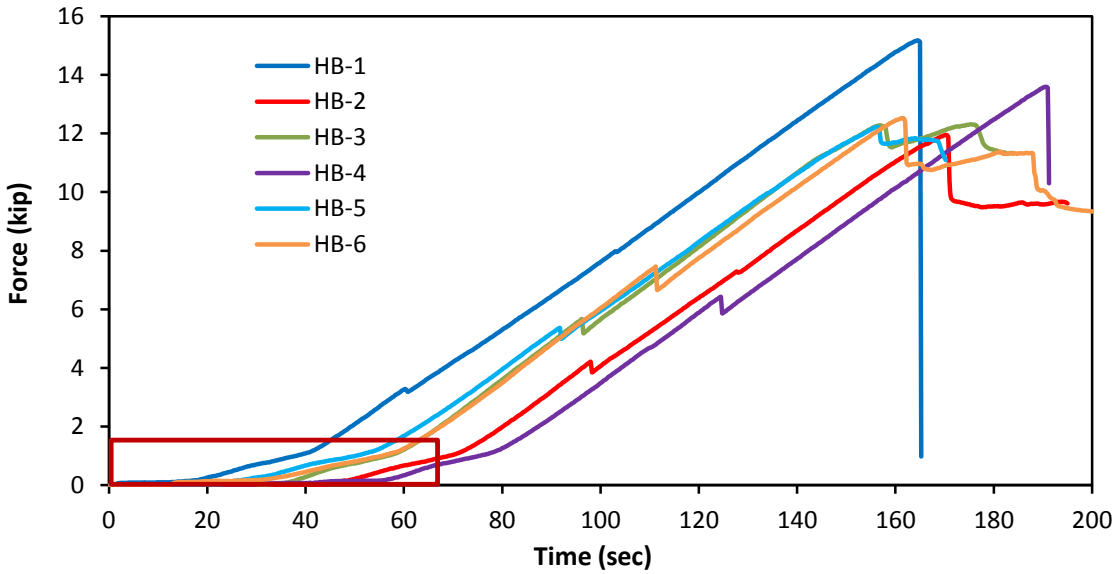

Figure 57. Force vs. time for headed bar pull-out tests.

Cracking initiated at the top interface and propagated horizontally across the sample. The sudden drop between 3,000 lb and 6,000 lb was the point when the top interface cracked. This will be referred to as the cracking force. Load kept increasing and the bottom interface began to show formation of cracks. After reaching the ultimate load, there was a sudden drop in load and the specimen cracked along the center rebar and down into the lower precast concrete section. Conical cracks also developed at the location of the center rebar head. All six specimens showed similar cracking behavior. Figure 58 shows the cracking of all specimens at the end of the tests. No spalling of concrete was observed at any point during the headed bar pull-out tests. Only concrete cracks were observed as shown in Figure 58. More detailed pictures are found in Appendix I of the thesis by Casanova, M. (2018).[49]

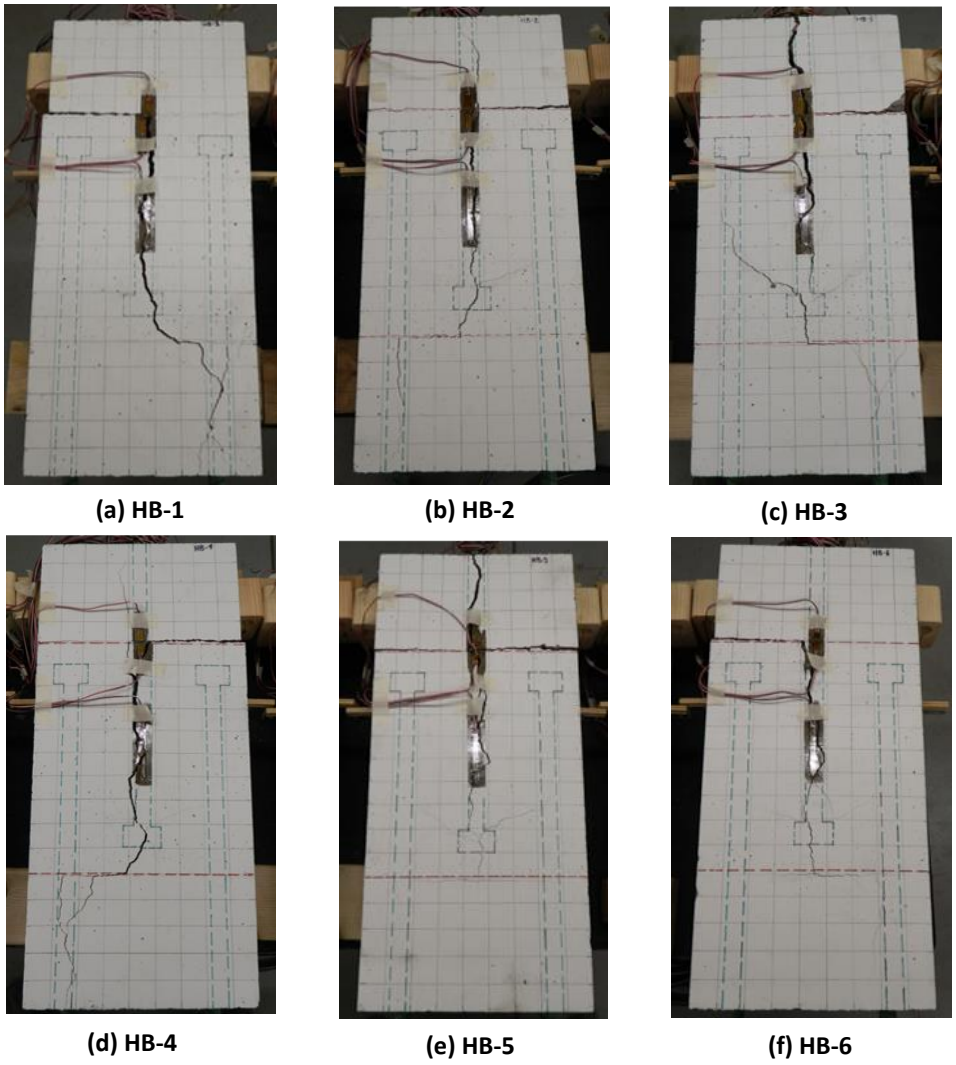

(a) HB-1 **(b) HB-2** **(c) HB-3**

(d) HB-4 **(e) HB-5** **(f) HB-6**

Figure 58. Headed bar pull-out samples crack pattern at the end of the tests.

Figure 59 shows the force versus displacement of the specimens. The figure also shows the points corresponding to cracking and ultimate failure load. Data can be found in Appendix I of the thesis by Casanova, M. (2018).[49]

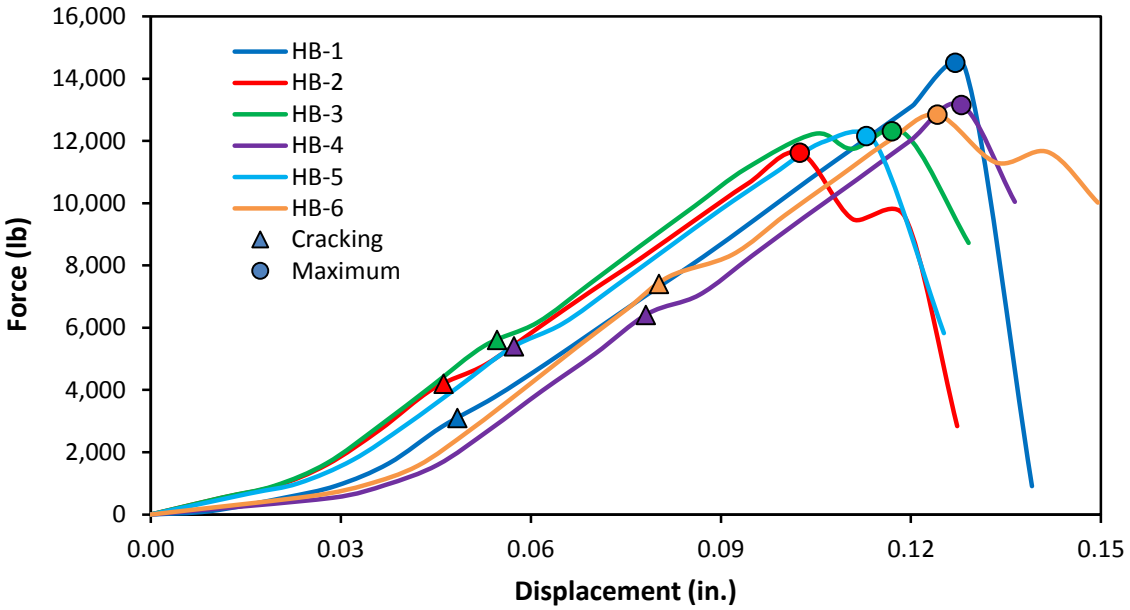

Figure 59. Machine force vs. machine displacement.

The force resisted by the head of the headed bar was calculated using equation in Figure 35 as described in Chapter 3. The applied force from the tensile load cell is graphed against the force in the rebar in Figure 60. Specimens showed similar behavior with the exception of specimen HB-1. The plots show a linear behavior up to the cracking load. The applied load drops slightly then load increases again. After cracking, the behavior becomes nonlinear. The graph also indicates the maximum forces.

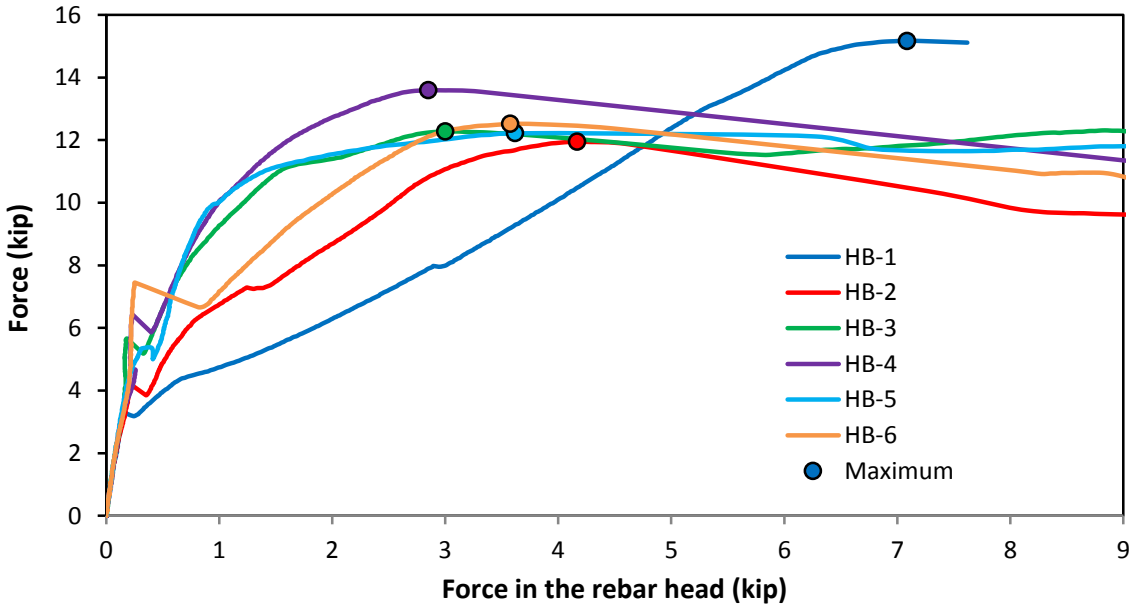

Figure 60. Applied force vs. force in the head of rebar in the pull-out tests.

Figure 61 shows the force versus crack expansion for specimen HB-2. The graph shows virtually no displacement until the top interface begins to crack. The initial vertical line is not exactly zero and it may be due to the vibrations from the testing machine. The extension rods of the LVDTs were not secured to the brackets to prevent them from being damaged so any external movement is read by the LVDTs. Large displacements indicated the first sign of cracking, which was also confirmed by the test pictures. From Figure 61, the initial crack for specimen HB-2 was around 4,200 lb which can also be seen in Figure 56 (i.e., the end of the linear region).

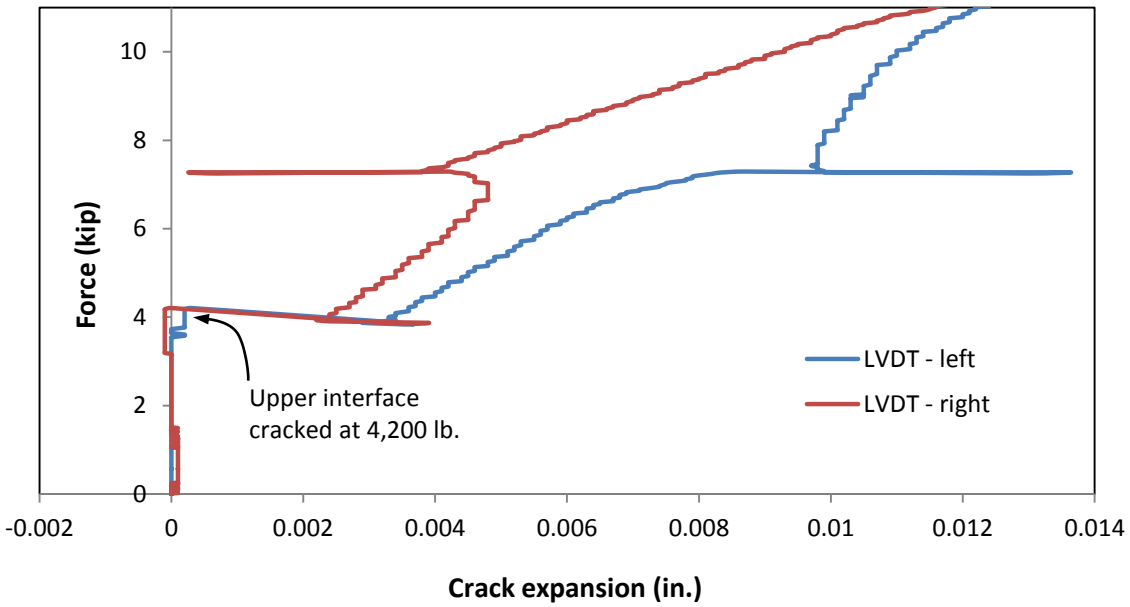

Figure 61. Force vs. crack expansion for HB-2.

Table 12 shows the force values corresponding to the interface cracking and the maximum specimen capacity. Cracking and ultimate loads are graphically shown in Figure 62. As shown in Figure 60, HB-1 has a different total force versus force in the head curve compared to the rest of the specimens. In addition, it has much lower cracking force and much larger ultimate force. For these reasons, this specimen is not included in the cracking force and ultimate force averages. The average values for the cracking force and ultimate force are 5,820 lb and 12,511 lb, respectively. The last column of Table 12 shows the stresses in the upper bar at the ultimate loads. These values were obtained by dividing the ultimate specimen force by the area of No. 5 bar. Note that the upper connection of the United machine is directly attached to the upper No. 5 bar.

Table 12. Headed bar pull-out test forces and stresses.

Sample	Cracking force (lb)	Force carried by the head at cracking force (lb)	Ratio of force in the head to the specimen force in the linear region	Ultimate Force (lb)	Force carried by the head at ultimate load (lb)	Ratio of force in the head to the specimen ultimate force	Stress in the upper bar at ultimate force (ksi)
HB-1	3,245*	193*	0.06	15,176*	7,085*	0.47	49.0*
HB-2	4,206	214	0.06	11,949	4,167	0.35	38.5
HB-3	5,661	184	0.04	12,275	3,116	0.25	39.6
HB-4	6,420	235	0.04	13,589	3,004	0.22	43.8
HB-5	5,362	311	0.06	12,222	3,617	0.30	39.4
HB-6	7,451	253	0.03	12,522	3,674	0.29	40.4
Avg.	**5,820**	**239**	**0.05**	**12,511**	**3,516**	**0.28**	**40.3**

*HB-1 force values were not included in average values.

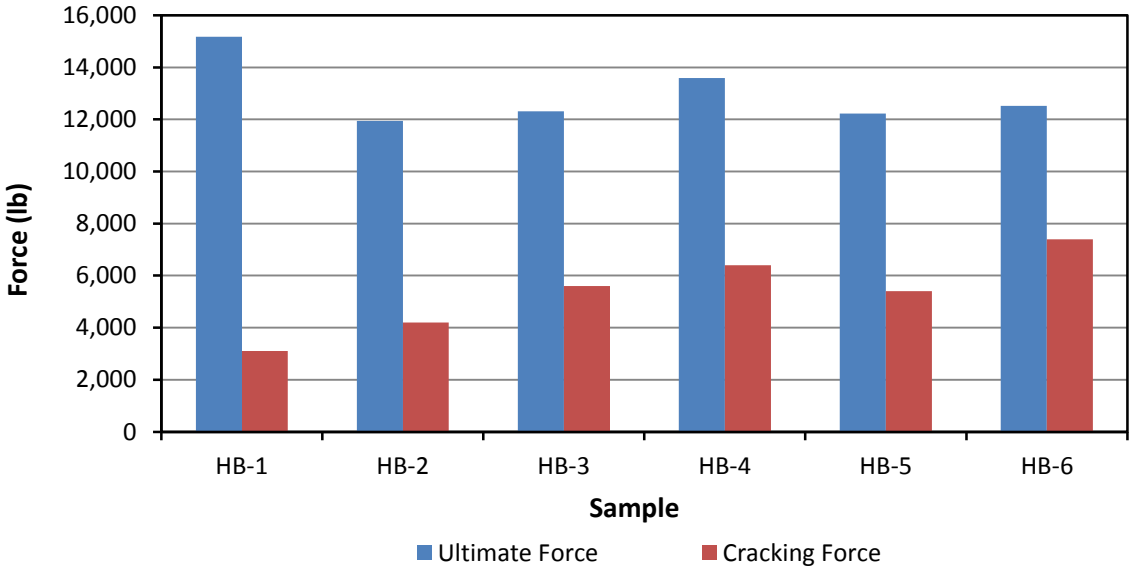

Figure 62. Headed bar pull-out force values.

Figure 63 shows a typical force versus average strain in the upper, middle and lower concrete strain gages. Since at each location, there are two strain gages, each curve represents the average response of strain measured in front and back of the specimen. The upper and middle strain curves show the strains at the interface for precast and closure pour materials, respectively. While, the lower strains are at the center of the closure pour. As seen in Figure 63, after reaching the cracking load, the strain gages at the top interface showed a significant drop in strain. After specimen cracking, the top and middle strain gages did not show useful data. Strain in the lower strain gage increased until cracking was reached, at which point there was a slight decrease in the force. After cracking, the lower strain stayed somewhat

constant and then increased with the increase in load until failure. As it can be seen from Figure 59, concrete strains are initially linear, but the behavior becomes highly nonlinear. This was the case for all the pull-out tests. More data on concrete strains are presented in the thesis by Casanova, M. (2018).[49]

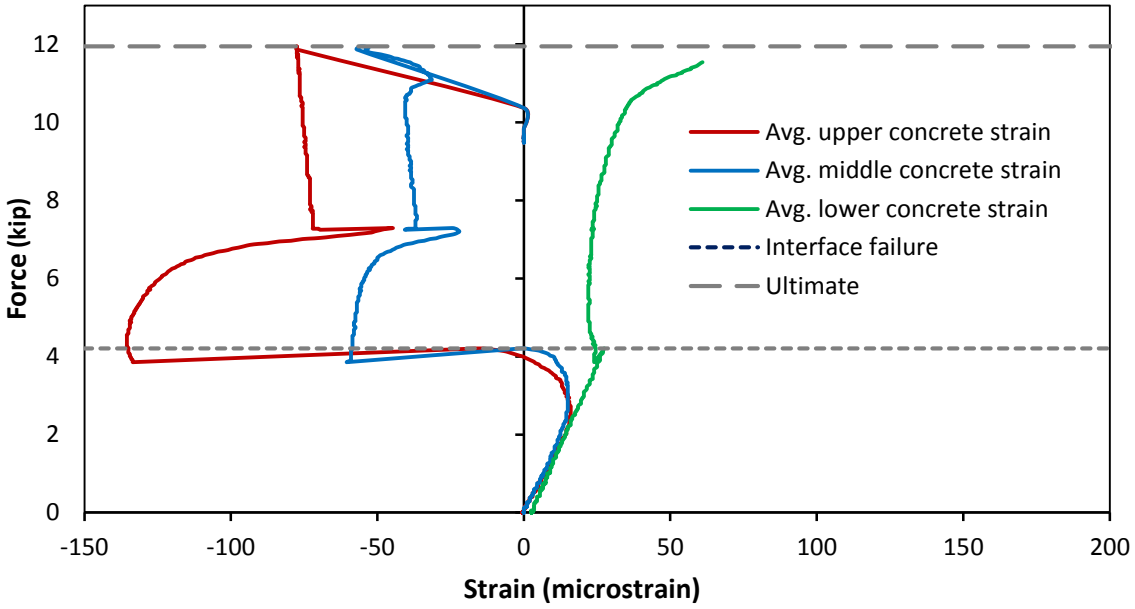

Figure 63. Force vs. average concrete strain for HB-1.

Large Beam Tests

Flexural beam tests were the final phase of the experimental work. Figure 60 shows a typical test for a beam in three-point bending. Two sets of beam specimens were prepared; three beams were used for testing in three-point bending and three were tested in four-point bending. As described in Chapter 3 section titled Flexural Beam Test, the distributed loading represents the footprint of a set of truck tires. Large beams (LB) designated with 1, 3, and 5 were tested in three-point bending, and the beams designated with 2, 4, and 6 were tested in four-point bending.

Figure 64. Typical three-point flexural beam test.

Closure connections were cast in sets of two, so LB-1 and LB-2 were cast on the same day. Similarly, LB-3 and LB-4 were cast on the same day, as were LB-5 and LB-6. Material property tests were conducted with each set of beams. In all cases, the age of closure pour concrete was 28 days and the precast concrete was 119-123 days.

Material Properties

Similar to the headed bar pull-out tests, sets of cylinders were used to determine material properties of the precast and closure concrete for computer modeling. Concrete properties included: compressive strength, splitting tensile strength, modulus of elasticity, and Poisson's ratio. Table 13 shows the summary of material properties for beam specimens. Average compressive and splitting tensile strengths for the closure pour concrete and precast concrete were similar to the averages from the headed bar pull-out tests. Compressive strengths were 8,354 psi and 4,969 psi for closure pour concrete and precast concrete, respectively. Split tensile strengths were 773 psi for closure pour concrete and 596 psi for the precast. Modulus of elasticity and Poisson's ratio values were within the ACI design-recommended range. More data on the compressive and tensile strength, modulus of elasticity, and Poisson's ratio can be the found in the thesis by Casanova, M. (2018) and its Appendices D, E, and G.[49]

Table 13. Beam concrete material properties summary.

	Compression strength (psi)	Split tension strength (psi)	Modulus of elasticity (ksi)	Poisson's ratio	Age (days)
Closure	8,354	773	4,425	0.176	28
Precast	4,969	596	3,181	0.154	119-123

Test Results

Beam specimens were tested as described in Chapter 3. Beams were prepared for testing by attaching concrete strain gages as described in Chapter 3 in section titled Specimen Instrumentation. Strain gages were attached to the concrete on the underside of the closure concrete. A coat of white paint was applied to the middle sections of the beam and the interface outlined with marker as shown in Figure 65. Similar to the pull-out tests, the paint assisted with identifying the formation of cracks.

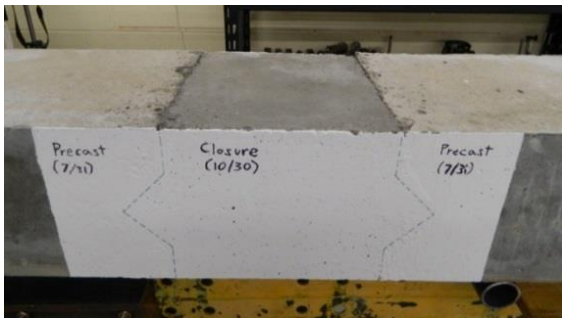

Figure 65. Beam specimen painted and interface lines drawn.

Figure 66 shows the two beam loading diagrams. The loading for the three-point bending is not a true three-point loading due to the one-inch thick steel plate distributing the load. Even though it is a distributed load it will be referred to as three-point bending. The steel plate with dimensions 20 in. x 10 in. x 1 in. was placed in the center of the beam. The plate distributed the load as seen in Figure 66. The load is assumed to be uniformly distributed along the length of the plate. For calculating the moment, the measured load from the machine is divided by 20 inches. The equation in Figure 67 is used to calculate the moment for the three-point bending. The equation in Figure 64 is used to calculate the moment for the four-point bending case.

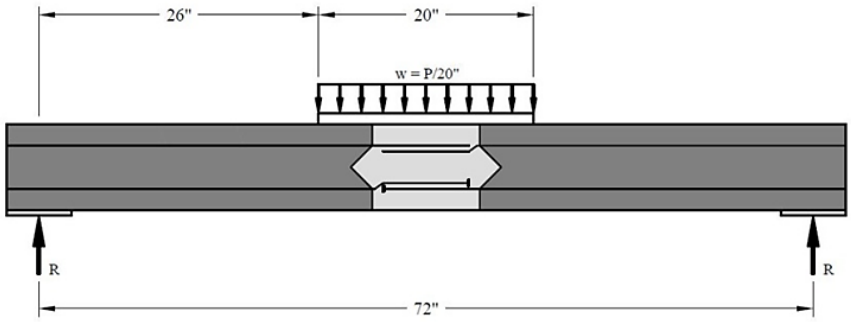

(a) Three-point loading

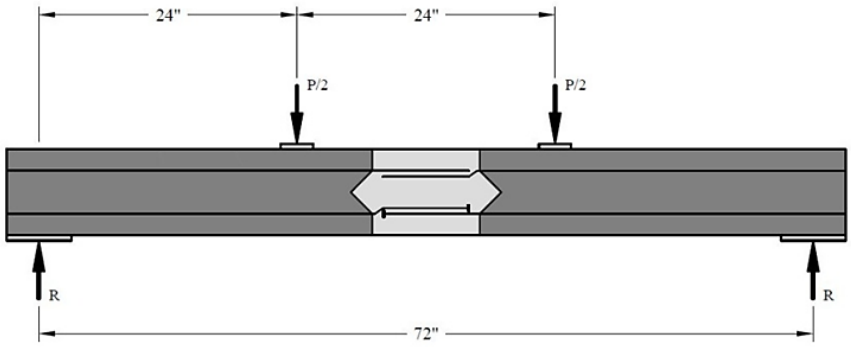

(a) Four-point loading

Figure 66. Beam loading diagrams.

$$M = R\left(a + \frac{R}{2w}\right)$$

Figure 67. Moment equation for the three-point loading.

Where,

M = Maximum (mid-span) moment (lb-in),
R = Support reaction = $\frac{P}{2}$,
w = Distributed load = $\frac{P}{20"}$ (lb/in.),
a = Distance from the end support to the start of distributed load = 26 in.

$$M = Rb$$

Figure 68. Moment equation for the four-point loading.

Where,

M = Maximum beam moment (lb-in),

R = Support reaction = $\frac{P}{2}$,

b = Distance from the support (reaction) force to the force at the one-third location used in the four-point flexural beam test = 24 in.

For the three-point loading, distributing load over the 20 in. x 10 in. steel plate was not ideal. The top surface of the beam was not perfectly flat. Gaps between the steel plate and the beam could be seen. A rubber pad was added under the loading plate for samples LB-3 and LB-5 to provide an evenly distributed load and to minimize gaps. The rubber reduced gaps between the steel plate and the concrete with only a few larger gaps visible.

The testing schematic shown in Figure 69 identifies the instruments and equipment for beam tests. The schematic refers to the designations for “left” and “right” instrumentation. A computer monitor and cameras were set up to monitor and record the progress of the tests.

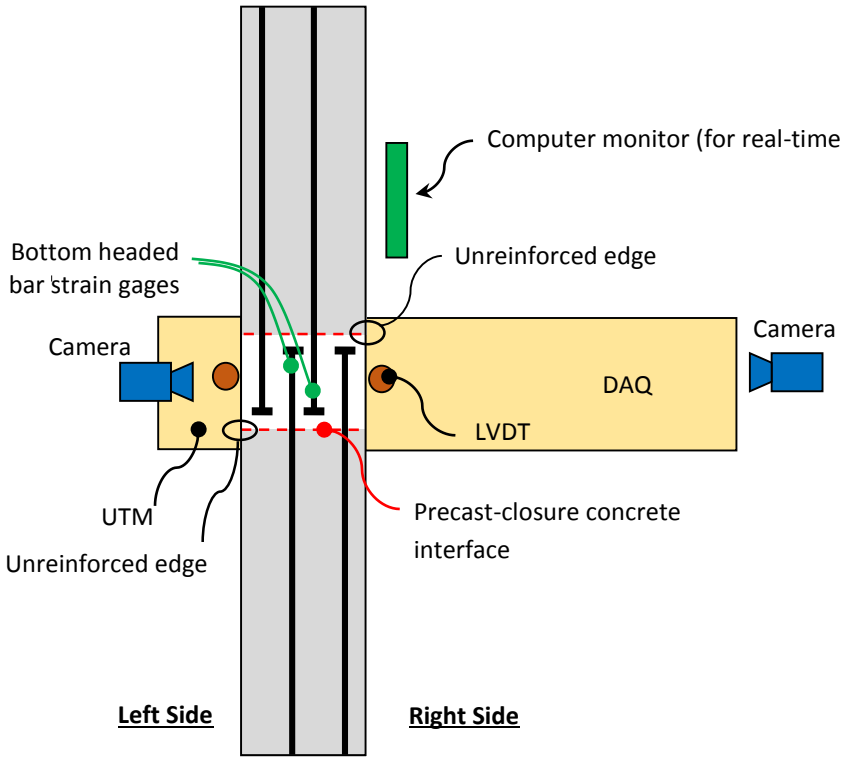

Figure 69. Flexural beam test schematic (top view).

Figure 70 shows the series of pictures taken while specimen LB-5 (one of the three-point loaded beams) was being loaded. Cracks first appeared at the bottom of the right interface. In this test, the ultimate force was 9,052 lb. But, the loading continued until the applied force deceased to about 6,000 lb.

The beam failure for LB-2 is shown in Figure 71. After testing the beam's cracking was mapped by indicating the sequence in which they appeared. The sequence of numbers represents the stages of cracking which are defined as:

1. **Primary**: Precast-closure interface cracked (at both interfaces) and propagated up along the shear key.
2. **Precast**: Several smaller cracks formed (1-3 in. long) in the precast segments. These occurred prior to reaching the ultimate beam capacity.
3. **Shear**: Shear crack started from the lower corner of the shear key and extended up toward the opposite interface. This occurred after reaching the ultimate beam capacity.
4. **Secondary**: Cracks formed as a result of excess deflection. These occurred well beyond the ultimate load.

Figure 72 shows a diagram of the typical cracking for flexural beam specimens. The crack appeared on the unreinforced edge on both sides of the beam. The secondary cracks were mainly to observe the cracks extending toward the top of the beam. After inspecting the beams no cracks were seen extending to the surface. The secondary horizontal cracks were 0.5-1 in. below the surface. Figure 73 shows the cracks on both sides of all the beam specimens beyond the ultimate load.

Figure 74 shows the bottom of LB-1. Cracks in the connection portion as well as in the precast concrete can be seen. Longitudinal cracks (along the length of the beam) formed below the two headed rebars in the middle of the beam as seen in Figure 74. Precast cracks can be seen marked in red located about 8 inches away from the connection.

In all cases the shear crack always formed on the lower right and extended to the top left of the connection. This was a result of the reinforcing and the width of the beam. The right side of the connection was unreinforced as shown in Figures 69 and 74(b). Primary cracks on the right side of the connection were also much larger than the cracks on the left side.

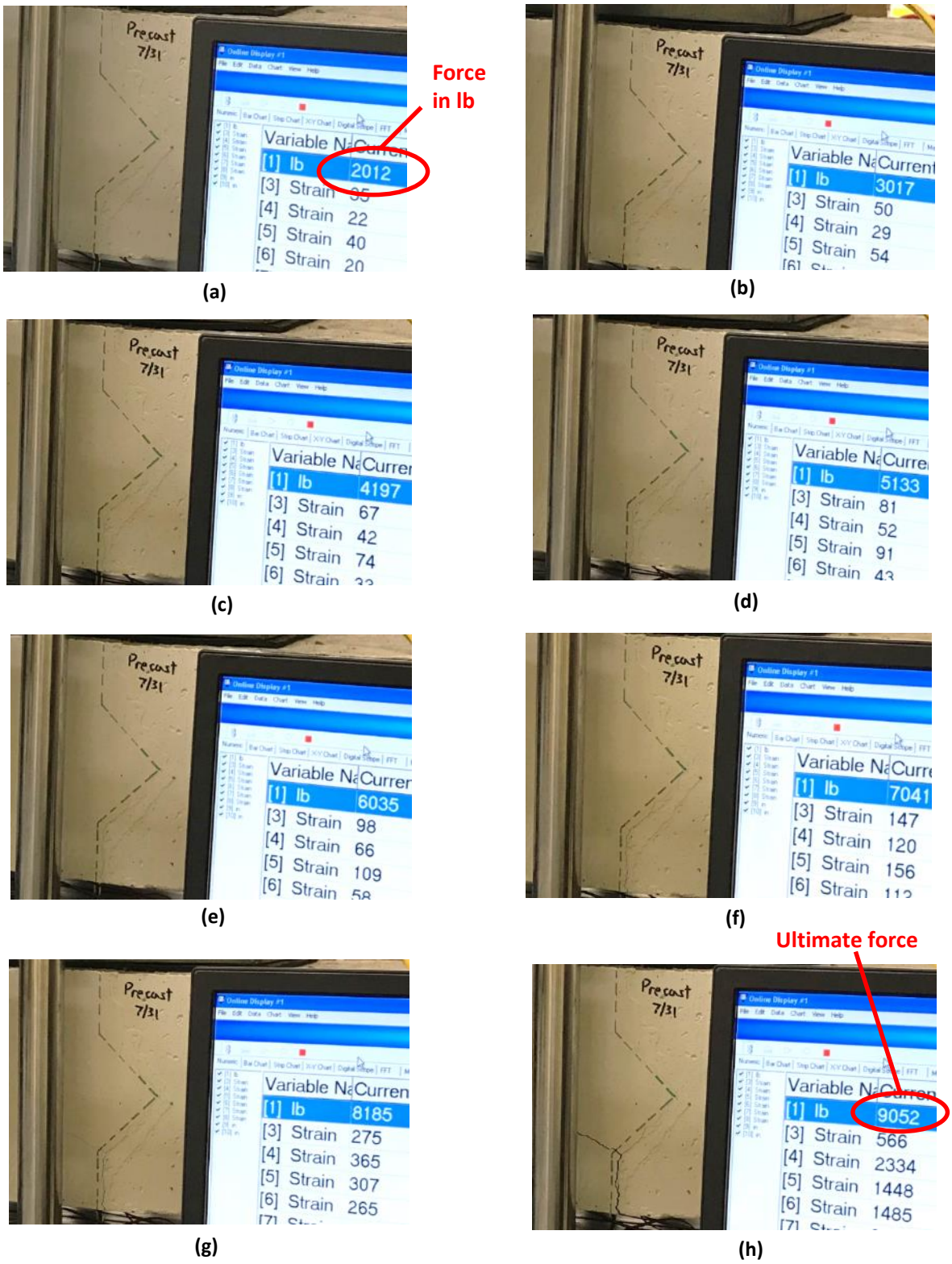

Figure 70. Selected pictures during testing of specimen LB-5.

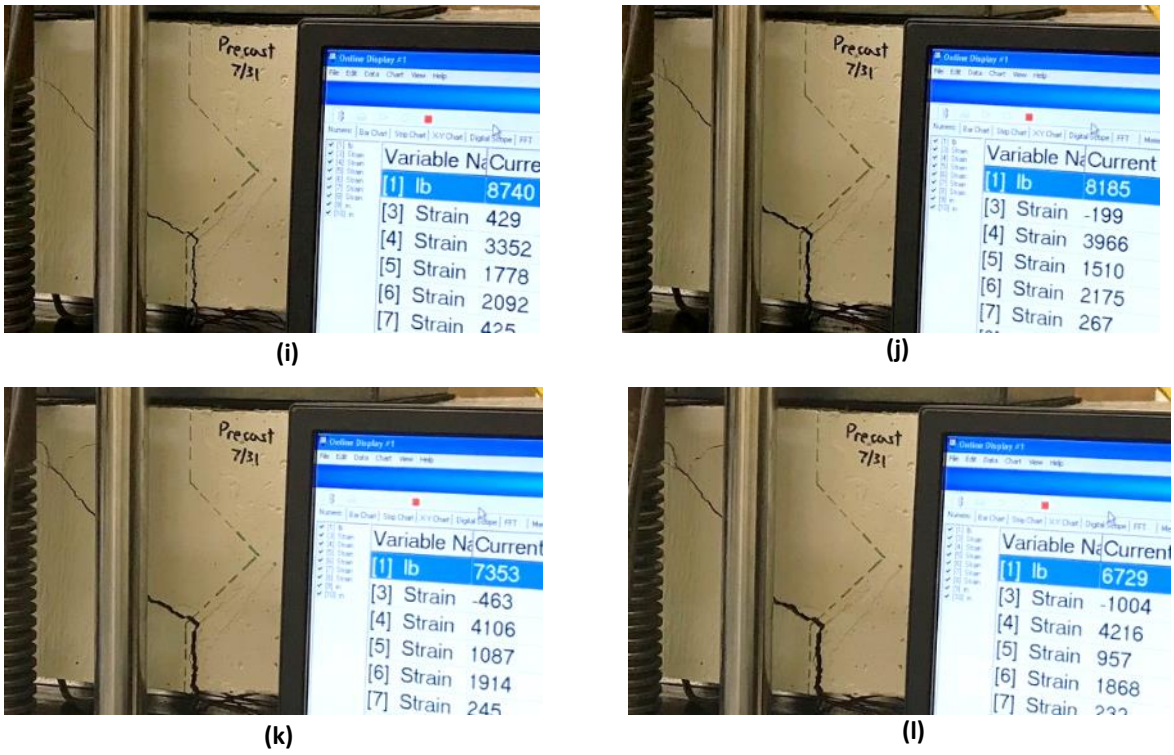

Figure 70, continued. Selected pictures during testing of specimen LB-5.

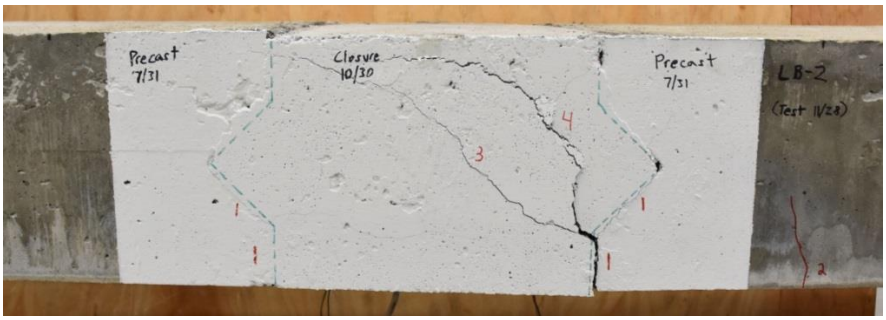

Figure 71. Beam cracking for specimen LB-2.

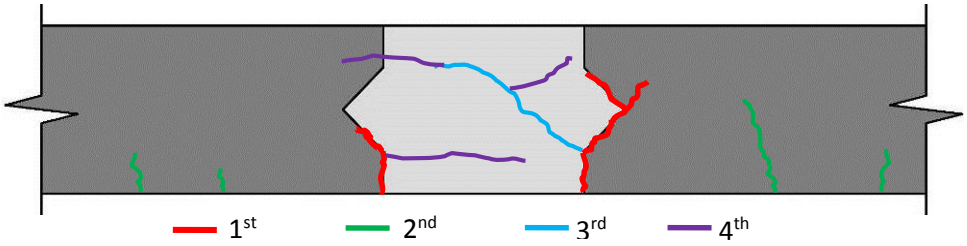

Figure 72. Typical beam cracking diagram.

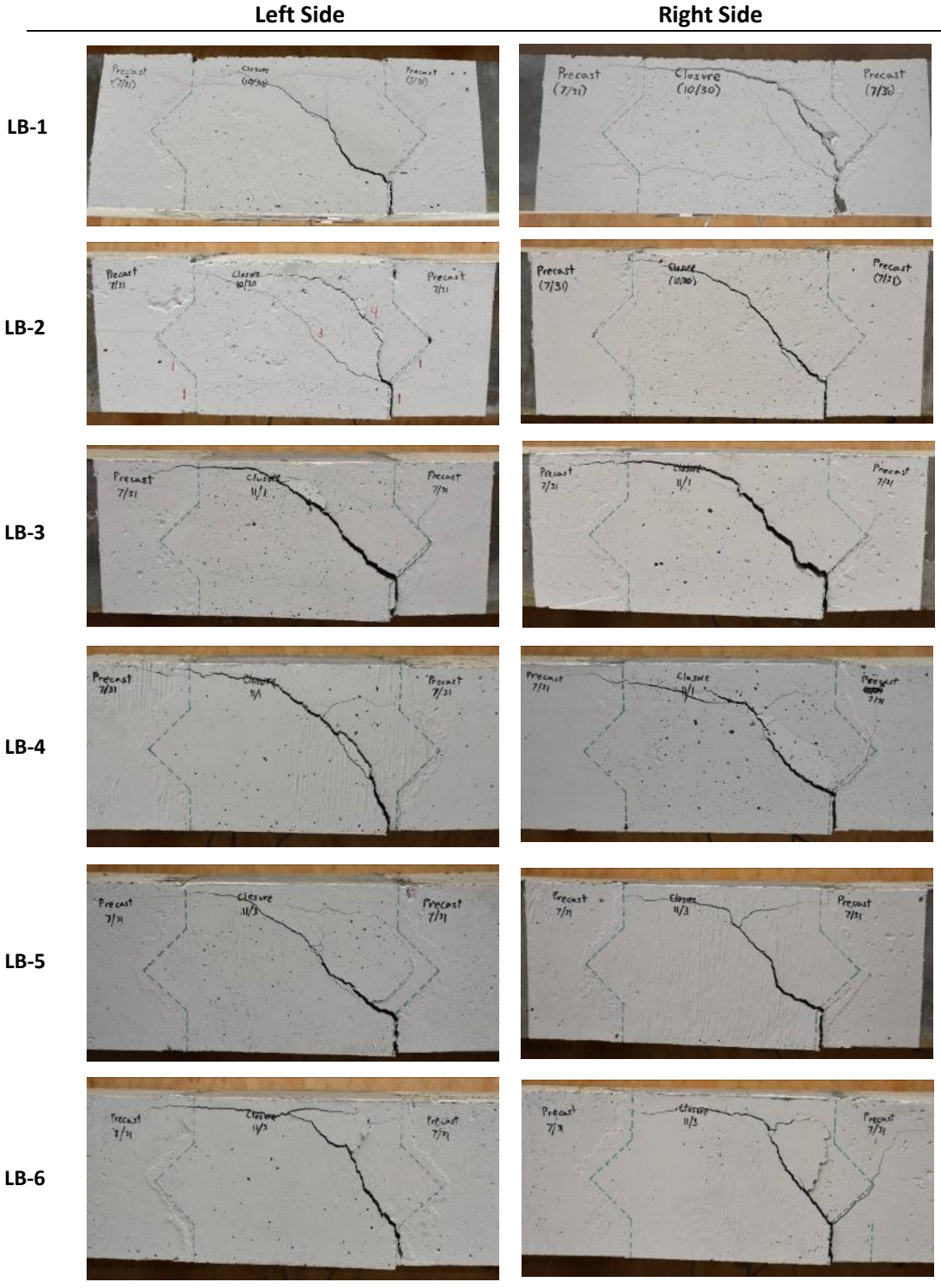

Figure 73. Beam specimen cracks beyond the ultimate load.

(a) Side view

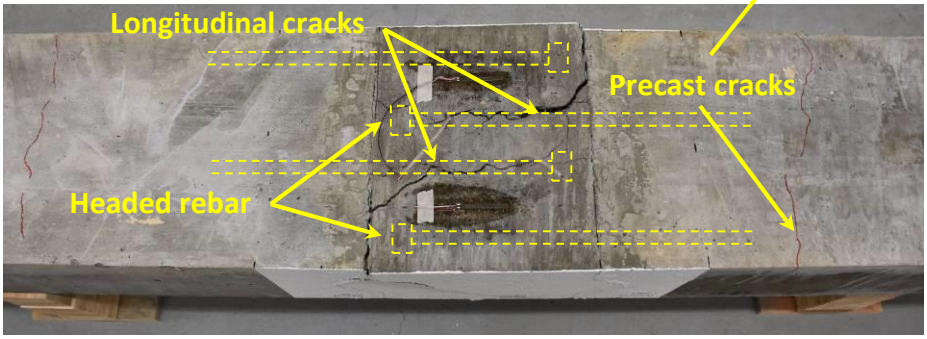

(b) Connection cracks

Figure 74. Cracking on bottom of specimen LB-1.

The beam force-deflection graphs for all six beams tested are shown in Figure 75. The solid lines represent the beams under three-point (3P) bending and the dashed lines represent beams under four-point (4P) bending. Performance of beams LB-1, LB-3, and LB-5 was similar. This is also the case for LB-2, LB-4, and LB-6. Ultimate forces are also identified in Figure 75. Similar to the headed bar tests, the point of cracking load was not easily determined. The cracking load was determined from visual observations of the interface.

Figure 76 shows the relationship between the mid-span moment and stress in the bottom middle two rebars next to the head. The stress values were calculated from the strain gages data next to the head (see Figure 70).

A summary of average values for large beam tests is shown in Table 14. The values correspond to the cracking and ultimate forces and moments. Mid-span deflection values at the ultimate forces are also given in Table 14. Refer to Appendix J of the thesis by Casanova, M. (2018) for graphs and data of the flexural beam tests.[49]

As shown in Table 14, the average interface cracking forces are estimated at 2,867 lb and 2,933 lb for three-point and four-point bending tests, respectively. The corresponding averages of ultimate forces are 9,492 lb and 12,209 lb, respectively. The average mid-span moments are 44.4 kip-in. and 35.2 kip-in. for three-point and four-point bending tests, respectively. The corresponding averages of ultimate moments are 147.1 kip-in. and 146.5 kip-in., respectively.

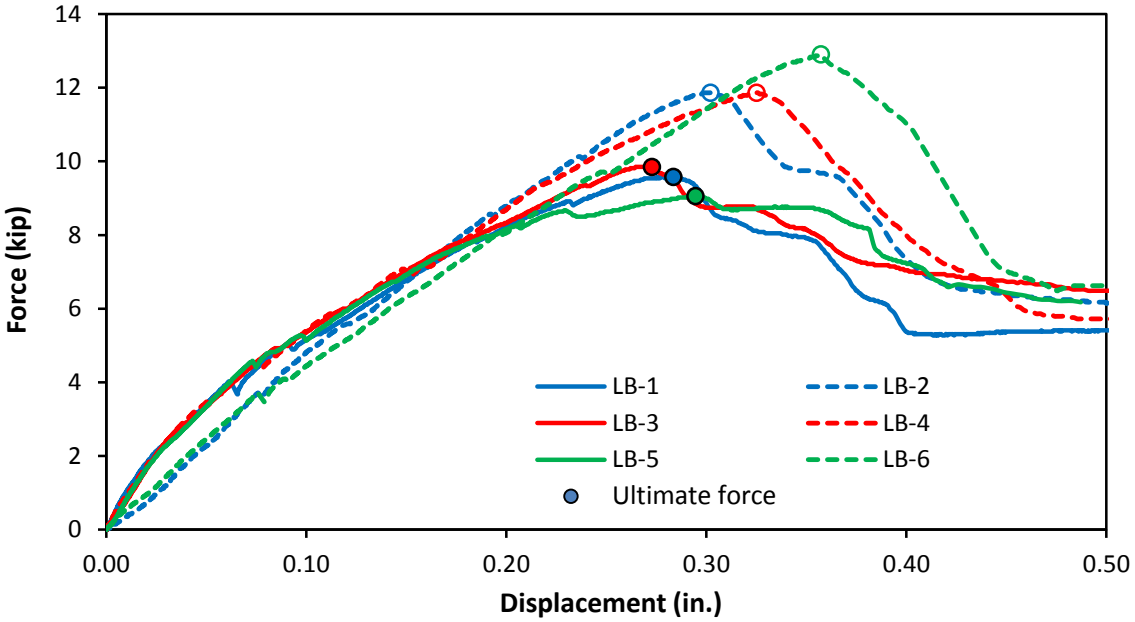

Figure 75. Beam force vs. deflection.

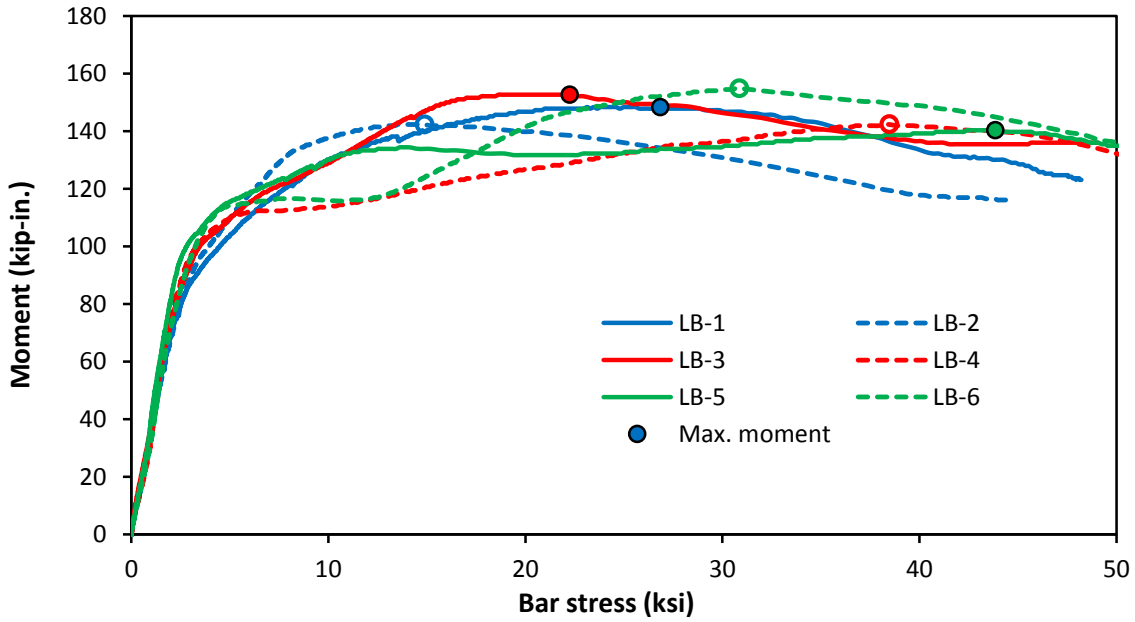

Figure 76. Mid-span moment vs. rebar stress next to the bar's head.

Table 14. Summary of beam test results.

Test type	Sample	Cracking force (lb)	Cracking moment (kip-in.)*	Ultimate force (lb)	Ultimate moment (kip-in.)	Mid-span displacement at ultimate force (in.)
3-point	LB-1	3,300	51.1	9,573	148.4	0.281
	LB-3	3,000	46.5	9,850	152.7	0.273
	LB-5	2,300	35.7	9,052	140.3	0.295
	Avg.	**2,867**	**44.4**	**9,492**	**147.1**	**0.283**
4-point	LB-2	3,500	42.0	11,862	142.3	0.302
	LB-4	2,800	33.6	11,862	142.3	0.326
	LB-6	2,500	30.0	12,902	154.8	0.357
	Avg.	**2,933**	**35.2**	**12,209**	**146.5**	**0.328**

* For the three-point bending test, the moment is calculated at the center, although crack is at the interface.

Concrete strain gage data is plotted against the beam mid-span moment in Figure 77 for three-point bending beams (i.e., specimens LB-1, LB-3, and LB-5). The strain behavior is similar to the interface strain data for the headed bar pull-out tests. The curves show an increase in strain up to approximately 50 microstrain, then decrease until failure. Figure 77 also shows the points where the initial hairline cracks were observed at the interface. This is where the curves begin to behave more nonlinear. Inspecting the strain gages revealed that cracking had occurred under some of the gages and some showed partial debonding. More data and discussions on beam concrete strain gages are provided in thesis by Casanova, M. (2018).

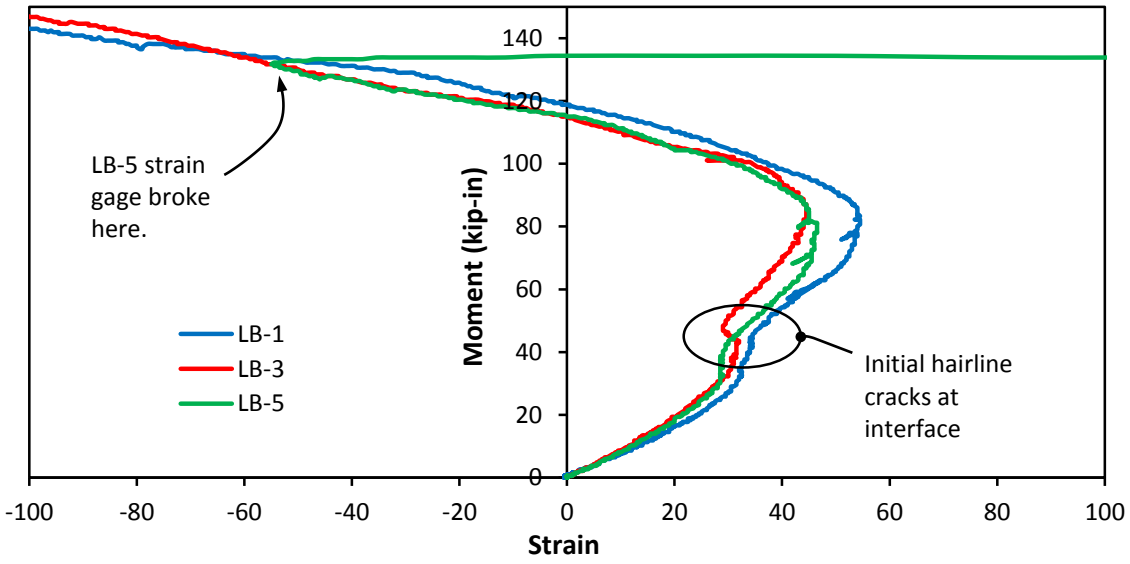

Figure 77. Moment vs. average concrete strain for beams under three-point load.

Discussion on Headed Bar Pull-out and Beam Test Results

This section provides a discussion on the experimental results of the headed bar pull-out tests and the beam tests. For the pull-out tests, strain gages were installed on the upper steel bar and several locations on the concrete. In addition, crack initiation at the upper interface was monitored. Among all the data, we believe the most useful information is provided by plots of total tensile force in the specimen versus the force carried in the head of the upper bars. This figure will be used in FE modeling in the next Chapter. Out of the six curves, one seems not to follow the general trend of the other five (see the graph for HB-1 in Figure 56) and was eliminated when comparing to the FE results.

Despite the fact that the upper interface between the precast and closure pour concrete completely failed in the headed bar pull-out tests, the upper bar on the average carried 40.4 ksi or 67% of the steel specified yield strength. This shows that the strut action and the force transfer between the opposing lapped bars works rather effectively.

In the beam tests, the strain gages were installed on the lower two headed bars, the bottom concrete, and displacements were measured at mid-span. In both cases of three-point bending and four-point bending, the initial crack always formed on the lower right (as one views the beam from either side) and extended to the top left of the connection. This was a limitation of the beam specimens; i.e., unsymmetrical placement of reinforcing and the small width of the beam. To explain this somewhat differently, the unsymmetrical placement of bars causes the unreinforced interface edges (see Figures 69 and 74) to be less stiff than the reinforced interface edges. Thus, causing the unreinforced edges to deform more under a given force and impose a twisting moment in the middle of the beam.

As an estimate, if one were to use the cracking moment formula of $M_{cr} = f_r\, I_g/y$, where $f_r =$ interface bond strength (modulus of rupture) = 612 psi, I_g= gross moment of inertia, and y = half the beam depth, a cracking moment value of 78.3 kip-in will be determined. This value is much larger than the cracking moment values obtained from the experiments (see Table 14), confirming that the interface cracks appeared much earlier than anticipated.

Regardless of the loading, the average ultimate moment in the beam specimens was approximately 147 kip-in. As a comparison, if one were to ignore the upper bars, assume that two continuous No. 5 bars are placed at the bottom, and assume the entire beam is made with precast concrete, the nominal bending moment capacity of 210 kip-in. is calculated. Therefore, the nominal moment capacity, M_n, of the beam with closure pour and lapped headed bars in the middle is 70% of that calculated for a beam with continuous bottom bars.

The mid-span moment versus the stress next to the head of the headed bars provided the most useful information. This plot will be used for comparing results with the FE model results. As expected, Figure 76 shows that initially the bar stresses vary linearly with increasing bending moment, and then the relationship becomes nonlinear until ultimate moment is reached.

Chapter 5
Finite Element Modeling

Introduction

Finite Element (FE) modeling has been a useful tool in modeling structural and other engineering problems for several decades. In this chapter, various approaches have been evaluated to model pull-out behavior of headed rebars in concrete. To test the accuracy of the developed models, test results from previous experimental studies have been compared with the FE results. For developing and simulating the finite element models, ANSYS 18.1, a general-purpose FE software was used.[59] This software has the capability to simulate linear and nonlinear structural, fluid, electromagnetic or thermodynamic problems. The structural analysis capabilities of ANSYS were used for this study. ANSYS offers a variety of options in terms of element and material selection. Some of the options that were considered in this study are discussed in the following sections. Detailed information is provided in the thesis by Rashique, U. (2018).[30]

Concrete Element and Material Properties

SOLID65

SOLID65, also known as CONCRETE65, is an 8-node brick element to model 3D solids with or without reinforcing bars. See Figure 78. The reinforcing bars can be modeled using the native "smeared rebar" option where the rebars can be defined to be smeared throughout the element in three different directions. This can be input as three real constants each having four parameters named MAT, VR, THETA and PHI. MAT and VR are the material properties and volumetric ratio of rebars with respect to concrete in a particular direction, respectively. THETA and PHI are the directions in terms of angels from the x-axis toward the y and z-axes in the global coordinate system. Moreover, the SOLID65 element has a unique capability of crushing and cracking in compression and tension, respectively. The crack at an integration point is represented by introducing a plane of weakness in the direction of cracking; i.e., the material turns from isotropic to orthotropic. When the element crushes due to compression at an integration point, it is defined as the complete deterioration of the structural integrity of the material and the structural stiffness at the integration point in question can be ignored. To determine the failure in tension and compression, the William-Warnke failure criterion is employed.[60] These features make it a very suitable element to model concrete. But it is also to be noted that, these features introduce nonlinearities in the FE model and often create convergence problems.

Cast Iron Model

With the default material specification option in ANSYS, the plasticity curve is mirrored in both tension and compression. But this is not suitable for materials like concrete that have different compressive and tensile strengths. To model different tensile and compressive properties, the Cast Iron material model in

ANSYS can be used. It was originally developed to model grey cast iron which is a two-phase material with different compressive and tensile behavior (Hjelm, 1994).[61]

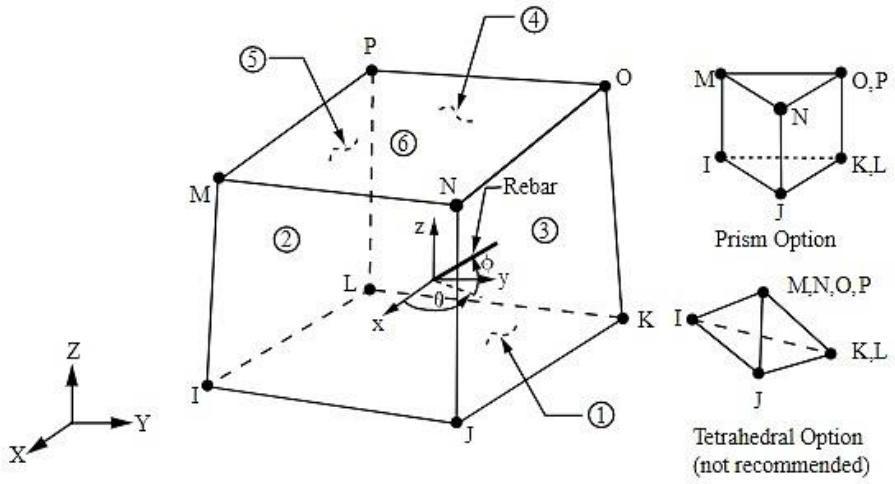

Figure 78. Geometry of SOLID65 element.[59]

There are three input parameters: plastic Poisson's ratio, uni-axial compression and uni-axial tension. The latter two are input as sets of stress-strain points representing multi-linear isotropic hardening behavior. These points are obtained from the uni-axial compression and tension tests of the material respectively. Plastic Poisson's Ratio is an FE modeling concept to address plasticity problems with a changing Poisson's ratio.

Concrete-Rebar Bond Modeling

As discussed in Chapter 2, the bond between concrete and reinforcing bars is a complex phenomenon to formulate. It also adds nonlinearities to the FE model that can create convergence issues and increase computation time. To overcome these problems, the concrete and rebar are often assumed to be perfectly bonded in FE simulations where it is reasonable to assume that the localized effects of bond-slip will not have a significant effect on the results. Otherwise, the bond-slip relations is to be incorporated into the model. There are various options in ANSYS to simulate the bond-slip response between steel and concrete.

COMBIN39

COMBIN39 is a nonlinear spring model that can be used in 1-D, 2-D or 3-D simulations. It can have a zero or non-zero length. The non-zero length spring elements are generated between two coincident nodes and have 1-D application only. The spring stiffness is input as points in a force-displacement curve. This element can be used as interface element between steel and concrete similar to that proposed by Ngo and Scordelis (1967) discussed in Chapter 2.[41]

Contact Debonding and Interface Delamination

Contact debonding and interface delamination are two techniques in ANSYS that can simulate progressive separation of a bond. Both methods are essentially the same in most aspects. The difference is that debonding is associated with contact elements and delamination is associated with interface elements. Contact elements are used to define other contact features (friction, perfect bond, frictionless sliding, etc.), but the interface elements do not have these capabilities. Debonding and delamination can be modeled using two methods: Cohesive Zone Model (CZM) method and the Virtual Crack Closure Technique (VCCT) method. The CZM method is bond shear-separation distance based, while the VCCT method is based on fracture energy. The CZM method is simpler and more suitable for modeling steel-concrete bond. There are two methods of formulation for the CZM method: bilinear and exponential. They model the bond traction (τ) and relative displacement of the two surfaces (δ). Both the curves have two arms, one that reaches to the maximum bond stress and the other one represents the subsequent softening of the bond. The bilinear CZM method is shown in Figure 79.

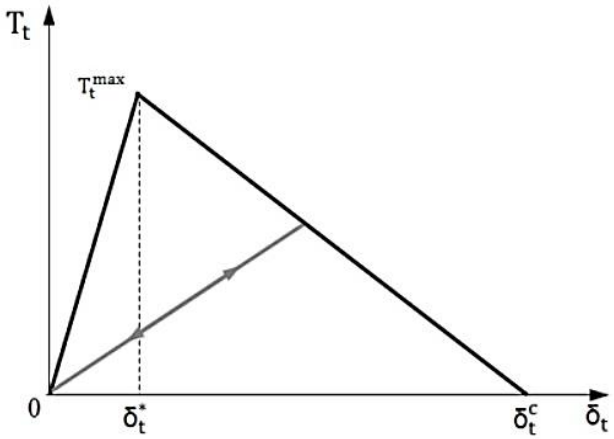

Figure 79. Bilinear CZM method graph.[59]

Verification using a Simple Concrete Model

The first step in modeling the specimens used in this study was to decide on suitable modeling techniques. It was convenient to use the SOLID65 element along with the William-Warnke criterion for modeling concrete because of the element's cracking capability. Using the appropriate parameters, a simple axial concrete model with both ends tapered (i.e., smaller cross-section in the middle region and larger cross-sections at the ends) was loaded in tension and compression. This model eliminated the stress concentrations at the ends and forced the cracks to appear in the middle section. Both the tensile and compressive stress-strain graphs obtained from this model matched the input material stress-strain model. The verification described is presented in detail in the thesis by Rashique, U. (2018).[30]

Calibration of the Bond-slip Spring Element

To use the COMBIN39 element, a force versus displacement curve has to be defined for each element. In this case, this curve should closely resemble the bond-slip behavior for the particular model. From the studies of Hong et al. (2008), an equation to determine bond stress in terms of shear stress per unit interface area can be obtained:[48]

$$\tau_b = 0.9(f_c')^{2/3}\left\{1 - exp\left[-40\left(\frac{S}{d_s}\right)^{0.6}\right]\right\}$$

Figure 80. Bond stress versus bond slip.[48]

Where, τ_b= bond stress, f_c'= compressive strength of concrete, d_s= bar diameter and S = bond slip. Values of τ_b are obtained for different values of S using the above equation. Then the bond stress values can be multiplied by $\pi d_s l$ where l = embedment length of the bar, to obtain the bond force value. These force values are to be divided by the total number of springs to produce the force versus displacement curve for each spring connecting steel bar and concrete element nodes. Figure 81 shows a typical force-displacement for a bond-slip spring element.

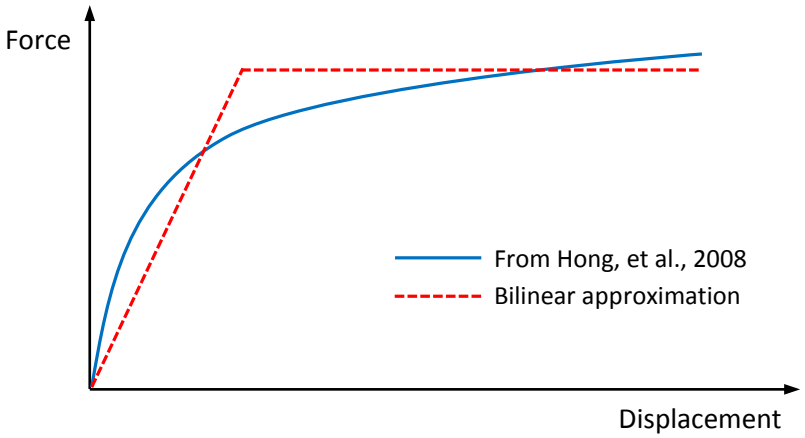

Figure 81. Force-displacement curve used for the bond slip springs.

However, the equation in Figure 80 already takes the crushing and failure of concrete around the rebar into account. If this equation is used to model bond-slip where cracking/failure criteria are defined for the concrete, the model will produce a softer response. Because the transference of force from the springs to the adjacent concrete will cause the concrete to fail. But this failure has already been addressed in the force-displacement definition of the spring. Therefore, in the FE model used in this study, the force-displacement curve for a spring element was adjusted. To calibrate this curve, a simple pull-out test of a regular deformed bar conducted by Rao et al. (2007) was modeled in ANSYS 18.1.[35] In this experiment, as shown in Figure 82, a No. 5 steel bar was embedded in a concrete cube of dimension 6 in. x 6 in. x 6 in. The development length of the bar was 6 in. For other details, see the thesis by Rashique, et al. (2018).[30] A known upward

displacement was applied on the top surface of the rebar. The four edges in the top surface of the concrete cube were constrained.

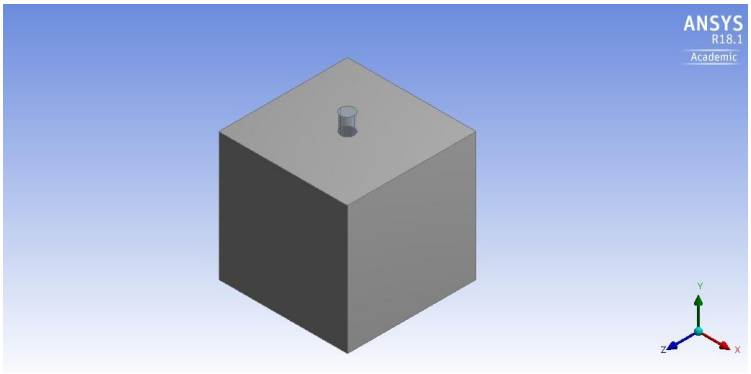

Figure 82. Geometry of the simple pull-out test by Rao et al. (2007).[35]

96 COMBIN39 spring elements were created at the interface between the steel and concrete. Their force-displacement curves were assigned the bilinear approximation shown in Figure 81. The concrete and steel were modeled using SOLID65 and SOLID186 elements, respectively. The slip of the rebar at the free end was monitored. The bond stress-slip curve obtained from the FE model had lower slope. Therefore, it was decided that the bilinear bond-slip curve for each spring had to be adjusted to have larger slope in order to give the net effect of the curve obtained from equation in Figure 80.

Finite Element Model of Pull-out Tests

As described in the Chapters 3 and 4, six headed bar pull-out specimens were tested. The specimen tested was described in a common setup for the pull-out specimens is shown in Figure 14. Nonlinear spring element COMBIN39 between steel and concrete to simulate bond-slip response. A quarter model was used in ANSYS as shown in Figure 84. SOLID65 elements were used to model the concrete parts, and the steel rebars were modeled using SOLID186, another 8-noded 3D solid element. Several ways of modeling closure pour to precast interface bond were explored. It was determined that Cohesive Zone Modeling (CZM) was the best option. Cohesive Zones were defined in the two closure-to-interface regions. Mode I Cohesive Zone Model was used which debonds only due to normal stress. The maximum normal stress for debonding was defined as 256 psi, and the contact gap at the completion of debonding was defined as 0.1 inch. The reduced value was based on the studies conducted by Kim and Taha (2014).[62] They studied the relationship between the concrete's modulus of rupture, splitting tensile strength and direct tensile strength. The relationships are given by the equations in Figure 83.

$$f_r = 0.85\sqrt{f_c'}\,; \qquad f_{sp} = 0.49\sqrt{f_c'}\,; \qquad f_t = 0.34\sqrt{f_c'}$$

Figure 83. Concrete tensile strength values in MPa.[62]

Where, f_r, f_{sp}, f_t and f_c' are the modulus of rupture, splitting tensile strength, direct tensile strength and compressive strength of the concrete, respectively, in terms of MPa. Recall that from Chapter 4 the

interface bond strength between closures pour and precast was determined as a modulus of rupture based on ASTM C78. Also, splitting tensile strength were determined for closure pour and precast concrete. For the FE analysis, the values of direct tensile strength, f_t, were used for the tensile strength of interface bond, the closure pour concrete, and the precast concrete. Using relations in Figure 83, these values were estimated as 256 psi, 556 psi and 435 psi, respectively. From experimental results, knowing that rebar is only loaded up to 67% of yield strength, the steel was modeled as a linear isotropic material with a modulus of elasticity of 29,000 ksi and Poisson's ratio of 0.3.

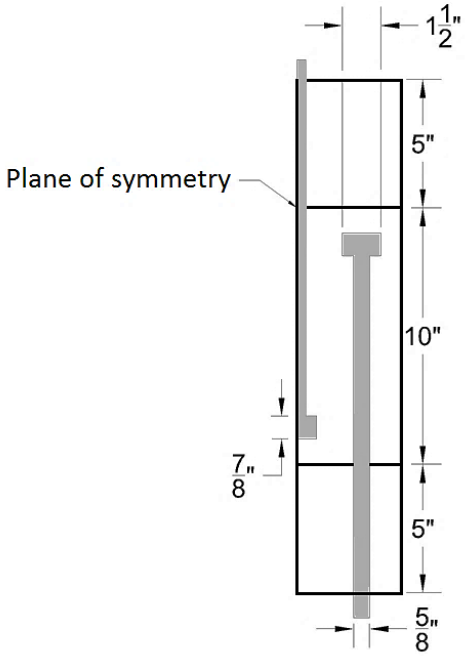

Figure 84. Schematic diagram of the pull-out test quarter model.

From the previous attempts, it was evident that the meshing of the model plays a very important role in the speed and accuracy of the simulation. The brick elements created by "sweep meshing" have a greater tendency of convergence than its tetrahedral counterparts. Also, brick meshes have better aspect ratio in general and reduce the total number of nodes and elements. This is important for SOLID65 elements, as they are highly nonlinear and often unstable due to their cracking and crushing capabilities. But manual meshing, in particular sweep meshing is a complicated task. It requires experience and patience from the person creating the mesh. A body cannot be swept, if:[(59)]

- There is a completely contained internal void in the body.
- A source and target pair cannot be found. That is, the sweeper cannot find at least one path from a source surface to a target surface connected by edges or closed surfaces.
- If a "Sizing control" is used on a body with hard edge sizing and the source and target faces contain hard divisions which are not the same for each respective edge.

To make a body "sweepable", it is often required to divide the body into several parts until each part satisfies the requirements to be swept. But, too many divisions can make the setup of the FE model very

complicated. So, a compromise has to be found based on the particular model. A model can perform in a satisfying manner if the number of tetrahedral SOLID65 elements is below 10% of the total number of elements.[59] So, a 3D quarter model was created and divided in such a way that more than 90% of it can be meshed using brick elements. Also, the sizing of the meshes had to be defined carefully so that the steel elements and the neighboring concrete elements have coincidental nodes that will be used for defining the bond-slip spring elements. The final meshing is shown in Figure 85.

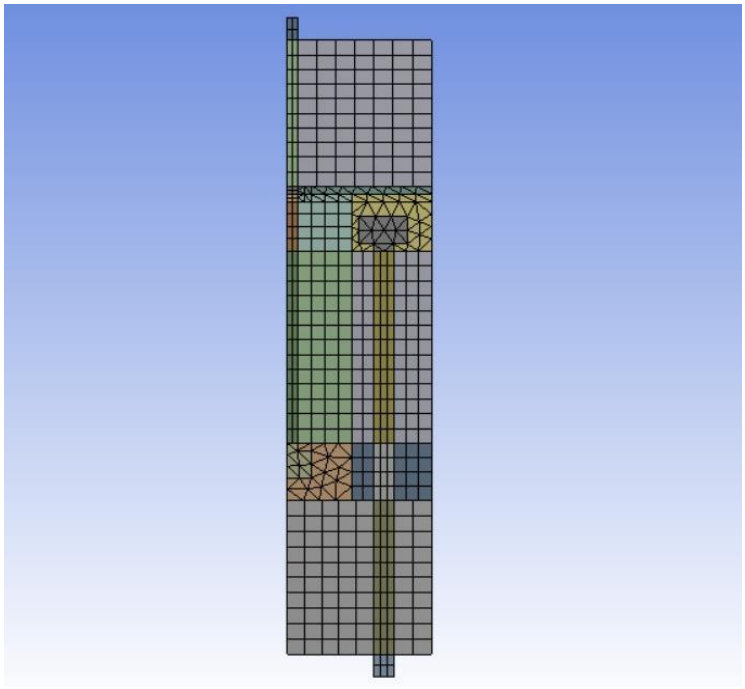

Figure 85. Meshing of the pull-out test quarter model.

Since a quarter model was used, frictionless supports were provided at the surfaces at the planes of symmetry. This allowed the nodes at those surfaces to move in the plane of symmetry, but restricted their movement normal to the symmetry planes. Constraint equations were used between the coincidental nodes of the steel and the concrete elements to restrict their movement in the normal direction. To control the movement in the tangential direction, i.e., to define the bond-slip relationship, single degree of freedom (DOF) in the tangential direction COMBIN39 elements were introduced between the coincidental nodes. As shown in Figure 87, at every 1 in. interval along the length, the quarter of the circumference of the middle rebar had three bond-slip spring elements attached to it.

Two nodes on the middle rebar near the head was monitored to obtain the strain values. Total force was obtained from the support reactions. From the strain data, force in the head was calculated using the equation in Figure 86.

$$F_H = A\varepsilon E$$

Figure 86. Equation for determining force in the steel bar's head.

Where F_H = Force in the head, A = cross-section area of the bar, ε = strain and E = modulus of elasticity of the steel. The total force versus force in the head curve was calculated from FE model results and compared to the results of the pull-out specimen experiments (see Chapter 4, Figure 60). As noted in Chapter 4, the results of HB-1 was not included in the experimental curves. Figure 88 represents the final successful simulation for the pull-out test. For details of other trials, see the thesis by Rashique, U. (2018).[30] The FE result is in very good agreement with the experimental results in the linear region. In addition, the nonlinear part also mostly remains inside the spectra of the experimental values.

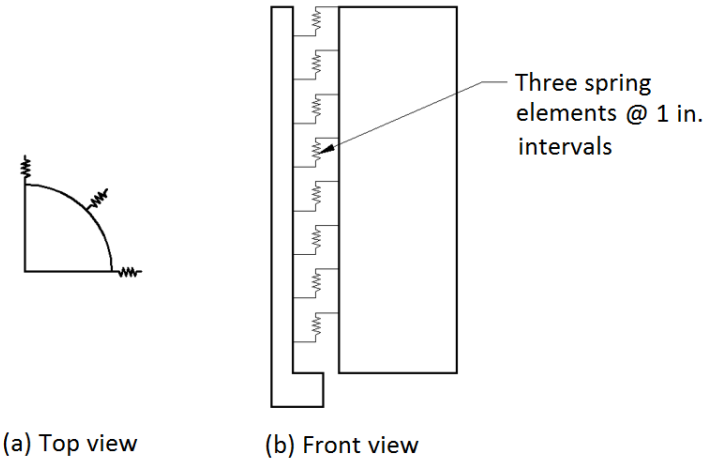

Figure 87. Schematic of placement of COMBIN39 elements between rebar and concrete.

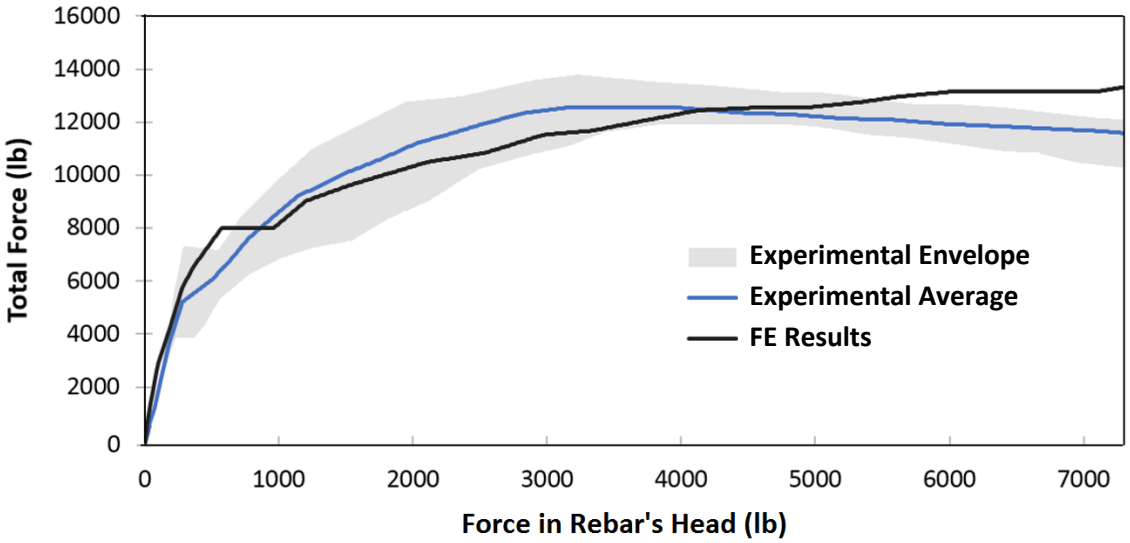

Figure 88. Total force in the pull-out specimen vs. force in the rebar's head (with bond-slip).

It can also be noticed from the FE model that, although both the precast and the closure pour concrete cracks after reaching their tensile strengths, there is no compressive crushing in concrete. The maximum compressive stress observed in the concrete was 2,100 psi, which is significantly less than the compressive strengths of both precast and closure pour. This observation is significant and

shows that nonlinear behavior in the pull-out test is only due to tensile cracking of concrete and failure of the upper interface. As a contrast to the FE result when bond-slip is used, Figure 89 shows one of the earlier attempts when bond-slip was ignored and perfect bond was assumed between the headed bars and the concrete. As it can be seen from Figure 89, use of perfect bond does not fully engage the head of the upper bar. That is, for the same total force, it results in a smaller force in the upper bar's head.

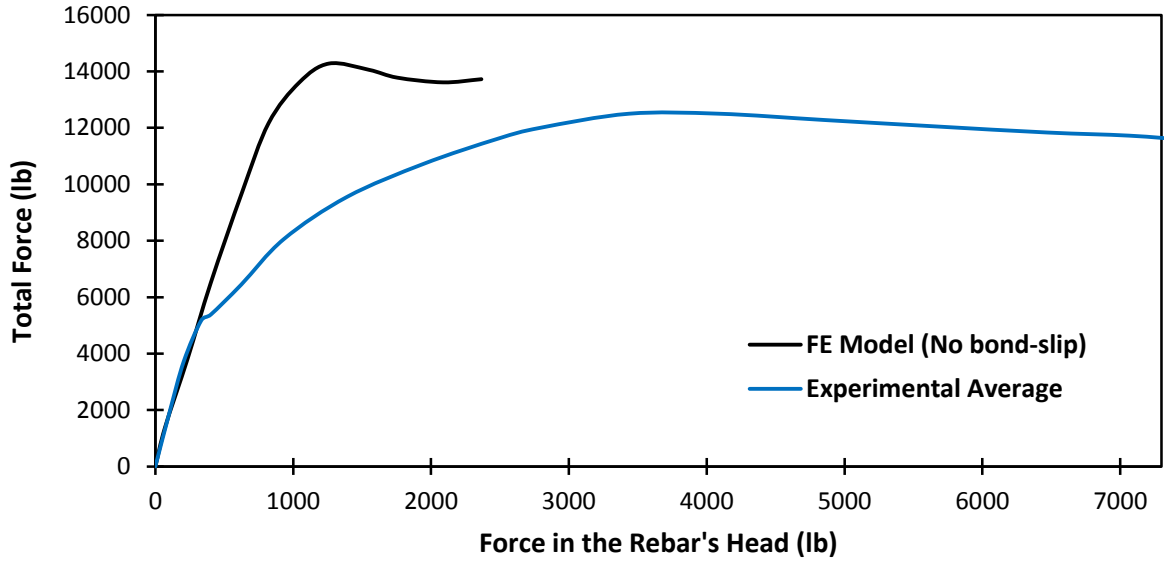

Figure 89. Total force in the pull-out specimen vs. force in the rebar's head (no bond-slip).

Two FE crack plots are shown in Figures 90 and 91 for loadings of 3,300 lb and 9,500 lb, respectively. It should be noted that the orientations of the figures are mirror images of those shown in Figures 84 and 85. A study of the crack plots shows that, the crack plots are in agreement with the experimental observations. It can be seen from Figures 90 and 91 that cracks started from the top of the specimen near the bar and continued to propagate downward. When the crack reaches the interface, the interface fails quickly, and the previous crack again continues to propagate down towards the head. In the crack plots, the red circles represent primary cracks, while the green and blue circles denote the secondary and tertiary cracks respectively. The yellow area at the interface zone denotes the failure of the interface in that region. From the figures, it is observed that the interface crack propagation is similar and in line with the experimental observation.

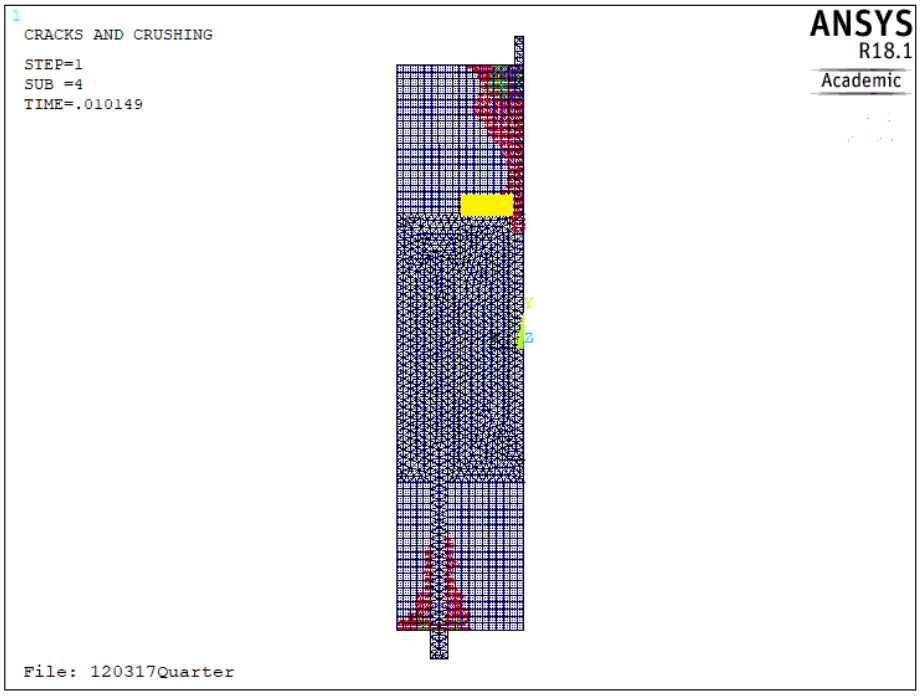

Note: Cracks at substep 4. Crack propagating from the top and the interface is failing.

Figure 90. Crack propagation in the FE model of pull-out test at force = 3,300 lb.

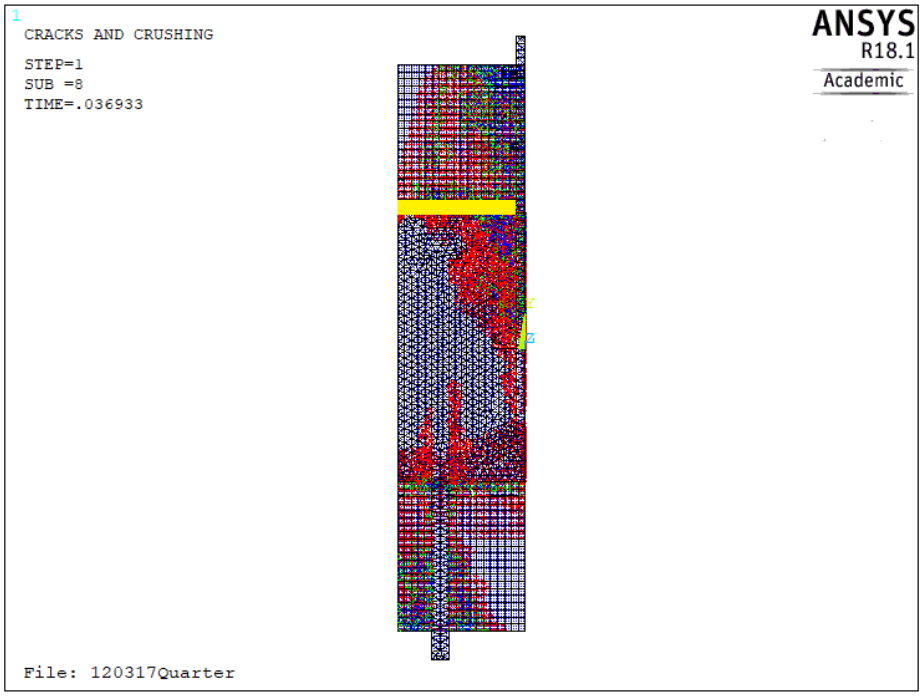

Note: Cracks at substep 8: The interface failed and the initial crack propagating further down.

Figure 91. Crack propagation in the FE model of pull-out test at force = 9,500 lb.

Finite Element Modeling of Beam Bending Tests

The final task of this study is to develop a finite element model of three-point and four-point beam bending tests. A number of approaches were taken to model the beams. Implementing the same modeling techniques from the previous section in the modeling of the beams proved to be problematic. Some new techniques were introduced to resolve these problems, but the models were still based on using springs to simulate bond-slip and CZM to model interface failure.

As described in Chapters 2 and 3, a total six beams were tested for bending. Each beam had a span of 72 inches between the supports, and were 12 inches in width and 8 inches in height. The closure pour section was 10 inches long with shear keys on both sides. A total of four No. 5 headed bars, two from each side, created a lap splice inside the closure at the bottom. Regular No. 5 reinforcing bars were used in a similar fashion at the top. Figure 92 shows the different parts of the 3D model used for the FE analyses.

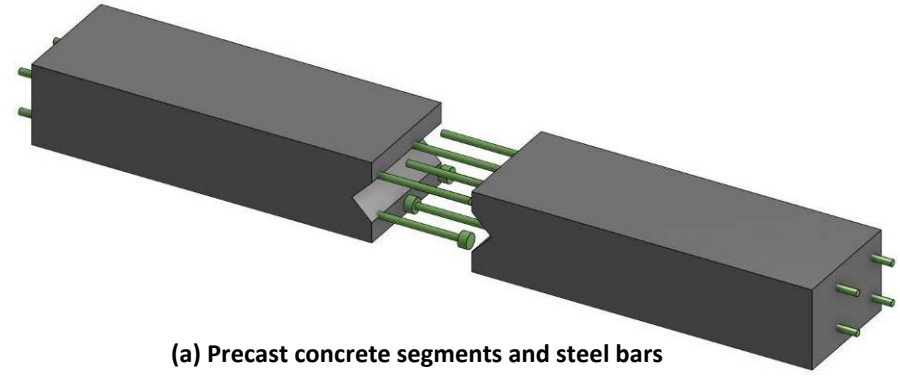

(a) Precast concrete segments and steel bars

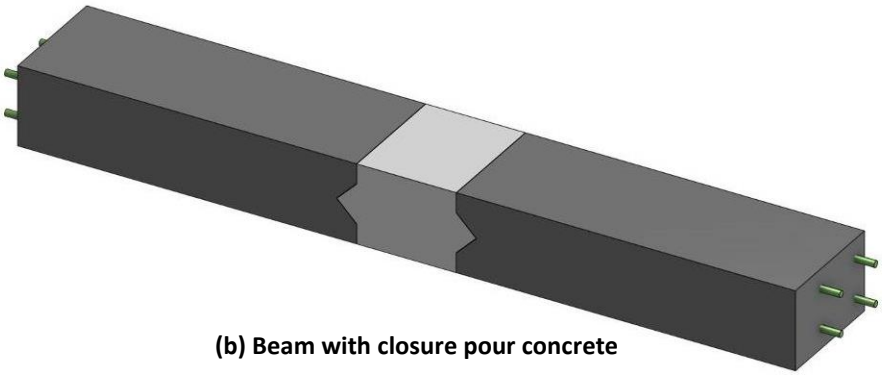

(b) Beam with closure pour concrete

Figure 92. Different components of the beam 3D model.

Three of the beams were tested in three-point bending, and the rest three in four-point bending. For three-point bending, the point load was applied on a 1-in. thick steel plate of a dimension of 20 in. x 10 in. on the top of the beam. This was done to simulate a truck wheel load more realistically. The same as the FE model of the pull-out tests, several models were considered for the beam tests. For details, see the thesis by Rashique, U. (2018).[30] For brevity, here only the final model of the three-point bending beam is presented.

In the beam model, COMBIN39 elements were used again to simulate bond-slip. The spring elements were only applied to the bottom bars. As the top portion of the beam is in compression, the upper bars do not take much load. So their bond-slip was not considered significant and perfect bonding was assumed. The surfaces of the bottom rebars and the surfaces of the voids in concrete that encase the rebars were carefully meshed first so that coincidental nodes could be created between the rebars and the surrounding concrete. A 0.25 in. thick layer of concrete surrounding each bottom bar was given a linear elastic material property. Use of SOLID65 (CONCRETE65) created convergence problems. Therefore, this time, for the rest of the concrete parts, "yielding" in tension and compression were defined using the Cast Iron material model. The linear elastic regions were created to reduce the nonlinearity in the model. Previous attempts using the spring elements but no linear elastic region failed to converge. The reason is that, the force in transferred from rebar to adjacent concrete, the concrete reaches its strength at some point and fails. The combined action of nonlinear springs and failure of concrete at one of the nodes of the spring elements suddenly introduces a large amount of nonlinearities in the model. As the beam model is significantly larger than the pull-out model, this sudden influx of nonlinearities creates convergence problems in the beam model. As the springs were connected to linear elastic elements, there was no need to adjust the force-displacement curve for the springs. The springs were only allowed to move in the direction of the length of the beam. They had no DOF in the other two directions. But this was a bending test. So if "Large Deflection" was turned on in the ANSYS solution options, it would take the bent shape of the beam into account in each substep. In that case, the displacement of the springs in the other two directions would become significant and the assumptions for the spring elements would have become invalid. To avoid this complication, "Large Deflection" option was turned off. CZM was used to model interface failure in tension. The debonding tensile strength was reduced to 256 psi to make it consistent with the pull-out model.

Stresses at two points of the first bottom rebar on the right side were monitored. One of the two points was close to the head, and the other point was right at the interface of precast and closure pour (recall that in the experiments, only the bars next to the head were instrumented with strain gages). As shown in Figure 93, the stresses at these two locations were plotted against the moment at the mid-span of the beam. The stress on the bar close to the head closely matches the experimental results in the linear region up to a moment of about 110 kip-in. The match becomes not as good in the nonlinear region and the bar's stress does not increase in the same way as the experimental results. Compared to the stress next to the bar's head, the FE results at the interface shows larger stress for the same bending moment. This is possibly due to cracks appearing at the right interface, thus allowing the rebar at the interface being pulled away more than around the head. In Figure 93, the point of average cracking moment at the interface is noted. See also Table 14 in Chapter 4. After this point, the stress in the bar at the interface increases much more with increasing bending moment than the stress near the head.

In the experimental phase, all six specimens cracked at the right-hand side closure to precast interface. Looking at the crack propagation in the finite element model of Figure 94, the right-hand side interface opens up more. So the FE model is in good agreement with the experimental results. The reason why the right-hand side interface cracked every time can be explained by the asymmetric splice configuration of the rebars. It should also be noted that the maximum compressive stress observed in

the concrete in the FE model was approximately 3,700 psi, which is less than the compressive strengths of both precast and closure pour. In addition, the larger compressive stresses were directly below the location of applied force from the machine.

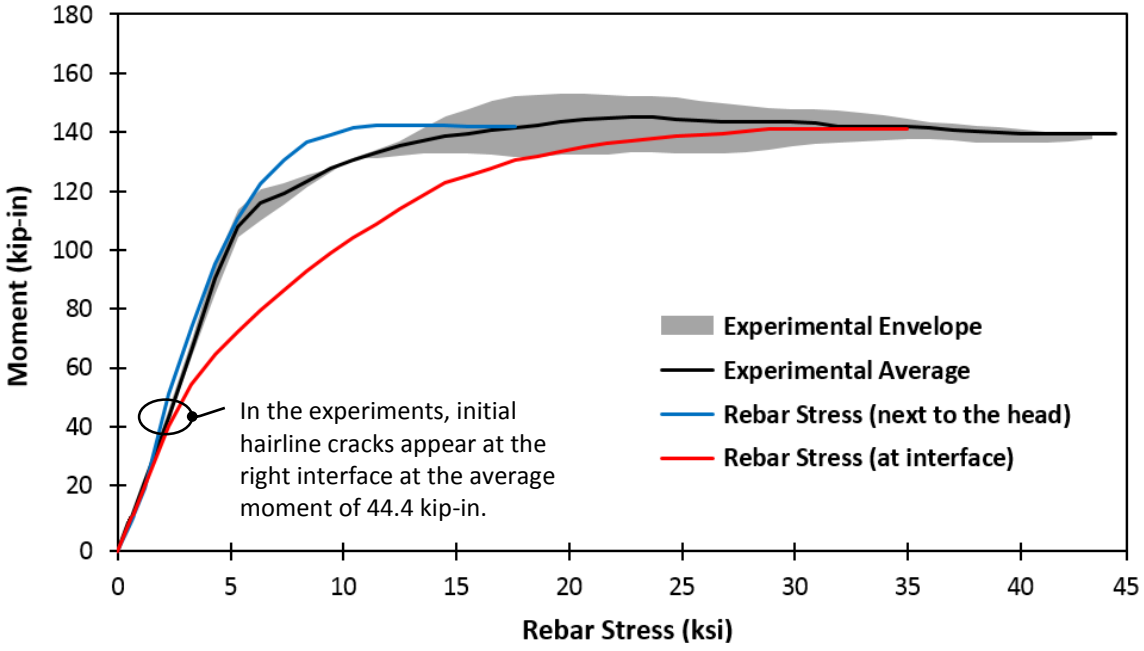

Figure 93. Moment vs. rebar stress for the three-point bending test.

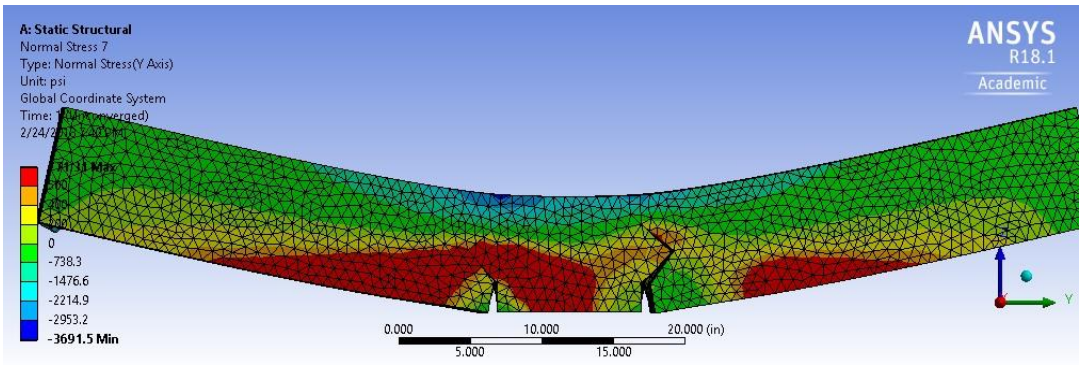

Figure 94. Exaggerated deformed view showing interface crack in three-point bending test.

Discussion on Finite Element Modeling Results

The FE model of the pull-out test specimen and the beam performed well in the linear region and resulted in very good agreements with the experimental results. The agreement in the nonlinear portion was not as good with the beam bending test. Although not measured in the experiments, the FE model of the beam showed a larger bar stress at the interface compared to the bar stress next to the head.

There were more issues with convergence of the beam models compared to the pull-out models. Use of contact elements is another reason for the convergence problems. Contact elements increase the node and element count in an analysis. Moreover, the contact elements themselves have highly nonlinear formulation. In comparison, gluing volumes (which merges the coincidental nodes in adjacent volumes) led to better convergence performance. However, gluing volumes results in perfect bonding and does not allow for bond-slip response. With no bond-slip, the head carries less force in the FE model than what was observed in the experiments. This is true for both the pull-out test and the beam bending test.

More work needs to be done on refining the FE model of the beam bending test to improve the response in the nonlinear region for better match with the experimental results.

Chapter 6
Bridge Modeling and AASHTO LRFD Design Requirements

Introduction

In this chapter a bridge with Deck Bulb-T girders is modeled in ANSYS. Using the optimum mix containing high-early strength concrete with Polypropylene fibers (Mix D), the behavior of the closure pour connections between precast girders is examined under the AASHTO LRFD design requirements for three limit states (AASHTO, 2017).[63] These limit states are: (1) Strength I Limit State for flexural capacity; (2) Service I Limit State for controlling flexural cracking; and (3) Fatigue I Limit State for infinite load-induced fatigue life.

Bridge Description and Assumptions

One span of the new design of SH-36 Bridge over Bear River is considered for analysis under the AASHTO design truck and the AASHTO fatigue design truck. This is a two-lane bridge located in Southeast Idaho near the city of Preston. Figure 95 shows the elevation view of the bridge. Figure 96 shows two girder cross-sections with longitudinal and transverse reinforcing bars. One span of this bridge was modeled with the assumption of it being simply-supported. This assumption is conservative knowing that supports allow for some moment reactions. Assuming that the closure pour connections experience loads exerted by the AASHTO design truck, a linear-elastic analysis was performed in ANSYS. As it will be seen later, under the appropriate load combinations and load factors, the steel and concrete stresses are well within the linear range. To determine the longitudinal and transverse deformation of the span, which will affect the closure pour connection behavior, an effective modulus of concrete equal to $E_{eff.} = 5.79 \times 10^6$ psi is used for the deck concrete and the rest of the girder. This effective value is determined using the ITD structural drawing material properties for concrete and steel and was based on the transverse steel in the 8-in. section of the deck (i.e., #6 bars @ 8”). Longitudinally, the deck bars are spaced @ 4.5”. Although longitudinally the effective modulus results in a slightly larger value, conservatively the same effective transverse modulus was used everywhere. Concrete Poisson’s ratio of 0.2 was assumed.

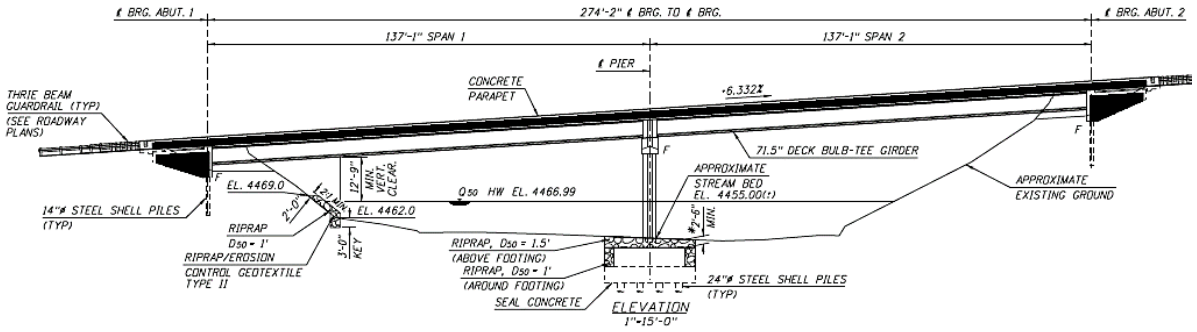

Figure 95. Elevation view of the new design of the SH-36 Bridge over Bear River (NTS).

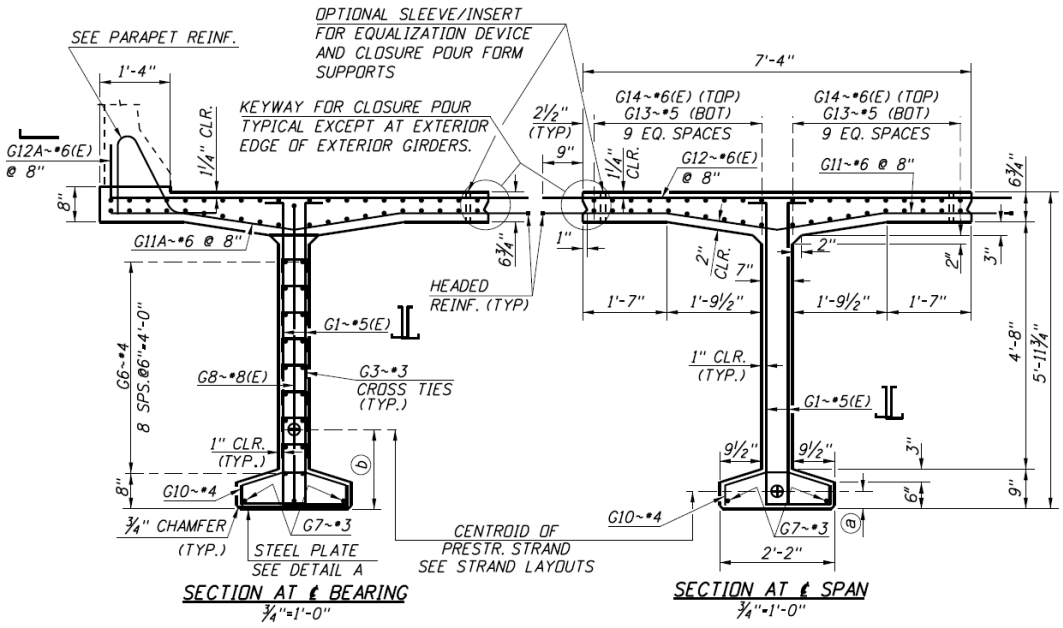

Figure 96. Girder section views of the SH-36 Bridge over Bear River (NTS).

Note that in this bridge #6 bars are used at 8” on center, while in the laboratory experiments #5 bars were placed at 6” on center. Therefore, both cases have approximately the same amount of transverse steel.

Loading and FE Modeling

As shown in Figure 97, one set of truck wheels were placed on top of a closure pour under two types of AASHTO trucks: design truck (three axles), and fatigue design truck (five axles). Using classical influence line approach, both the three-axle and the five-axle trucks were placed longitudinally on the span to create the largest bending moment. This placement for the AASHTO design truck (three-axle) is shown in Figure 98. Here the lead axle is 54’ from the end of the span.

In ANSYS the bridge span was modeled using 12 in. x 12 in. shell elements for the deck and the girders were modeled using beam elements. As seen in Figure 98, for the AASHTO design truck, the deck moments and stresses are found in two shell elements with one 16-kip load distributed over them. The remaining loads were treated as concentrated forces. Therefore, the patch area is 24”x12”. The moment values along the centerline of closure pour are determined. Note that the patch area is larger than 10”x20” used by AASHTO, but the moment and stress values at the center of closure pour (forming the boundary between the two 12”x12” shell elements) were found which are larger than at the values at the closure pour interface. The alternative would have been to use a much finer mesh for the deck.

Similar placement of the truck was considered for the fatigue truck. As shown in Figure 99, for the fatigue truck, two 8-kip pressures patches (shown in the ellipse in the figure) were used, each occupying two 12”x12” shell elements. Again, the moment and stresses at the center of the closure pour were

determined. Figures 100 and 101 show the bridge span model in ANSYS. From Figure 101, it can be seen that for better accuracy, shell elements with different thicknesses were used.

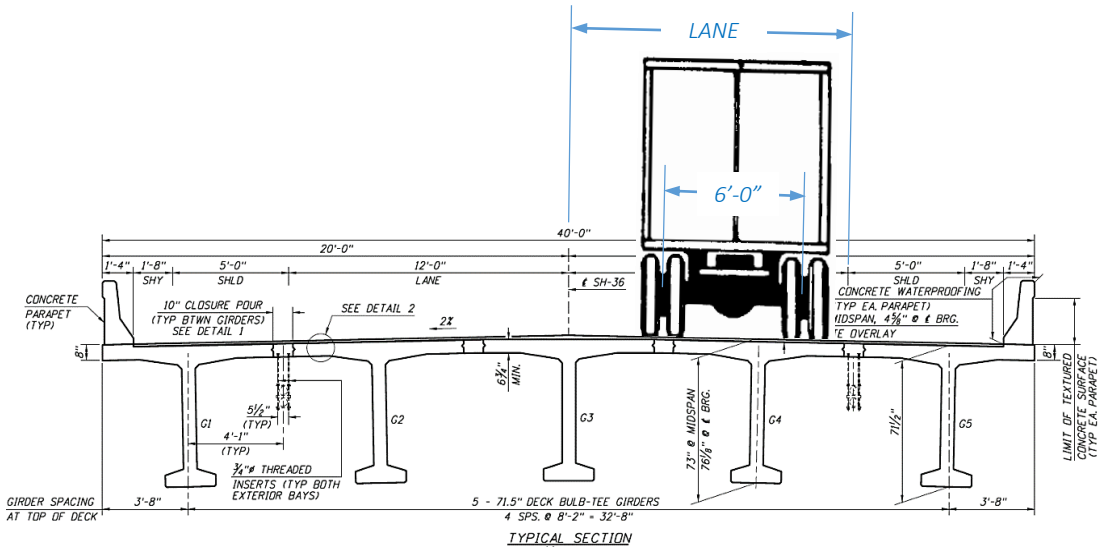

Figure 97. Section view of the bridge with truck in one lane (NTS).

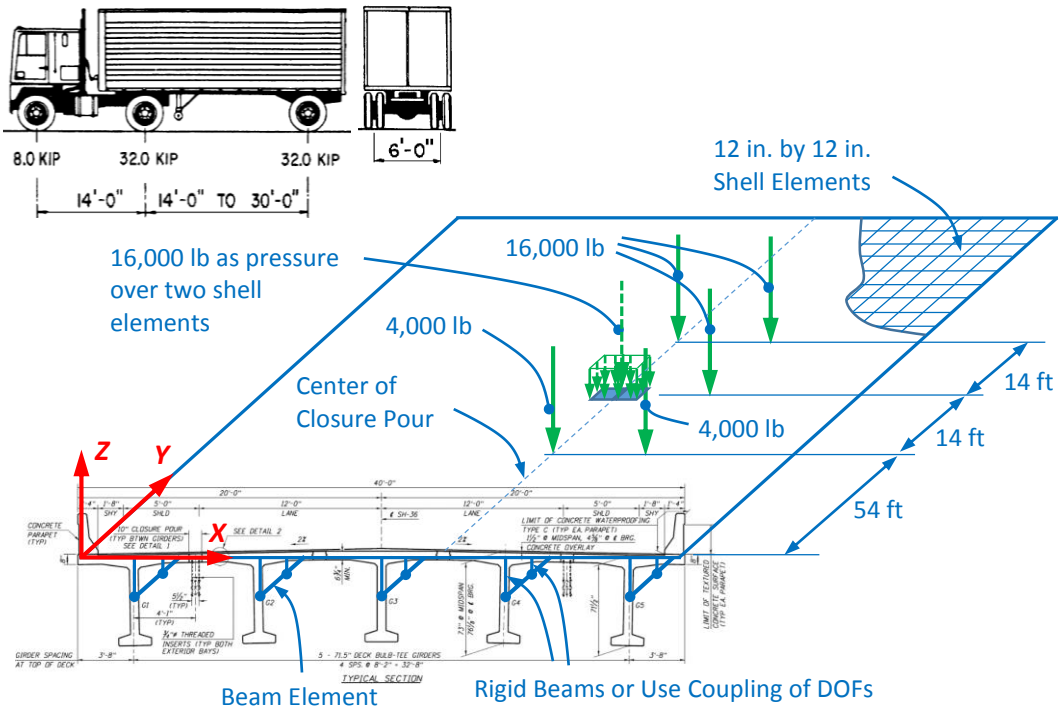

Figure 98. Section view of the bridge with AASHTO design truck in one lane (NTS).

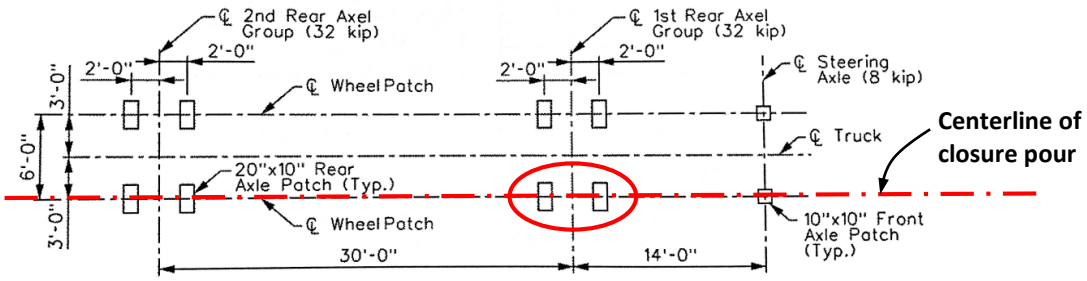

Figure 99. AASHTO fatigue truck with pressure placed on the patches that are circled.

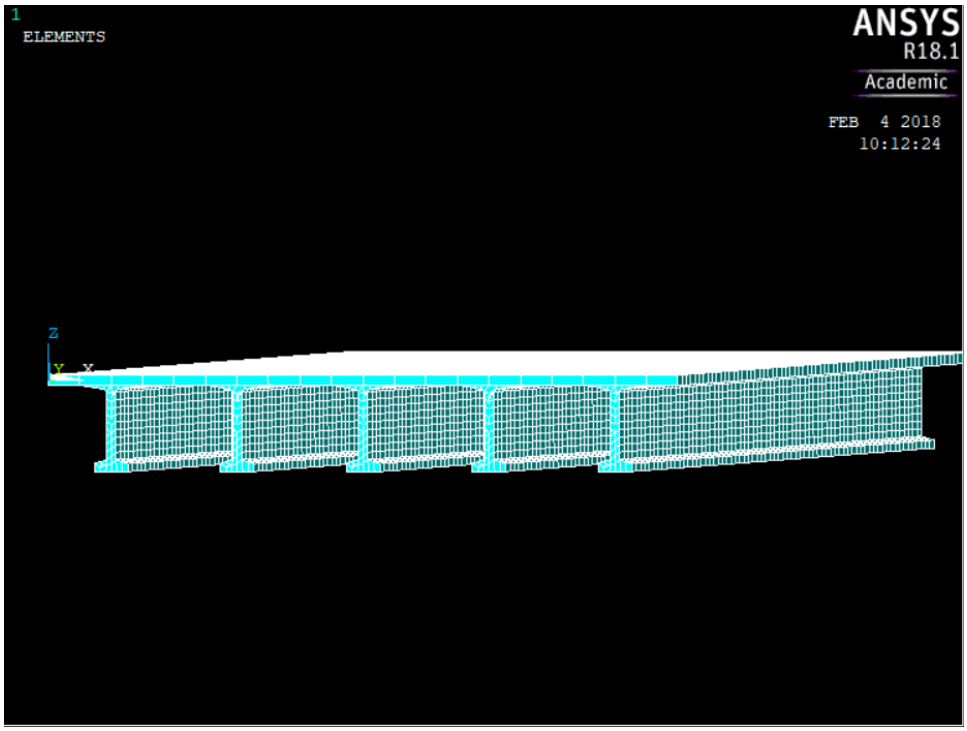

Figure 100. 3-D view of the bridge in ANSYS showing girder beam elements and deck shell elements.

Initially, for transportation purposes, the girder deck will have approximately 1.5 in. less thickness than the final thickness. Once the girders are placed, a 1.5-in. concrete overlay will be placed on the deck as well as the future wearing surface. The added weight of these dead loads are 18.75 psf and 28 psf, respectively. For analysis, the AASHTO design truck live load will be increased by 33% to account for live load impact. The live load due to AASHTO fatigue truck will be increased by 15%.

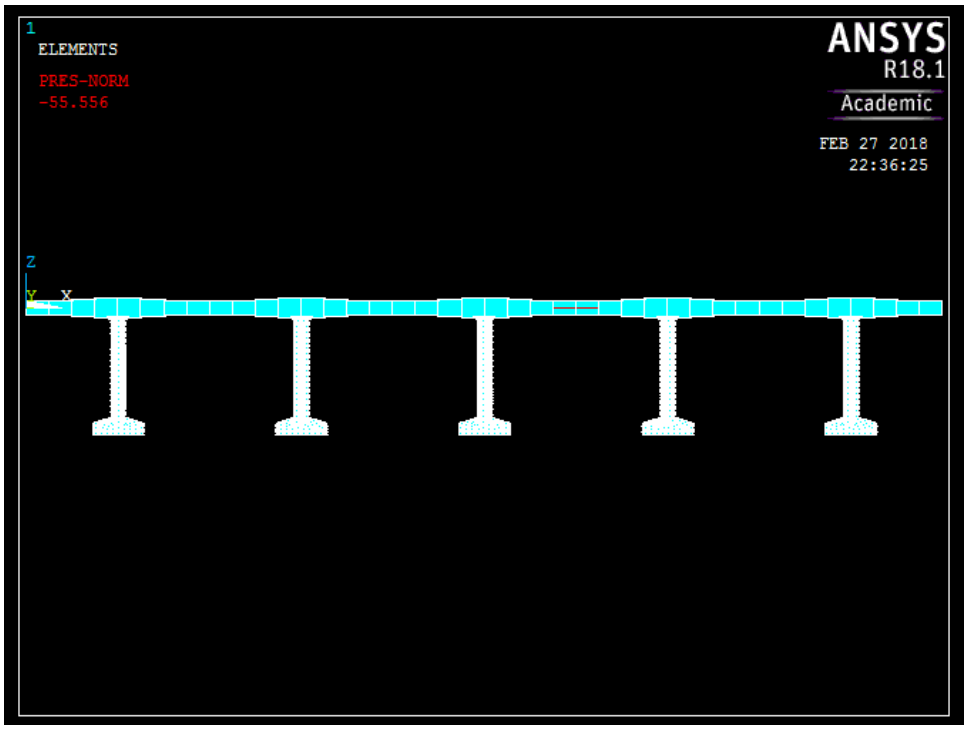

Figure 101. Section view of the bridge in ANSYS.

Results under Added Dead Loads

Figure 102 shows two side-by-side shell elements and the bending moments under dead loads of 1.5" concrete overlay (18.75 psf) and future wearing surface of 28 psf. Tables 15 shows the values of nodal forces and moments in global coordinates. Table 16 shows the values of element stresses in global coordinates. The values used in the analysis are highlighted in yellow.

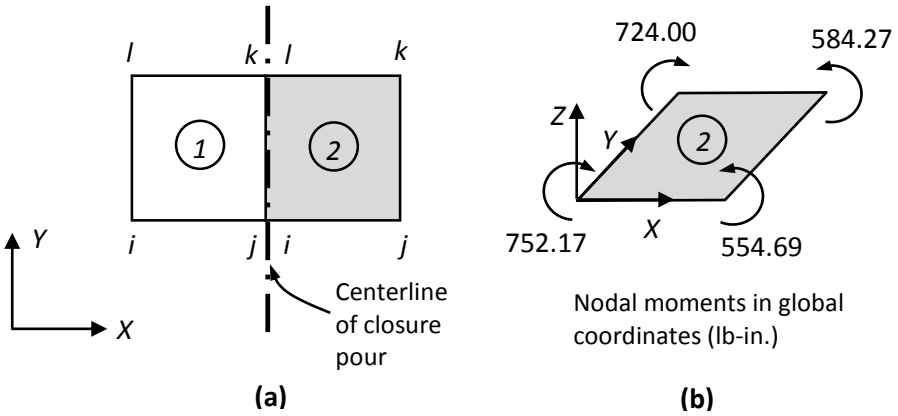

Figure 102. Deck shell elements under added dead loads.

Table 15. Nodal forces and moments in global coordinates (lb and lb-in.) under added dead loads.

Element	Node	FX	FY	FZ	MX	MY	Mz
1955	*2751*	-10.903	-10949	1.8248	3708.2	-752.17	0.10340E-1
1955	*2890*	5.6188	-10944	-26.148	3680.4	554.69	-0.15779
1955	*2891*	10.873	10949	-25.327	-3714.3	584.27	-0.17230
1955	*2752*	-5.5888	10944	2.9007	-3685.7	-724.00	-0.16376E-1

Table 16. Element stresses in global coordinates (psi) under added dead loads.

Element	Node	SX	SY	SZ	SXY	SYZ	SXZ
1955, top	*2751*	-10.387	-285.82	0	-0.28119	0	0
1955, top	*2890*	-10.387	-285.82	0	-0.28119	0	0
1955, top	*2891*	-10.387	-285.82	0	-0.28119	0	0
1955, top	*2752*	-10.387	-285.82	0	-0.28119	0	0
1955, bottom	*2751*	10.044	-170.28	0	0.17082	0	0
1955, bottom	*2890*	10.044	-170.28	0	0.17082	0	0
1955, bottom	*2891*	10.044	-170.28	0	0.17082	0	0
1955, bottom	*2752*	10.044	-170.28	0	0.17082	0	0

From the above tables, the maximum moment and the maximum bending (normal) stress values under the added dead loads are as follows:

$M_{max} = 0.752 + 0.724 = 1.48$ kip-in.

Max. bending stress at the bottom $(\sigma_x)_{max} = 10.0$ psi

Results under AASHTO Design Truck Load

Next, the moments and bending stresses are calculated under AASHTO design truck placed as shown in Figure 98. The values on the same two shell elements, shown in Figure 102(a), are given in Tables 17 and 18. Again, as noted previously, a pressure load caused by a 16-kip force is placed on the two shell elements, while other loads are treated as point loads. From the tables, the maximum moment and the maximum bending (normal) stress values are:

$M_{max} = 26.29 + 26.47 = 52.76$ kip-in.

Max. bending stress at the bottom $(\sigma_x)_{max} = 364.6$ psi

Table 17. Nodal forces and moments in global coordinates (lb and lb-in.) under AASHTO design truck.

Element	Node	FX	FY	FZ	MX	MY	Mz
1955	*2751*	-142.37	-6951.7	-1474.4	14808	-26287	-1.0586
1955	*2890*	-373.45	-6439.7	-2541.1	14662	20057	-1.5290
1955	*2891*	142.26	6955.8	-2525.5	-14583	19900	-0.35350
1955	*2752*	373.56	6435.6	-1459.0	-15072	-26469	0.15170

Table 18. Element stresses in global coordinates (psi) under AASHTO design truck.

Element	Node	SX	SY	SZ	SXY	SYZ	SXZ
1955, top	*2751*	-359.75	-370.45	0	-4.0395	0	0
1955, top	*2890*	-359.75	-370.45	0	-4.0395	0	0
1955, top	*2891*	-359.75	-370.45	0	-4.0395	0	0
1955, top	*2752*	-359.75	-370.45	0	-4.0395	0	0
1955, bottom	*2751*	364.57	91.466	0	-6.7092	0	0
1955, bottom	*2890*	364.57	91.466	0	-6.7092	0	0
1955, bottom	*2891*	364.57	91.466	0	-6.7092	0	0
1955, bottom	*2752*	364.57	91.466	0	-6.7092	0	0

Results under AASHTO Fatigue Truck Load

The results under AASHTO fatigue truck placed as shown in Figure 99 are shown in Tables 19 and 20. The patch that resulted in larger values was used. This patch is located on the left side within the ellipse shown in Figure 99. The two 8-kip loads on the patches within the ellipse were placed as pressure, while other loads were placed as point loads. Two 12”x 12” side-by-side shell elements as shown in Figure 102(a), were used for each patch. From the tables, the maximum moment and the maximum bending (normal) stress values are:

$M_{max} = 17.79 + 18.46 = 36.24$ kip-in.

Max. bending stress at the bottom $(\sigma_x)_{max} = 259.5$ psi

Table 19. Nodal forces and moments in global coordinates (lb and lb-in.) under AASHTO fatigue truck.

Element	Node	FX	FY	FZ	MX	MY	Mz
1943	*2748*	-299.10	-6238.6	-700.47	8271.8	-17785	-0.45210
1943	*2887*	-405.02	-55382	-1240.9	8893.5	15374	0.11313
1943	*2888*	298.94	6242.2	-1288.1	-7784.2	14522	1.1558
1943	*2749*	405.18	5534.6	-770.89	-8675.6	-18457	0.63583

Table 20. Element stresses in global coordinates (psi) under AASHTO fatigue truck.

Element	Node	SX	SY	SZ	SXY	SYZ	SXZ
1943, top	*2748*	-257.25	-254.02	0	-1.1268	0	0
1943, top	*2887*	-257.25	-254.02	0	-1.1268	0	0
1943, top	*2888*	-257.25	-254.02	0	-1.1268	0	0
1943, top	*2749*	-257.25	-254.02	0	-1.1268	0	0
1943, bottom	*2748*	259.46	8.6728	0	-13.541	0	0
1943, bottom	*2887*	259.46	8.6728	0	-13.541	0	0
1943, bottom	*2888*	259.46	8.6728	0	-13.541	0	0
1943, bottom	*2749*	259.46	8.6728	0	-13.541	0	0

Applicable AASHTO Limit States

The following load combinations were considered:

Strength I Limit State for flexural capacity:

$$1.5\ DW\ + 1.75\ LL\ (1 + IM)$$

Where, DW = dead load due to concrete overlay wearing surface; LL = live load (AASHTO design truck); and IM = impact factor = 0.33.

Service I Limit State for controlling flexural cracking:

$$1.0\ DW\ +\ 1.0\ LL\ (1 + IM)$$

Where, IM = 0.33.

Fatigue I Limit State for infinite load-induced fatigue life:

$$1.5\ LL\ (1 + IM)$$

Where, LL = live load due to AASHTO fatigue truck, IM = 0.15.

Strength I Limit State for Flexural Capacity

The ultimate moment in the bridge deck imposed by the dead load and AASHTO design truck live load for a one-foot width FE shell element is:

$$M_u = 1.5(1.48) + 1.75(52.76)(1 + 0.33) = 125.0 \text{ kip-in.}$$

The reduced moment capacity based on experimental results under three-point bending with the same one-foot width (i.e., using value of 147.1 kip-in. from Table 14) is:

$$\phi M_n = 0.9(147.1) = 132.4 \text{ kip-in.} > M_u \quad \underline{\textbf{O.K.}}$$

Note that in a bridge there are longitudinal bars at each closure pour at the top and bottom. This, plus the two-way action of the bridge deck will help in increasing the moment capacity. Therefore, in an actual bridge, the value of nominal bending moment capacity, M_n, is probably larger than 147 kip-in. per foot of the closure pour connection.

Service I Limit State for Controlling Flexural Cracking

Recall from the laboratory experiments on interface bond strength between closure pour (Mix D) and precast concrete using the ASTM C78 (see Table 10 in Chapter 4), a modulus of rupture f_r = 612 psi was obtained.

From the FE analysis, the deck maximum concrete bending stress under the added dead load and AASHTO design truck live load is:

$$f_{concrete} = 1.0(10) + 1.0(364.6)(1 + 0.33) = 494.9\, psi < f_r = 612\, psi \quad \underline{\textbf{O.K.}}$$

Note that in the FE model the stresses are obtained at the center of the closure pour which are larger than those at the interface.

Fatigue I Limit State for Infinite Load-induced Fatigue Life

The requirements of the AASHTO LRFD Bridge Design Specs. Article 5.5.3 – Fatigue Limit State are followed in this section.

The maximum moment in the deck under the AASHTO fatigue truck live load is:

$$M_{max} = 1.5(36.25)(1 + 0.15) = 62.5 \text{ kip-in.}$$

From Figure 103 shown below (this is the same figure as Figure 93 from Chapter 5), the stress in the bar at the interface under the beam three-point bending and factored moment of 62.5 kip-in. is approximately equal to 4 ksi.

For the stress range, let's double the effect (very conservative!). This will give:

$$\gamma(\Delta f_s) = 8\, ksi$$

Where, $\gamma(\Delta f_s)$ = factored live load stress <u>range</u> in the steel bar.

The constant-amplitude fatigue threshold, $(\Delta F)_{TH}$, for reinforcement is:

$$(\Delta F)_{TH} = 24 - 0.33 f_{min} \qquad \text{AASHTO Eq. (5.5.3.2-1)}$$

Where, f_{min}= minimum live-load stress resulting from the Fatigue I load combination, combined with the more severe stress from either the permanent loads or the permanent loads, shrinkage, and creep-induced external loads; positive if tension, negative if compression (ksi).

Assume $f_{min} = 0$. Therefore,

$$(\Delta F)_{TH} = 24 \ ksi$$

$$\gamma(\Delta f_s) < (\Delta F)_{TH} \quad \underline{\textbf{O.K.}} \qquad \text{AASHTO Eq. (5.5.3.1-1)}$$

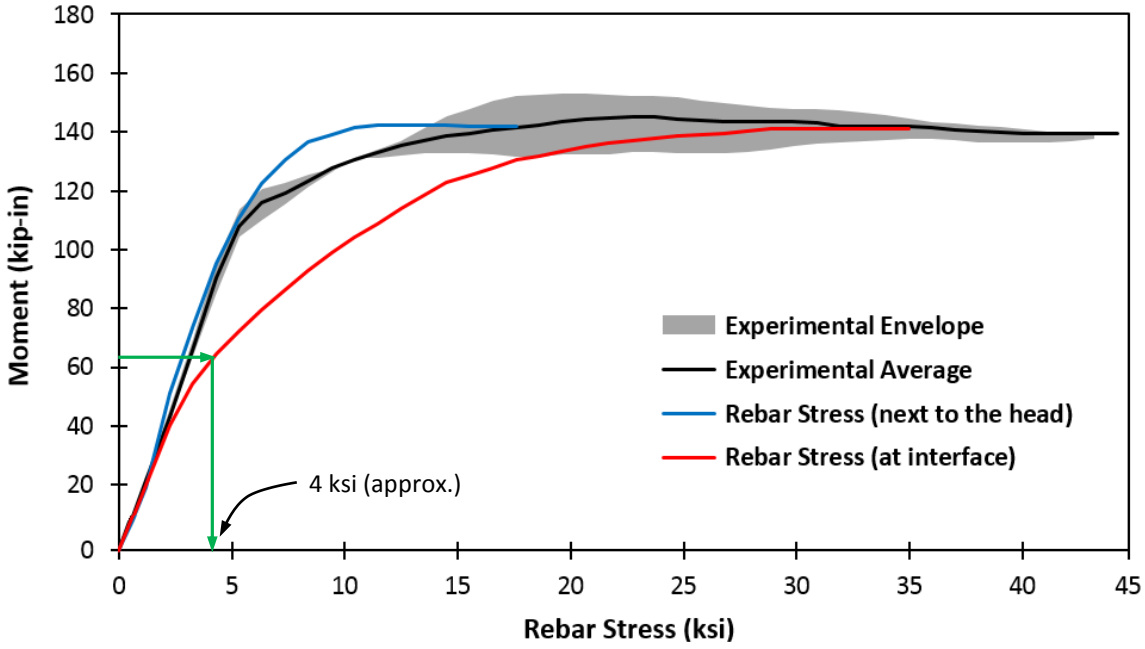

Figure 103. Moment vs. rebar stress for the three-point bending test.

Therefore, according to the requirements of AASHTO LRFD Bridge Design Specs. Article 5.5.3, the closure pour can withstand infinite number of fatigue truck load cycles without headed bar experiencing fatigue failure.

Fatigue analysis requires cracked section properties if "*sum of stresses, due to unfactored permanent loads and prestress, and the Fatigue I load combination is tensile and exceeds* $0.095\sqrt{f_c'}$*.*"

In the case of bridge considered, both the precast and closure pour (Mix D) have almost the same compressive strength of 8.5 ksi $\Rightarrow$ $0.095\sqrt{f_c'} = 0.277$ ksi $= 277$ psi.

The sum of maximum bending stresses in concrete at the bottom of the deck due to unfactored loads is: $10 + 259.5 \cong 270$ psi.

Therefore, the use of uncracked section properties in the bridge model is acceptable.

Chapter 7
Summary, Conclusions, and Future Work

The objectives of this research project were to (a) obtain experimental data on the behavior of several mixes containing HES concrete Class 50AF with and without polypropylene fibers and select the optimum mix for use as a closure pour material between Deck Bulb-T Girders; and (b) use the experimental results to create a computer model of the proposed closure pour detail and provide an indication of fatigue performance under repeated loading. To accomplish these objectives, five main tasks were performed. In the following paragraphs, summary and conclusions are provided for each task. At the end, the future work that is directly related to this project is briefly noted.

Summary and Conclusions of the Tasks Performed

Task 1

This task was to perform a literature review. Five main sections were covered: (a) an overview of the field-cast connections of prefabricated bridge elements; (b) related testing methods; (c) preparation of laboratory concrete specimens; (d) materials needed for the closure pour, including bonding agent and polypropylene fibers; and (e) literature needed for computer modeling. Literature review revealed that high performance fiber-reinforced concrete has been used as an alternate material to UHPC in connecting certain bridge precast components. Work by others gave insight as to the appropriate ASTM testing methods and sample preparation techniques. It was also concluded that rebar bond-slip plays an important role in numerical modeling.

Task 2

Task 2 was to select HES concrete mixes with and without polypropylene fibers and other additives. This task was done with direct input from the TAC members. Six mixes were selected. Compressive strength, tensile strength, and shrinkage behavior of each mix were determined. Mix D, containing 1.5 lb/yd^3 of fiber and shrinkage reducing admixture, performed the best. It had the largest compressive and tensile strength values and the lowest shrinkage value. These values were 8,864 psi, 837 psi, and 522 microstrain, respectively. For computer modeling, modulus of elasticity and Poisson's ratio of the optimum mix were also obtained.

Task 3

Task 3 was to obtain the interface bond strength and perform headed bar pull-out tests. With input from TAC, Mixes D and E with and without bonding agent were selected for the ASTM C78 four-point bending tests. Mix E contained 0.75 lb/yd^3 of fiber, shrinkage reducing admixture, and bonding admixture. Mix D without the bonding agent performed the best with bond strength (modulus of rupture) value of 612 psi. In contrast, De la Varga, Haber, and Graybeal (2016) obtained a value of 712

psi for the interface bond strength between UHPC and precast concrete with exposed aggregate surface.[1]

Next, headed bar tensile strength tests were performed in a closure pour connection with the optimum mix. The specimen represents the lower half portion of a closure pour section. Six headed bar pull-out specimens were tested. The primary mode of failure in all headed bar pull-out tests was cracking of the concrete. No surface spalling was observed at any point during the tests. Cracking initiated at the top interface and propagated horizontally across the sample. Then, the bottom interface began to show formation of cracks. After reaching the ultimate load, there was a sudden drop in load and the specimen cracked along the center rebar and down into the lower precast concrete section. Conical cracks also developed at the location of the center rebar head. The average ultimate pull-out force was 12,511 lb. Even after the failure of the upper interface, the strut action between the opposing lapped bars was effective, resulting in upper bar stress of 40.4 ksi or 67% of the steel specified yield strength. The most useful data was the relationship between total tensile force in the specimen and the force carried by the head of the upper bars. This relationship was used to calibrate the FE model of the pull-out specimen.

Task 4

Task 4 was to perform three-point and four-point flexural tests of beams composed of two precast segments with the optimum mix closure pour segment in the middle. ITD's 10-in. closure pour detail was used. Three of each beam tests were performed. In both cases of three-point bending and four-point bending, the initial crack always formed on the lower right of the interface between closure pour and precast. This was a limitation of the beam specimens; i.e., unsymmetrical placement of reinforcing and the small width of the beam. Both the three-point and four-point loading tests had almost the same ultimate moment capacity of about 147 kip-in. The mid-span moment versus the stress next to the head of the headed bars (where the strain gages were installed) provided the most useful information. This data was used for comparing results with the FE model results.

Task 5

This task had two components. The first one was to develop the FE models for headed bar pull-out and the beam specimens and compare the results with the experimental test results. In addition, the task required investigation of the adequacy of the connection with the optimum mix between the Deck Bulb-T girders of a typical bridge.

The FE models of the pull-out and beam specimens performed well in the linear region and resulted in very good agreements with the experimental results of moment versus stress in the bar next to the head. The agreement in the nonlinear region was not as good with the beam bending tests. Although not measured in the experiments, the FE model of the beam showed a larger bar stress at the interface compared to the bar stress next to the head. Rebar bond-slip had a big role in capturing the experimental results. With no bond-slip, the head carries less force in the FE model than what was observed in the experiments. This was true for both the pull-out test and the beam bending test. More

work needs to be done in refining the FE model of the beam bending test to improve the response in the nonlinear region.

Next, a bridge with Deck Bulb-T girders connected with Mix D was modeled in ANSYS. This bridge is the new design of the SH-36 Bridge over Bear River near Preston, Idaho. For this task linear-elastic behavior was considered. The closure pour connection performed well under three AASHTO limit states: (1) Strength I Limit State for flexural capacity; (2) Service I Limit State for controlling flexural cracking; and (3) Fatigue I Limit State for infinite load-induced fatigue life.

Future Work

The second phase of this project has been approved. This phase involves instrumenting the SH-36 Bridge over Bear River with strain gages placed over the headed bars and on the concrete surface below the bridge deck along a transverse section close to the southwest abutment. Early in 2018, the bridge girders were fabricated. They will be installed during the summer and early fall 2018. In May 2018, the bridge girder headed bars were instrumented in the precasting yard. Based on the results of the first phase, headed bars have been instrumented next to the head and next to the precast interface. The closure pour material for this bridge is a mix similar to the optimum mix found in the laboratory. Among the tasks planned are: strain data measurement in the bridge under a known truck load, data acquisition under commercial truck loading, data analysis, and refining the FE model of ITD's 10-in. closure pour detail.

References

1. **De la Varga, I., J. B. Haber, and B. A. Graybeal.** "Performance of Grouted Connections for Prefabricated Bridge Elements-Part I: Material-Level Investigation on Shrinkage and Bond." *PCI National Bridge Conference*. Nashville, TN, 2016.

2. **Haber, J. B., I. De la Varga, and B. A. Graybeal.** "Performance of Grouted Connections for Prefabricated Bridge Elements-Part II: Component-Level Investigation on Bond and Cracking." *PCI National Bridge Conference*. Nashville, TN, 2016.

3. **Graybeal, B. A.** *Design and Construction of Field-Cast UHPC Connections*, Washington, D.C.: Federal Highway Administration, Report No. FHWA-HRT-14-084, 2014.

4. **De la Varga, I., and B. A. Graybeal.** *Dimensional Stability of Grout-Type Materials Used as Connections for Prefabricated Bridge Elements*, Washington, D.C.: Federal Highway Administration, Report No. FHWA-HRT-16-008, 2016.

5. **Graybeal, B. A.** *Field-Cast UHPC Connections for Modular Bridge Deck Elements*, Washington, D.C.: Federal Highway Administration, Report No. FHWA-HRT-11-022, 2010.

6. **Haber, J. B., and B. A. Graybeal.** "Performance of Multiple UHPC-Class Materials in Prefabricated Bridge Deck Connections." In *First International Interactive Symposium on UHPC*. Des Moines, IA, 2016.

7. **Hoomes, L. C., H. C. Ozyildirim, and M. Brown.** *Evaluation of High-Performance Fiber-Reinforced Concrete for Bridge Deck Connections, Closure Pours, and Joints*, Charlottesville, VA: Virginia Transportation Research Council, Report No. VTRC 17-R15, 2017.

8. **Mamlouk, M. S., and J. P. Zaniewski.** *Materials for Civil and Construction Engineers*. 3rd ed. Prentice Hall, Upper Saddle River, NJ, 2011.

9. **ASTM International**. *Standard Test Method for Length Change of Hardened Hydraulic-Cement Mortar and Concrete*, West Conshohocken, PA: ASTM C157-17, 2017.

10. **Bentz, D. P., I. De la Varga, J. F. Muñoz, R.P. Spragg, B. A., Graybeal, D. S. Hussey, D. L. Jacobson, S. Z. Jones, and J. M. LaManna.** "Influence of Substrate Moisture State and Roughness on Interface Microstructure and Bond Strength: Slant Shear vs. Pull-off Testing." *Cement and Concrete Composites*, Vol. 87, March 2018: 63-72.

11. **De la Varga, I., J. B. Haber, and B. A. Graybeal.** *Bond of Field-Cast Grouts to Precast Concrete Elements*, Washington, D.C.: Federal Highway Administration, Report No. FHWA-HRT-16, 2017.

12. **Emmons, P. H.** *Concrete Repair and Maintenance Illustrated*. Kingston, MA: R.S. Means Company Inc., 1994.

13. **Silfwerbrand, J.** "Shear Bond Strength in Repaired Concrete Structures." *Materials and Structures* Vol. 36, No. 6 (2003): 419-424.

14. **Swenty, M. K., and B. A. Graybeal.** "Characterization of Materials Used in Field-Cast Precast Concrete Connections." *PCI Journal*, Vol. 62, No. 6 (2017): 33-44, 2017.

15. **Yildirim, G., M. Şahmaran, M. K. M. Al-Emam, R. K. H. Hameed, Y. Al-Najjar, and M. Lachemi.** "Effects of Compressive Strength, Autogenous Shrinkage, and Testing Methods on Bond Behavior of High-Early- Strength Engineered Cementitious Composites." *ACI Materials Journal*, Vol. 112, No. 3 (January 2015): 409-418.

16. **ASTM International**. *Standard Test Method for Splitting Tensile Strength of Cylindrical Concrete Specimens*. West Conshohocken, PA: ASTM C496-17, 2017.

17. **ASTM International**. *Standard Test Method for Bond Strength of Epoxy-Resin Systems Used with Concrete by Slant Shear*. West Conshohocken, PA: ASTM C882-13a, 2013.

18. **ASTM International**. *Standard Test Method for Tensile Strength of Concrete Surfaces and the Bond Strength or Tensile Strength of Concrete Repair and Overlay Materials by Direct Tension (Pull-off Method)*. West Conshohocken, PA: ASTM C1583-13, 2013.

19. **Julio, E. N. B. S., F. A. B. Branco, and V. D. Silva.** "Concrete-to-Concrete Bond Strength: Influence of the Roughness of the Substrate Surface." *Construction and Building Materials* Vol. 18, No. 9 (2004): 675–681.

20. **Santos, P. M. D., and E. N. B. S. Julio,** "Factors Affecting Bond between New and Old Concrete." *ACI Materials Journal*, Vol. 108, No. 4 (2011): 449-456.

21. **Tayeh, B. A., B. H. A. Bakar, and M. A. M. Johari.** "Characterization of the Interfacial Bond between Old Concrete Substrate and Ultra High Performance Fiber Concrete Repair Composite." *Materials and Structures*, Vol. 46, No. 5 (2013): 743–753.

22. **Júlio, E., F. A. B. Branco, and V. D. Silva.** "Concrete-to-Concrete Bond Strength: Influence of an Epoxy-Based Bonding Agent on a Roughened Substrate Surface." *Magazine of Concrete Research*, Vol. 57, No. 8 (2005): 463-468.

23. **ASTM International**. *Standard Specification for Latex Agents for Bonding Fresh to Hardened Concrete*. West Conshohocken, PA: ASTM C1059-13, 2013.

24. **ASTM International**. *Standard Test Method for Bond Strength of Latex Systems Used with Concrete by Slant Shear (Withdrawn 2008)*. West Conshohocken, PA: ASTM C1042-99, 1999.

25. **Ahmed, S., I. A. Bukhari, J. I. Siddiqui, and S. A. Qureshi.** "A Study on Properties of Polypropylene Fiber Reinforced Concrete." *31st Conference on Our World in Concrete & Structures*, Singapore, August 16 – 17, 2006.

26. **Banthia, N., and R. Gupta.** "Influence of Polypropylene Fiber Geometry on Plastic Shrinkage Cracking in Concrete." *Cement and Concrete Research,* Vol. 36, No. 7 (2006): 1263–1267.

27. **Madhavi, T., L. Raju, and D. Mathur.** "Polypropylene Fiber Reinforced Concrete-A Review." *International Journal of Emerging Technology and Advanced Engineering*, Vol. 4, Special Issue 4 (June 2014): 114-119.

28. **Serdar, M., A. Baričević, M. Jelčić Rukavina, M., Pezer, D. Bjegović, and N. Štirmer.** "Shrinkage Behaviour of Fibre Reinforced Concrete with Recycled Tyre Polymer Fibres." *International Journal of Polymer Science*, 2015.

29. **Kakooei, S., H. M. Akil, M. Jamshidi, and J. Rouhi.** "The Effects of Polypropylene Fibers on the Properties of Reinforced Concrete Structures." *Construction and Building Materials*, Vol. 27 (2012): 73–77.

30. **Rashique, U.** "Finite Element Modeling of a Field-cast Connection Composed of High-Early Strength Concrete with Polypropylene Fibers and Headed Bars for Bridge Prefabricated Elements." Master's Thesis, Idaho State University, Pocatello, ID, 2018.

31. **Mathey, R. G., and D. Watstein.** "Investigation of Bond in Beam and Pull-out Specimens with High-Yield-Strength Deformed Bars." *Journal of American Concrete Institute*, Vol. 57, No. 3 (March 1961): 1071-1090.

32. **Lutz, L. A., and P. L. B. Gergely.** "Mechanics of Bond and Slip of Deformed Bars in Concrete." In *Journal of American Concrete Institute*, Vol. 64, No. 11 (November 1967):711–721.

33. **Goto, Y.** "Cracks Formed in Concrete around Deformed Tension Bars." *Journal of American Concrete Institute*, Vol. 68, No. 4 (April 1971): 244–251.

34. **Nilson, A. H.** "Internal Measurement of Bond Slip." *Journal of American Concrete Institute*, Vol. 69, No. 7 (July 1972): 439–441.

35. **Rao, G.A., K. Pandurangan, F. Sultana, and R. L. B. Eligehausen.** "Studies on the Pull-out Strength of Ribbed Bars in High-Strength Concrete." *Proceeding, FraMCos-6 Conference. International Association of Fracture Mechanics for Concrete and Concrete Structures. Part*, 5:5–17, 2007.

36. **Fynboe, C.C., and E. Thorenfeldt.** *T-Headed Bars, SP1: Static Pullout Tests*, Trondheim, Norway: SINTEF Test Report STF65 F86083, 1986.

37. **Eligehausen, R.** "Bericht Über Zugversuche Mit Deha Kopfbolzen (Report on Pull Tests on Deha Anchor Bolts). Institut Für Werkstoffe in Bauwesen, University of Stuttgart." Stuttgart, Germany: Report No. DE003/01-96/32, September (Research carried out on behalf of Deha Ankersystene, GMBH & Co., Gross-Gerau, Germany), 1996.

38. **DeVries, R.A.** "Anchorage of Headed Reinforcement in Concrete." Ph.D. Dissertation, University of Texas at Austin, Austin, Texas, December 1996.

39. **Wright, J. L., and S. L. McCabe.** *The Development Length and Anchorage Behavior of Headed Reinforcing Bars,* Lawrence, Kansas: University of Kansas Center for Research, Report No. 44, September 1997.

40. **Thompson, M.K., A. Ledesma, J. O. Jirsa, and J. E. Breen.** "Lap Splices Anchored by Headed Bars." *ACI Structural Journal*, Vol. 103, No. 2 (2006): 271-279.

41. **Ngo, D., and A. C. Scordelis.** "Finite Element Analysis of Reinforced Concrete Beams." *Journal of American Concrete Institute, Vol.* 64, No. 3 (March 1967): 152–163.

42. **Dinges, D.** *Untersuchung Verschiedener Elementsteifigkeitsmatrizen Auf Ihre Eignung Zur Berechnung von Stahlbetonkonstruktionen: Dritter Zwischenbericht Zum Forschungsvorhaben" Nichtlineare Berechnungen Im Konstruktiven Ingenieurbau*. Darmstadt, Germany: Univ. Kassel, Fachgebiet Massivbau, 1983.

43. **Keuser, M., and G. Mehlhorn.** "Finite Element Models for Bond Problems." *Journal of Structural Engineering, ASCE*, Vol. 113, No. 10 (1988): 2160–2173.

44. **Doerr, K.** "Ein Beitrag Zur Berechnung von Stahlbetonscheiben Unter Besonderer Berucksichtigung Des Verbundverhaltens." Technischeltoch Schale, in Darmstadt, Germany, 1980.

45. **Martin, H.** "Zusammenhang Zwischen Oberflächenbeschaffenheit, Verbund Und Sprengwirkung von Bewehrungsstählen Unter Kurzzeitbelastung." *Deutscher Ausschuss Für Stahlbeton*, No. 228 (1973).

46. **Ingraffea, A. R., W. H. Gerstk, P. Gergely, and V. Saouma, V.** "Fracture Mechanics of Bond in Reinforced Concrete." *Journal of Structural Engineering, ASCE,* Vol. 110, No. 4 (1984): 871–890.

47. **Cox, J. V., and L. R. Herrmann.** "Development of a Plasticity Bond Model for Steel Reinforcement." *Mechanics of Cohesive-Frictional Materials,* Vol. 3, No. 2 (1998).

48. **Hong, S.-G., J. M. Park, T.W. Kim, S.K. Park, and W.J. Ko,** "Bond Stress-Slip Relationship in Reinforced Concrete: New Relationship and Comparative Study." *33rd Conference on Our World in Concrete & Structures,* Singapore, August 25-27, 2008.

49. **Casanova, M.** "Mechanical Properties of High Early Strength Concrete with Polypropylene Fibers for Field-cast Connections of Bridge Precast Elements." Master's Thesis, Idaho State University, Pocatello, ID, 2018.

50. **Idaho Transportation Department.** *Standard Specifications for Highway Construction*. Boise, ID, 2012.

51. **ASTM International**. *Standard Test Method for Relative Density (Specific Gravity) and Absorption of Coarse Aggregate*. West Conshohocken, PA: ASTM C127-15, 2015.

52. **ASTM International**. *Standard Test Method for Relative Density (Specific Gravity) and Absorption of Fine Aggregate*. West Conshohocken, PA: ASTM C128-15, 2015.

53. **ASTM International**. *Standard Test Method for Sieve Analysis of Fine and Coarse Aggregates*. West Conshohocken, PA: ASTM C136-14, 2014.

54. **ASTM International**. *Standard Practice for Making and Curing Concrete Test Specimens in the Laboratory*. West Conshohocken, PA: ASTM C192-16a, 2016.

55. **ASTM International**. *Standard Practice for Capping Cylindrical Concrete Specimens*. West Conshohocken, PA: ASTM C617-15, 2015.

56. **ASTM International**. *Standard Test Method for Compressive Strength of Cylindrical Concrete Specimens*. West Conshohocken, PA: ASTM C39-17b, 2018.

57. **ASTM International**. *Standard Test Method for Static Modulus of Elasticity and Poisson's Ratio of Concrete in Compression*. West Conshohocken, PA: ASTM C469-14, 2014.

58. **American Institute of Steel Construction.** *Manual of Steel Construction*. 15th Ed. Chicago, IL: AISC, 2017.

59. **ANSYS Inc**. "ANSYS User Manual (Version 18)." Cannonsburg, PA: ANSYS Inc., 2016.

60. **Willam, K., and E. Warnke.** "Constitutive Model for the Triaxial Behavior of Concrete." *International Association for Bridge and Structural Engineering Proceedings*, Vol. 19 (1975): 1–30.

61. **Hjelm, H. E.** "Yield Surface for Grey Cast Iron under Biaxial Stress." *Journal of Engineering Materials and Technology,* Vol. 116, No. 2 (April 1994): 148–154.

62. **Kim, J. J., and M. Reda Taha.** "Experimental and Numerical Evaluation of Direct Tension Test for Cylindrical Concrete Specimens." *Advances in Civil Engineering*, 2014.

63. **American Association of State Highway and Transportation Officials.** *AASHTO LRFD Bridge Design Specifications*, Washington, D.C.: American Association of State Highway and Transportation Officials, 2017.